A SEARCH FOR THE HIGGS BOSON IN $H \to WW \to l\nu l\nu$ WITH 8.2 fb^{-1}

BY

BENJAMIN P CARLS

DISSERTATION

Submitted in partial fulfillment of the requirements
for the degree of Doctor of Philosophy in Physics
in the Graduate College of the
University of Illinois at Urbana-Champaign, 2012

Urbana, Illinois

Doctoral Committee:

Assistant Professor Mark Neubauer, Chair
Professor Kevin Pitts, Director of Research
Professor Jon Thaler
Professor Scott Willenbrock

Abstract

This thesis documents a search for Standard Model (SM) Higgs boson to WW production in the final state of two charged leptons (e, μ) and two neutrino final state resulting from in $p\overline{p}$ collisions at $\sqrt{s} = 1.96$ TeV. The data collected by the CDF II detector at the Tevatron collider at Fermilab, corresponds to an integrated luminosity of 8.2 fb^{-1}.

This iteration of the analysis incorporated several improvements to increase Higgs sensitivity. We reevaluated lepton isolation values to recover signal events in which leptons mutually spoil each other's isolation requirements. We additionally incorporated new lepton identification selections, namely likelihood based forward electrons and a better recovery of electrons passing through detector cracks.

The base analysis searches for opposite-sign dilepton events. We employed three separately trained neural networks to distinguish signal from background processes for events with 0, one, or two jets. To further increase sensitivity for 0-jet events, we constructed a likelihood ratio discriminant based on Matrix Element calculations as an additional input to the neural network. For the base opposite-sign analysis, summing over all jet multiplicities, we observed 3513 events in data compared with a background expectation of 3409 ± 233 and a signal expectation of 53.6 ± 9.4 for a mass of 165 GeV/c^2.

To further increase signal acceptance, we incorporated several separate search regions in addition to the base analysis. We include subchannels searching for Higgs production in events with low dilepton invariant mass and in events having final states with either same-sign dileptons or trileptons

With the combination of the separate analyses, we observed a 95% C.L. upper production limit of 0.77 times the SM expectation for a Higgs mass of 165 GeV/c^2 to be compared with the value for the median of the expected limit (0.78). We additionally present results for eighteen Higgs masses ranging from 110 GeV/c^2 to 200 GeV/c^2. We excluded at the 95% C.L., a SM Higgs boson in the mass range between 156 and 175 GeV/c^2.

Acknowledgments

I owe a great deal to my advisor Kevin. He has overseen most of my development as a physicist from when I began as a lowly undergrad at Illinois to where I've ended up now. I owe the appreciation I have for the subtleties of particle physics to him. I'll never forget the nights at the condo discussing how feasible the goals of LHCb were.

I also thank Eric and Sergo, whom I worked on $H \to WW$ with. I loved the opportunity to work on an analysis that was very different from what I had known of physics previously.

There are numerous others in my research group who have helped me. Greg and Ed assisted my navigation of graduate school. Olga provided much camaraderie as we tackled suppressed B_S decays together. Jonathan, who served as our godparent, did a great deal to help us finish the analyses. He also saved me as an ace many times. Heather kept me grounded and provided an enormous amount of support as well as dogs to sit.

There are many others whom I owe a great debt to. I'm quite thankful for my friend Jerry, who introduced me to Vim and always made me strive to be a better programmer. There's Mike, who helped keep me centered and forever scared me away from a normal job. I spent a great deal of time with Allison, Hannah, Kevin, and Scott working field theory problem sets and guessing phone numbers.

I give my father most of the blame for where I am today. From as far back as I remember, he was reading dinosaur books to me, building 6 feet tall models of the Sears tower with my sister and me, and bearing with me when I asked unanswerable questions about the birth of the universe.

My mother and sister Kerry have played a vital role in where I've ended up. My mother introduced the quarks and leptons to me. Kerry provided me with essential support and made staying at Illinois easily the best decision.

This thesis was supported in part by the United States Department of Energy under grant DE-FG02-91ER40677.

Table of Contents

List of Tables

List of Figures

List of Abbreviations

SM	Standard Model.
DY	Drell-Yan.
QED	Quantum Electrodynamics.
QCD	Quantum Chromodynamics.
LEP	Large Electron-Positron Collider.
MI	Main Injector.
COT	Central Outer Tracker.
L00	Layer 00 Silicon Tracker.
SVXII	Silicon Vertex Tracker.
ISL	Intermediate Silicon Layer Tracker.
CEM	Central Electromagnetic Calorimeter.
PEM	Plug Electromagnetic Calorimeter.
CHA	Central Hadronic Calorimeter.
WHA	Wall Hadronic Calorimeter.
PHA	Plug Hadronic Calorimeter.
CES	Central Electromagnetic ShowerMax Chamber.
PES	Plug Electromagnetic ShowerMax Chamber.
CMU	Central Muon Detector.
CMP	Central Muon Upgrade Detector.
CMX	Central Muon Extension Detector.
BMU	Barrel Muon Detector.
CLC	Cerenkov Luminosity Counters.
XFT	eXtremely Fast Tracker.
XTRP	Extrapolation Unit.
SVT	Silicon Vertex Trigger.

JES	Jet Energy Scale.
MC	Monte Carlo Simulation.
NLO	Next-to-Leading Order.
NNLO	Next-to-Next-to-Leading Order.
NNLL	Next-to-Next-to-Leading Log.
ME	Matrix Element.
LR	Likelihood Ratio.
NN	Neural Network.
CL	Confidence Level.

List of Symbols

p_T	Transverse momentum.
η	Pseudorapidity.
ϕ	Detector azimuthal angle.
E_T	Transverse energy.
H_T	The sum of the lepton p_T and event $\not{E}_T$.
$\not{E}_T$	Missing transverse energy.
M_{ll}	Dilepton Mass.
ΔR_{ll}	Spatial separation in η-ϕ space.

Chapter 1

Introduction

The Standard Model of particle physics has proven itself to be a highly successful description of the fundamental particles and their interactions. However, the exact mechanism behind which the fundamental electroweak interaction becomes the electromagnetic and weak interactions remains unknown. One proposal, the Higgs mechanism, introduces a scalar field to break the symmetry between the electromagnetic and weak interactions. The search for the boson associated with the scalar Higgs field remains a primary focus of modern high-energy physics. This thesis details a search for the Higgs boson in decays to two W bosons using the CDF detector at the Tevatron collider.

The thesis gives an introduction to the theory of the Higgs boson in Chapter 2. We describe the process through which the Higgs field breaks the electroweak symmetry and gives masses to the W and Z bosons here. A review of the Higgs search at the Large Electron-Positron Collider follows in Chapter 3 along with an introduction to the search at the Tevatron collider.

A description of the Fermilab accelerator complex and the CDF detector appears in Chapter 4. This covers the components of the CDF detector relevant for the analysis. We describe the process used to identify prospective Higgs decay products in Chapter 5. This includes the identification procedure for electrons and muons. A description of the analysis improvements put into this iteration also appears in Chapter 5. The improvements are crucial for increasing the sensitivity of the analysis beyond what the addition of data alone offers.

The selection criteria we used to identify Higgs events and the data modeling procedure appears in Chapter 6. We describe the limit setting procedure for the primary analysis channels in Chapters 7 and 8.

Finally, the combination of all $H \to WW$ channels from CDF appears in Chapter 9. Additionally, the full Tevatron combination with data from all Higgs channels coming from CDF and D0 also appears. We lastly present a brief discussion of the future prospects for the Higgs boson search.

Chapter 2

The Standard Model and Higgs mechanism

Over the past few decades, the Standard Model (SM) has proven successful in describing the fundamental particles and their interactions. Despite the success of the SM, the framework remains incomplete. The exact mechanism for breaking the symmetry between the electromagnetic and the weak interactions in the SM has thus far eluded detection. One proposal, the Higgs mechanism, is the focus of this thesis. The theory of the SM and the Higgs mechanism will be described in this chapter.

2.1 The Standard Model

The SM is a quantum field theory incorporating three interactions: the strong, the weak, and the electromagnetic. To accomplish this, the SM is based on the gauge symmetry group of $SU(3)_C \times SU(2)_L \times U(1)_Y$ [4]. The gauge group $SU(3)_C$ corresponds to Quantum Chromodynamics or the strong interaction. The gauge group $SU(2)_L \times U(1)_Y$ comprises the electroweak interaction whose symmetry the proposed Higgs field breaks.

The SM contains a range of fundamental particles. The quarks and leptons are the two types of fermions incorporated into the SM. Fermions possess half-integer spin, with the quarks and leptons of the SM having spins of 1/2. The six quarks undergo the electromagnetic, strong, and weak interactions. Of the leptons, three interact weakly and electromagnetically. The other three, the neutrinos, interact weakly. The quarks and leptons are both further divided up into generations. Additionally, each particle possesses an antiparticle partner, an identical particle with the exception of possessing opposite charge. An overview of the quarks appears in Table 2.1. An overview of the leptons appears in Table 2.2.

generation	charge 2/3	charge $-1/3$
1st	up (u) $1.7 - 3.1$ MeV/c^2	down (d) $4.1 - 5.7$ MeV/c^2
2nd	charm (c) 1.29 GeV/c^2	strange (s) 100 MeV/c^2
3rd	top (t) 172.9 GeV/c^2	bottom (b) 4.19 GeV/c^2

Table 2.1: The six quarks in the SM with their masses.

generation	charge -1	charge 0
1st	electron (e) 0.5110 MeV/c^2	electron neutrino (ν_e) $<$ 2 eV/c^2 (CL = 95%)
2nd	muon (μ) 105.7 MeV/c^2	muon neutrino (ν_μ) $<$ 0.19 MeV/c^2 (CL = 90%)
3rd	tau (τ) 1.777 GeV/c^2	tau neutrino (ν_τ) $<$ 18.2 MeV/c^2 (CL = 90%)

Table 2.2: The six leptons in the SM with their masses. Note, the neutrino masses listed are expectation values based on taking the square roots of $m^2_{\nu_l} = \sum_i |\mathrm{U}_{li}|^2 m^2_{\nu_i}$ for a neutrino of flavor l. Here, m_{ν_i} are the three neutrino mass eigenstates and U_{li} are the elements of the neutrino mixing matrix relating the mass eigenstates to the flavor eigenstates. Limits on the sum of the neutrino masses based on comological measurements are considerably stricter, being as low as $m_{tot} < 0.44$ eV/c^2 (CL = 95%).

2.1.1 The electroweak interaction

As mentioned above, the electroweak interaction lives in the symmetry group $SU(2)_L \times U(1)_Y$, having gauge bosons W^i_μ (for $i = 1, 2, 3$) for $SU(2)_L$ and B_μ for $U(1)_Y$ [4]. We specify the fermions as weak isospin doublets which are left-handed and singlets which are right-handed. The left-handed weak isospin doublets, which transform under $SU(2)_L$, take the form

$$\begin{pmatrix} \nu_e \\ e \end{pmatrix}_L, \begin{pmatrix} \nu_\mu \\ \mu \end{pmatrix}_L, \begin{pmatrix} \nu_\tau \\ \tau \end{pmatrix}_L$$

and

$$\begin{pmatrix} u \\ d' \end{pmatrix}_L, \begin{pmatrix} c \\ s' \end{pmatrix}_L, \begin{pmatrix} t \\ b' \end{pmatrix}_L.$$

Here, the primes correspond to mass eigenstates of the weak interaction. These are relatable to the aforementioned flavor eigenstates (u, s, and b) via the transformation $d' = \sum_j V_{ij} d_j$, where V_{ij} represents elements of the Cabibbo-Kobayashi-Maskawa (CKM) matrix. The CKM matrix relates the weak quark eigenstates to the flavor eigenstates. The right-handed $SU(2)_L$ singlets take the form of e_R, ν_{eR}, u_R, etc.

The symmetry group $SU(2)_L$ has three generators following from the Pauli matrices as $T^i = \sigma^i/2$ [5] and obey the commutation relation of

$$[T^i, T^j] = i\epsilon_{ijk} T^k.$$

We can relate the particle's charge Q to its weak isospin (T^3) and weak hypercharge Y using the relation of

$$Q = T^3 + \frac{Y}{2}.$$

The weak hypercharge Y operates as the generator for $U(1)_Y$ [6]. The first generation fermions with their quantum numbers appear in Table 2.3.

lepton	T	T^3	Q	Y
ν_e	1/2	1/2	0	−1
e_L^-	1/2	−1/2	−1	−1
e_R^-	0	0	−1	−2

quark	T	T^3	Q	Y
u_L	1/2	1/2	2/3	1/3
d_L	1/2	−1/2	−1/3	1/3
u_R	0	0	2/3	4/3
d_R	0	0	−1/3	−2/3

Table 2.3: The six quarks in the SM with their masses.

With the aforementioned gauge bosons of $W^i_{\mu\nu}$ (for $i = 1, 2, 3$) and $B_{\mu\nu}$, the electroweak Lagrangian's kinetic energy terms for the fields are given by

$$\mathcal{L}_{gauge} = -\frac{1}{4}W^i_{\mu\nu}W^{\mu\nu i} - \frac{1}{4}B_{\mu\nu}B^{\mu\nu}$$

for

$$W^i_{\mu\nu} = \partial_\nu W^i_\mu - \partial_\mu W^i_\nu + g\epsilon_{jkl}W^j_\mu W^l_\nu,$$

$$B_{\mu\nu} = \partial_\nu B_\mu - \partial_\mu B_\nu,$$

and g being a coupling constant [6]. The interaction of the field with generic fermionic fields is given by

$$\begin{aligned}\mathcal{L}_{fermions} = \quad & \bar{\psi}_R i\gamma^\mu(\partial_\mu + i\tfrac{g'}{2}YB_\mu)\psi_R \\ & +\bar{\psi}_L i\gamma^\mu(\partial_\mu + i\tfrac{g'}{2}YB_\mu + i\tfrac{g}{2}\vec{T}\cdot\vec{W}_\mu)\psi_L,\end{aligned}$$

where g' is an additional coupling constant, ψ_R is a right handed fermionic field, and ψ_L is a left handed fermionic field [4]. The two Langrangians form the basic electroweak interaction of

$$\mathcal{L}_{ewk} = \mathcal{L}_{gauge} + \mathcal{L}_{fermions}.$$

2.2 Electroweak symmetry breaking

In the electroweak Lagrangian above, the boson fields are all massless and the symmetry of $SU(2)_L \times U(1)_Y$ is still intact. The physical bosons seen today are given by mixtures of the massless gauge fields of $W^i_{\mu\nu}$ and

$B_{\mu\nu}$ [4]. The physical $W^{\pm}$ fields are given by

$$W_{\mu}^{\pm} = \sqrt{\frac{1}{2}}(W_{\mu}^{1} \mp iW_{\mu}^{2})$$

and the physical Z and photon fields are given by

$$Z_{\mu} = W_{\mu}^{3}\cos\theta_{W} - B_{\mu}\sin\theta_{W}$$

and

$$A_{\mu} = B_{\mu}\cos\theta_{W} + W_{\mu}^{3}\sin\theta_{W}$$

respectively. Here, θ_W is the Weinberg angle which can be related to the coupling constants g and g' by

$$g\sin\theta_{W} = g'\cos\theta_{W} = e$$

where e is the electric charge.

To break the electroweak symmetry of $SU(2)_L \times U(1)_Y$ and produce the observed physical bosons described above, we introduce a complex doublet of scalar fields

$$\phi = \begin{pmatrix} \phi^{\dagger} \\ \phi^{0} \end{pmatrix},$$

which possesses a weak hypercharge of $Y = +1$ [4]. We introduce this field into the electroweak Lagrangian with

$$\mathcal{L}_{scalar} = (\mathcal{D}^{\mu}\phi)^{\dagger}(\mathcal{D}_{\mu}\phi) - V(\phi^{\dagger}\phi),$$

where the covariant derivative $\mathcal{D}^{\mu}$ is

$$\mathcal{D}^{\mu} = \partial^{\mu} + i\frac{g'}{2}YB^{\mu} + i\frac{g}{2}\vec{T}\cdot\vec{W}^{\mu},$$

and the potential $V(\phi^{\dagger}\phi)$ is

$$V(\phi^{\dagger}\phi) = \mu^{2}(\phi^{\dagger}\phi) + |\lambda|(\phi^{\dagger}\phi)^{2}.$$

The quantities μ and λ are both constants. If we proceed to minimize the action of the Lagrangian, we

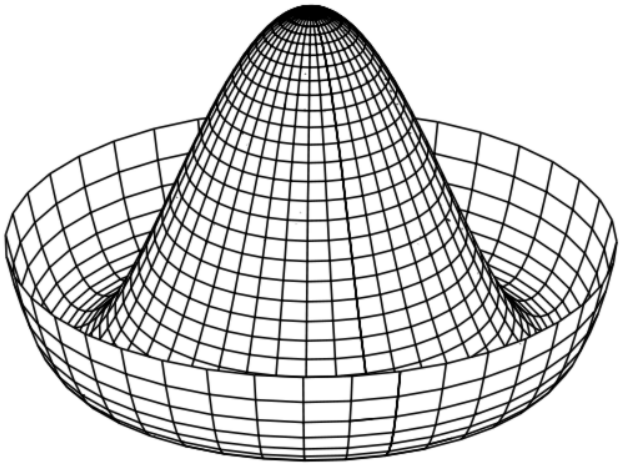

Figure 2.1: The shape of the scalar field's potential.

arrive with a vacuum expectation value for the scalar field of

$$\langle\phi\rangle_0 = \sqrt{\frac{1}{2}}\begin{pmatrix} 0 \\ v \end{pmatrix},$$

where $v = \sqrt{-\mu^2/|\lambda|}$.

The scalar field's potential is shown in Figure 2.1.

We can examine small oscillations, $\xi^i(x)$ (for $i = 1, 2, 3$) and $\eta(x)$ off of the vacuum expectation value of $\langle\phi\rangle_0$ with

$$\phi = \exp\left(\frac{i\xi^i(x)T^i}{2v}\right)\begin{pmatrix} 0 \\ \frac{v+\eta(x)}{\sqrt{2}} \end{pmatrix}.$$

Employing a gauge transformation in $SU(2)_L$ eliminates the exponential function containing $\xi^i(x)$, giving

$$\phi = \begin{pmatrix} 0 \\ \frac{v+\eta(x)}{\sqrt{2}} \end{pmatrix}.$$

Using this in the electroweak Lagrangian provides mass terms for the $W^{\pm}$ and Z bosons, $M_W = \frac{1}{2}vg$ and $M_Z = \frac{1}{2}v\sqrt{g^2 + g'^2}$ respectively, while the photon field remains massless [4]. Also important is that the Higgs field $\eta(x)$ receives a mass term of $M_H = 2v^2\lambda = -2\mu^2$ for $\mu^2 < 0$.

2.3 Indirect constraints on the Higgs boson mass

The Higgs mechanism leaves the Higgs mass behind as a free parameter which cannot be directly determined without experimental measurement. It is possible however through SM consistency checks to determine constraints on the Higgs mass.

In the instance of gauge boson scattering (e.g. $WW \rightarrow WW$), through partial-wave analysis, it can be shown that the scattering amplitudes are proportional to $G_F M_H^2$, for the Fermi coupling constant G_F [4]. If we enforce unitarity for the largest eigenvalue from the partial-wave analysis, $|a_0| \leq 1$, this results in a requirement on the Higgs mass of

$$M_H \leq \left(\frac{8\pi\sqrt{2}}{3G_F} \right)^{1/2} = 1 \text{ TeV/c}^2$$

to prevent a quadratic divergence of the scattering amplitude. This provides us with a reasonably solid upper limit on the mass of a potential Higgs boson.

Additionally, a confidence interval can be determined based on precision electroweak measurements. In the SM, the mass of the W boson receives corrections dependent on the masses of the top quark and the Higgs boson. This dependence happens to be quadratic for the top quark mass and logarithmic for the Higgs boson mass. Combining measurements of the W and top quark masses with other electroweak measurements gives values the Higgs mass is likely to have.

The result of such a fit appears in Figure 2.2 and shows the dependence of the Higgs boson mass in relation to current measurements of the W and top quark masses. The limit on the Higgs mass produced by the fit was $M_H < 161$ GeV/c^2 at the 95 % C.L. [1] The central value produced by the fit was $M_H = 92^{+34}_{-26}$ GeV/c^2.

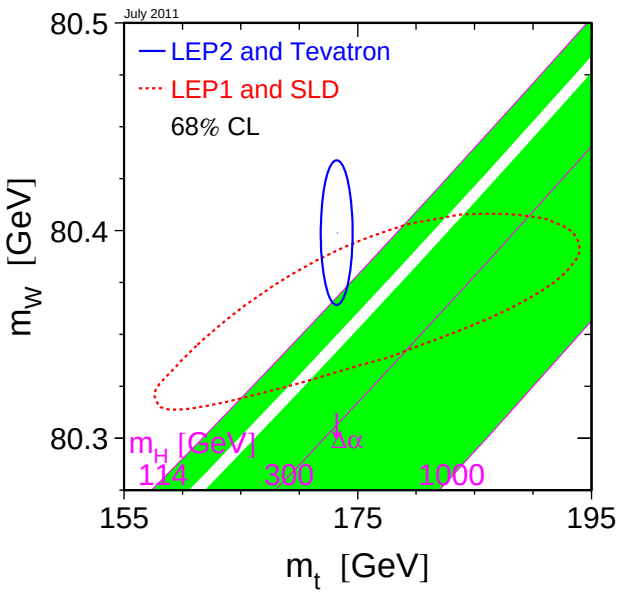

Figure 2.2: The result of the electroweak fit for the Higgs mass as a function of the W boson and top quark masses [1]. Values for the Higgs list appear on the bottom axis in purple. The relation of the Higgs mass to the W boson and top quark masses follow the purple lines. The 68% CL region of the fit based on direct measurements from LEP-II and the Tevatron appear as the solid blue contour. The 68% CL region of the fit based on indirect measurements from LEP-I and SLD appear as the dotted red contour. The green regions are Higgs mass regions not yet excluded by experiment. The 1000 GeV/c^2 cut off is applied based on theoretical arguments from gauge boson scattering.

Chapter 3

Searches for the Higgs boson

The goal of observing or excluding a Higgs boson is a strong focus of modern high-energy physics. An overview of Higgs production, decays, and previous searches follows.

3.1 Searching for the Higgs at LEP

Most recently, the Higgs search in the low mass region has been dominated by the Large Electron-Positron Collider (LEP), which collided beams of positrons with beams of electrons. The LEP collider featured four experiments: ALEPH, DELPHI, L3, and OPAL. They collected 2461 pb^{-1} of total data at center of mass energies ranging from 189 and 209 GeV/c^2 [2].

3.1.1 Higgs production at LEP

The primary production mechanism of interest at LEP was associated production. In associated production, a Z boson created from $e^+e^- \rightarrow Z$, radiates a Higgs boson [2]. An additional production mechanism at LEP was through vector boson fusion, in which either two W bosons or two Z bosons, radiated from an electron-positron pair, fuse to produce a Higgs boson. The Feynman diagrams for these mechanisms appear in Figure 3.1.

3.1.2 Higgs decays at LEP

In the mass ranges the LEP experiments were sensitive to, the Higgs predominantly decays to $b\bar{b}$ with decays to $\tau^+\tau^-$, WW^*, gg, and $c\bar{c}$ also contributing. A plot of the Higgs decay branching fractions appears in Figure 3.2. For associated production, the decays of the Z boson also contribute to the event topology with decays of $Z \rightarrow q\bar{q}$, $Z \rightarrow \nu\bar{\nu}$, and $Z \rightarrow l^+l^-$. The final states the LEP experiments looked for were the four jet final state ($H \rightarrow b\bar{b}$ and $Z \rightarrow q\bar{q}$); missing energy final state ($H \rightarrow b\bar{b}$ and $Z \rightarrow \nu\bar{\nu}$); electron or muon final state ($H \rightarrow b\bar{b}$ and $Z \rightarrow l^+l^-$); and the tau final state consisting of ($H \rightarrow b\bar{b}$ and $Z \rightarrow \tau^+\tau^-$) and ($H \rightarrow \tau^+\tau^-$ and $Z \rightarrow q\bar{q}$) [2]. The predominant backgrounds in these analyses were diphoton processes,

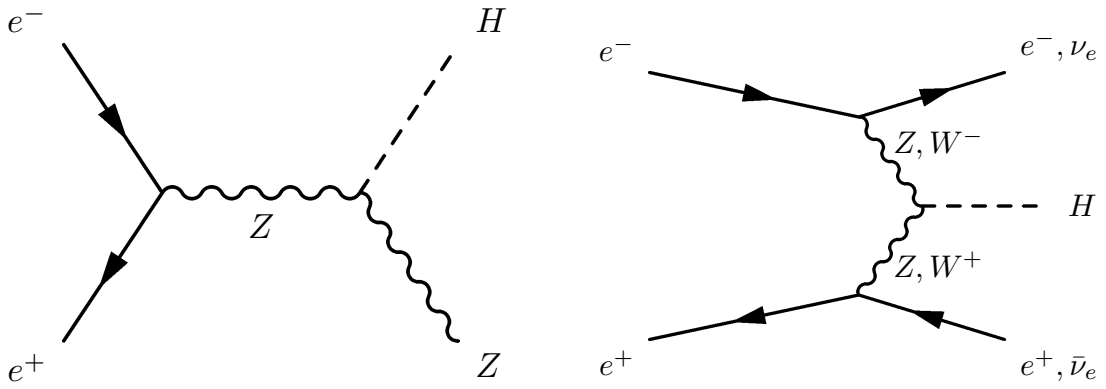

Figure 3.1: Two Higgs production mechanisms expected at LEP, associated production (left) and vector boson fusion (right).

$e^+e^- \to Z\gamma$, $q\bar{q}$, and WW/ZZ production.

The LEP experiments did not see any strong evidence for a Higgs boson. They therefore proceeded to set limits on possible Higgs boson masses. The LEP experiments ruled out Higgs masses below 114.4 GeV/c^2 [2] at the 95% confidence level. The confidence level limits as a function of Higgs masses appears in Figure 3.3.

3.2 Searching for the Higgs at the Tevatron

Over the past few years of the Tevatron's second running, CDF and D0 have become sensitive to the Higgs boson. An introduction to Higgs searches follows with descriptions of production and decay mechanisms at the Tevatron.

3.2.1 Higgs production at the Tevatron

There are three primary modes of Higgs production at the Tevatron: gluon fusion, associated production, and vector boson fusion. Gluon fusion production is the dominate mode, with a cross-section just below 1 pb^{-1} [3]. Gluon fusion Higgs production proceeds via the fusion of two gluons into a quark loop which produces a Higgs boson. The Feynman diagram appears in Figure 3.4.

After gluon fusion, the two other production mechanisms relevant for this analysis are associated production and vector boson fusion. They are quite similar to the production mechanisms at LEP previously discussed. Feynman diagrams depicting both mechanisms appear in Figure 3.5. Associated production and Vector boson fusion both have cross-sections roughly a factor of 10 smaller than gluon fusion.

A plot of the cross-sections for gluon fusion, associated, vector boson fusion, and other productions mechanisms at the Tevatron as a function of Higgs mass appears in Figure 3.6.

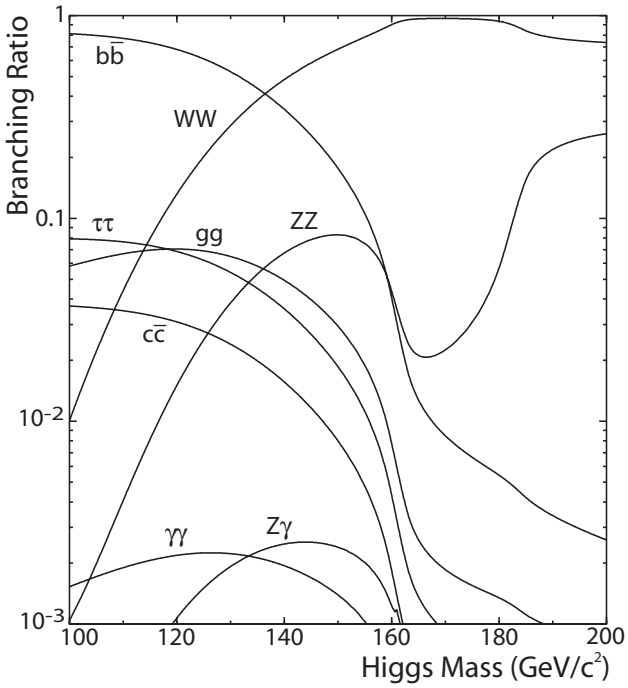

Figure 3.2: The expected branching ratios for Higgs decays for masses between 100 and 200 GeV/c^2.

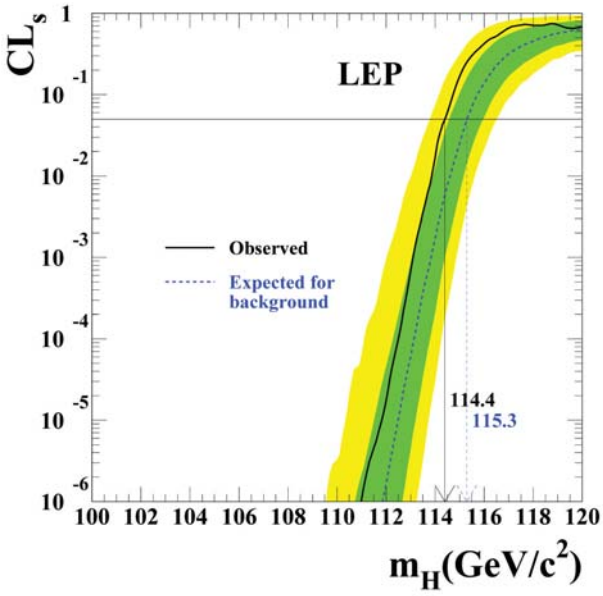

Figure 3.3: The limit on SM Higgs production from the four LEP experiments [2]. Here CL_s is the confidence level indicated by the data that the expected Higgs production cross-section is above the SM expectation. The 5% level is indicated by a black line. The expected limit, generated by pseudoexperiments, appears as a dotted blue line. Bands indicating 1σ and 2σ deviations in the expected limit appear and green and yellow bands respectively. The observed limit appears as the solid black line.

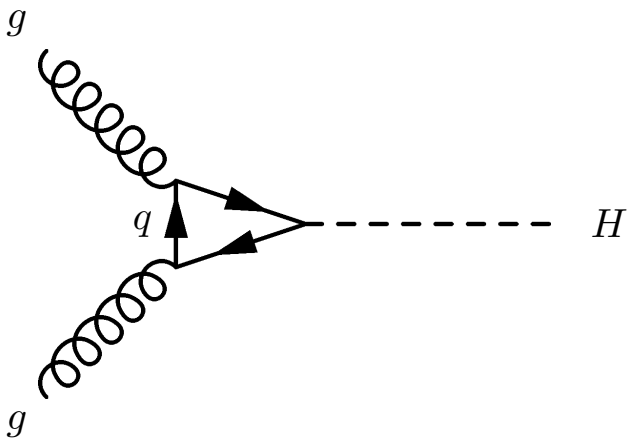

Figure 3.4: The gluon fusion Higgs production mechanism at the Tevatron. The quark loop is predominately top.

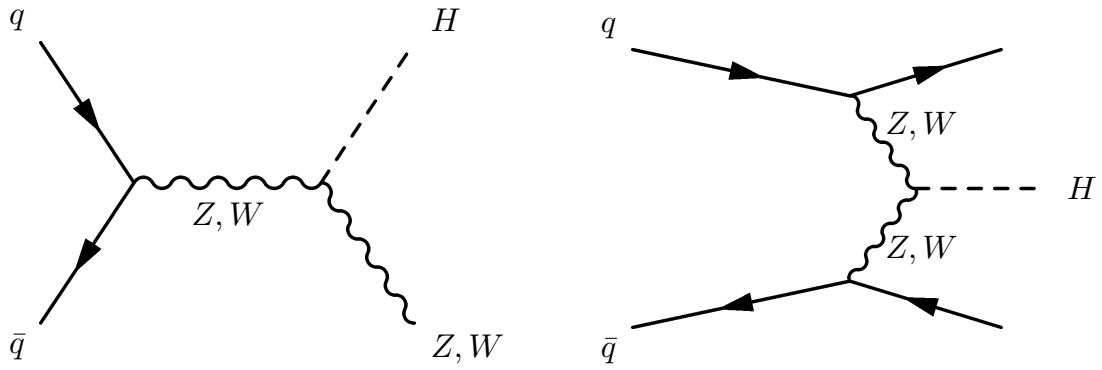

Figure 3.5: Two Higgs production mechanisms expected at the Tevatron, associated production (left) and vector boson fusion (right).

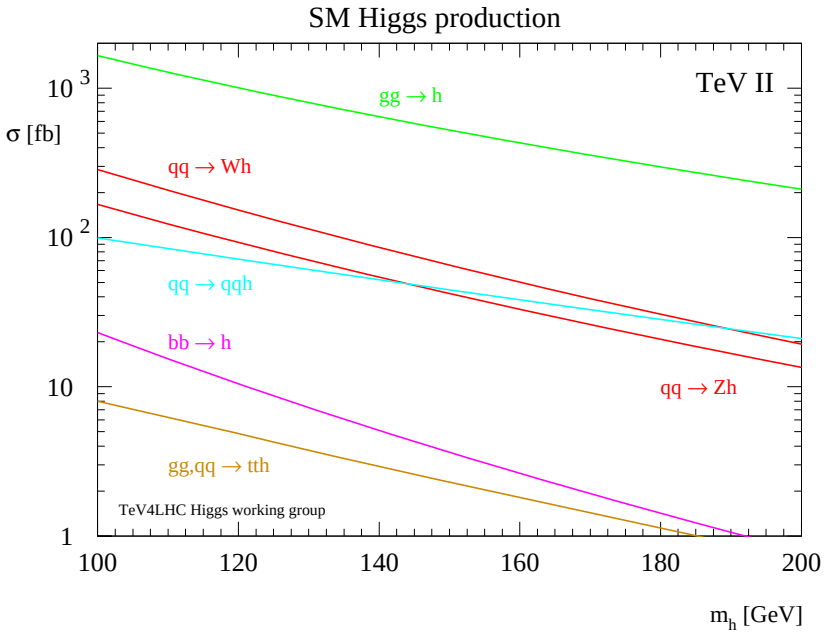

Figure 3.6: The cross-section for gluon fusion ($gg \rightarrow h$), associated production ($qq \rightarrow Wh$ and $qq \rightarrow Zh$), and vector boson fusion ($qq \rightarrow qqh$) at the Tevatron as a function of Higgs mass [3]. Two other production mechanisms at the Tevatron are also shown, $bb \rightarrow h$ and $gg, qq \rightarrow tth$.

3.2.2 Low-mass Higgs search at the Tevatron

The preferred Higgs decay below ≈ 135 GeV/c^2 is $H \rightarrow b\bar{b}$ as shown in Figure 3.2. The $b\bar{b}$ final state is not distinct enough to distinguish from the prominent QCD backgrounds that emerge. For example, the $p\bar{p} \rightarrow b\bar{b}$ production cross-section, on the order of 1 μb, is a million times larger than the $gg \rightarrow H$ cross-section of approximately 1 pb. As a consequence, we cannot use the dominate $gg \rightarrow H$ production mechanism since it leaves no handles to distinguish $H \rightarrow b\bar{b}$ from QCD backgrounds. In the case of associated production, the additional W or Z in the event provide excellent handles to differentiate signal from background.

3.2.3 High mass Higgs search at the Tevatron

For the Tevatron, the high mass search considers primarily the Higgs mass region of 135 GeV/c^2 to 200 GeV/c^2, where the Higgs boson decays predominantly to pairs of W bosons. As opposed to the $b\bar{b}$ final state, the decays of the W bosons provide better handles to differentiate Higgs events from background.

The branching fraction of hadronic W decays is $\approx 68\%$ [5]. There are three leptonic decay modes, $W \rightarrow l\nu$ (for $l = e, \mu, \tau$), having a branching fraction of $\approx 10.8\%$ for each.

For a Higgs analysis, the final states of both W bosons decaying is not a distinctive enough of a final state to distinguish from background. In this analysis, we look for both W bosons to decay leptonically,

giving us the final state of $l\nu l\nu$.

Out of the leptonic decays, we look only for the electron and muon final states since the CDF detector is fairly adept at identification of these particles. We therefore restrict ourselves to 4.7% of all the final states of $H \rightarrow WW$.

3.2.4 Increased Higgs sensitivity through analysis improvements

Though the Higgs analyses at CDF increase sensitivity through luminosity additions, a significant amount of sensitivity increases result from improving the analyses. Figure 3.7 shows the expected sensitivity for a given iteration of the analysis as a function of luminosity. The plot shows the first iteration of the analysis done in Summer 2004 for comparison to the result this thesis documents. If the Summer 2004 version of the analysis had been used with the data available for Summer 2011, CDF would still be unable to exclude a Higgs boson at a mass of 160 GeV/c^2. The improvements over the Summer 2010 CDF $H \rightarrow WW$ analysis we put in to reach the sensitivity seen in Figure 3.7 will be a strong focus of this thesis.

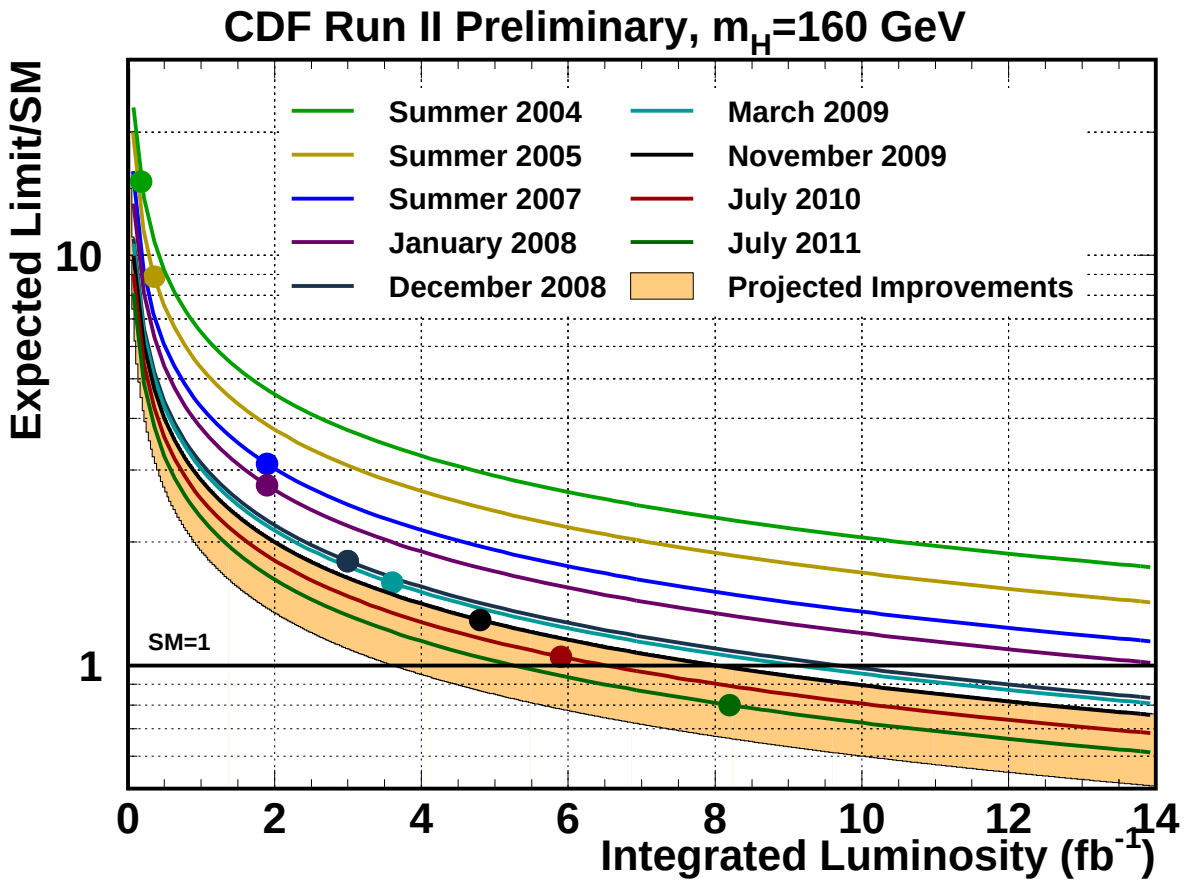

Figure 3.7: The expected sensitivity to the Higgs boson as a function of luminosity for a Higgs mass of 160 GeV/c^2. We plot several curves for different iteration of the analysis. Improving the CDF Higgs analyses significantly increases sensitivity.

Chapter 4

Tevatron collider and CDF detector

The Fermilab accelerator complex housed the worlds most powerful collider, the Tevatron, until the advent of the Large Hadron Collider in 2008. The Tevatron supplied beams of protons and antiprotons to two collider experiments, CDF and D0, from 2001 to 2011, the years of the Tevatron's Run II.

4.1 The Fermilab accelerator chain and the Tevatron collider

The Tevatron collides protons and antiprotons at a center of mass energy of $\sqrt{s} = 1.96$ GeV. The Tevatron collider itself is only one part of the long chain of accelerators that bring protons and antiprotons to collisions. The wide range of accelerators consists of two Cockcroft-Walton accelerators, a linear accelerator, and several synchrotrons.

4.1.1 Cockcroft-Walton, Linac, and Booster

The accelerator chain begins with the aforementioned Cockcroft-Walton accelerators which produce atoms of H^- at energies up to 750 KeV [7]. The H^{-1} atoms are then fed through a transfer line and into a linear accelerator (Linac) that brings them up to 400 MeV. The Linac operates in a series of pulses at 15 Hz.

Once the H^- atoms have reached 400 MeV, we strip two electrons off of the atoms leaving behind protons [7]. The protons then enter a synchrotron called the Booster which accelerates the protons to 8 GeV. The Booster consists of 19 radio frequency cavities to produce a ring with a radius of 75 meters. The combined accelerator chain consisting of the Linac and Booster, produces the 8 GeV protons in bunches of roughly 1×10^{11} particles.

4.1.2 Main Injector

The Main Injector (MI) is the next level of acceleration after the Linac and Booster. The MI is a synchrotron constructed as an upgrade of the accelerator complex for Run II of the Tevatron. The MI takes the 8 GeV protons from the booster and accelerates them to either 120 GeV or 150 GeV depending on the destination [7].

We fed the 120 GeV protons into the portion of the complex responsible for antiproton production. We used the 150 GeV acceleration mode to feed protons and antiprotons into the Tevatron, which accepted particles with an energy of 150 GeV. The MI carried through an acceleration cycle every 2.2 seconds while the Tevaton operated. The particle bunches each consisted of roughly 10^{11} protons.

4.1.3 Antiproton source

To produce antiprotons, we carried the 120 GeV protons from the MI to the antiproton source where we collided them with a nickel alloy target [7]. The secondary interactions then produced antiprotons with energies around 8 GeV. We collected the 8 GeV antiprotons using magnets to select particles based on momentum and charge.

Once produced, we fed the antiprotons into a synchrotron called the Debuncher. The Debuncher captured the antiprotons and performed stochastic cooling [7] to decrease their high momentum spread. Stochastic cooling made the bunches more manageable by correcting the highly varied antiproton orbits in the Debuncher. To accomplish this, we measured a signal for the antiproton bunch on one side of the ring, amplified it, and applied it to the same bunch on the other side of the ring. The stochastic cooling apparatus applied corrections in the transverse plane to decrease oscillations in the horizontal and vertical directions, and also to the momenta of antiprotons.

Once cooled, we fed the antiprotons into another synchrotron housed in the same tunnel as the Debuncher called the Accumulator. The Accumulator acted as temporary storage for the 8 GeV antiprotons until they were ready to be transfered to another ring, the Recycler, for longer term storage.

4.1.4 Recycler

The Recycler is another synchrotron housed in the same tunnel as the MI. The Recycler stored antiprotons, taken from the Accumulator, until a new collider store was ready to begin. The Recycler is composed of permanent magnets with the intention of storing antiprotons in the event of power loss. The Recycler is equipped with both stochastic and electron cooling. Electron cooling overlays a beam of electrons with the antiprotons to transfer momentum to the electrons from antiprotons not in ideal orbits.

4.1.5 Tevatron

The Tevatron, with a 4 mile circumference, was the largest accelerator at the Fermilab complex [7]. The Tevatron accelerated protons and antiprotons out of the MI from 150 GeV to 980 GeV. Fermilab designed

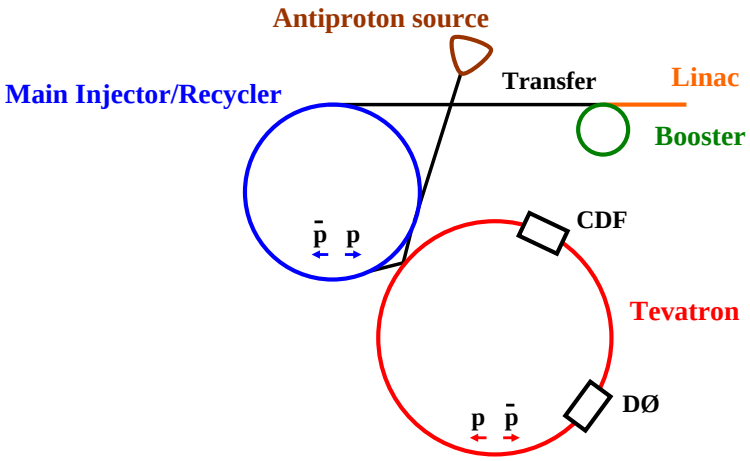

Figure 4.1: A diagram of the Fermilab accelerator complex.

the Tevatron to store protons and antiprotons for several hours while the two collider experiments, CDF and D0, collected data.

The Tevatron made use of niobium/titanium alloy superconducting magnets which required an operating temperature of around 4 K [7]. To achieve this, we made use of an extensive cryogenic infrastructure to supply liquid helium to the magnets. We used superconducting magnets since they allow high magnetic fields to be produced through high currents running through relatively thin wires.

A diagram of the Fermilab accelerator complex appears in Figure 4.1.

When the Tevatron ran in collider mode for Run II, it collided 36 bunches of protons with 36 bunches of antiprotons with a bunch crossing rate of 396 ns. We further divided the groups of 36 bunches into groups of 12. Between each group of 12, we left an open space in the accelerator called an abort gap. The abort gaps provided time to activate the Tevatron's abort system to dump the beam if it became necessary.

The instantaneous luminosity in the Tevatron is given by:

$$L = \frac{fBN_pN_{\bar{p}}}{2\pi(\sigma_p^2 + \sigma_{\bar{p}}^2)} \tag{4.1}$$

where B is the number of bunches in each beam, N_p ($N_{\bar{p}}$) is the number of protons (antiprotons) in each bunch, σ_p ($\sigma_{\bar{p}}$) is the proton (antiproton) rms beam size at the interaction point, and f is the frequency of revolution [8]. The data we used in this analysis came from instantaneous luminosities ranging from 0.1×10^{32} cm^{-2}s^{-1} to 4×10^{32} cm^{-2}s^{-1}.

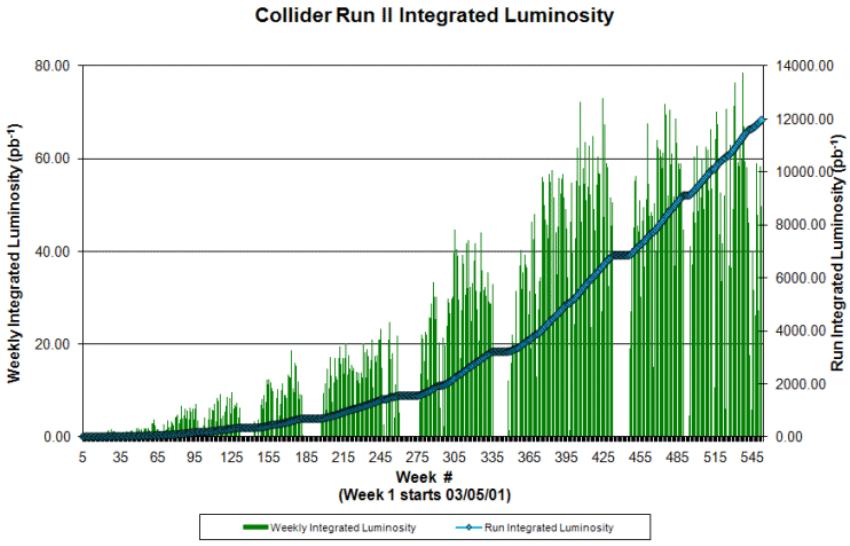

Figure 4.2: The integrated luminosity delivered to CDF and D0.

The delivered integrated luminosity appears in Figure 4.2. The initial instantaneous luminosities appear in Figure 4.3.

4.2 CDF II detector

The multipurpose CDF detector proved itself useful for a variety of analyses. This analysis made extensive use of the calorimetry, tracking, and muon systems of the detector. We document the utilized subdetectors in this section. A diagram of the detector appears in Figure 4.4.

4.2.1 Coordinate system

In the description of the detector geometry, we make extensive use of the azimuthal angle ϕ and polar angle θ. We define the polar angle θ with respect to the proton beam axis which moves in the positive z-direction. We also define an additional quantity called the pseudorapidity

$$\eta = -\ln(\tan\frac{\theta}{2}). \tag{4.2}$$

We define a variant on the pseudorapidity in relation to the detector's center as η_{det}.

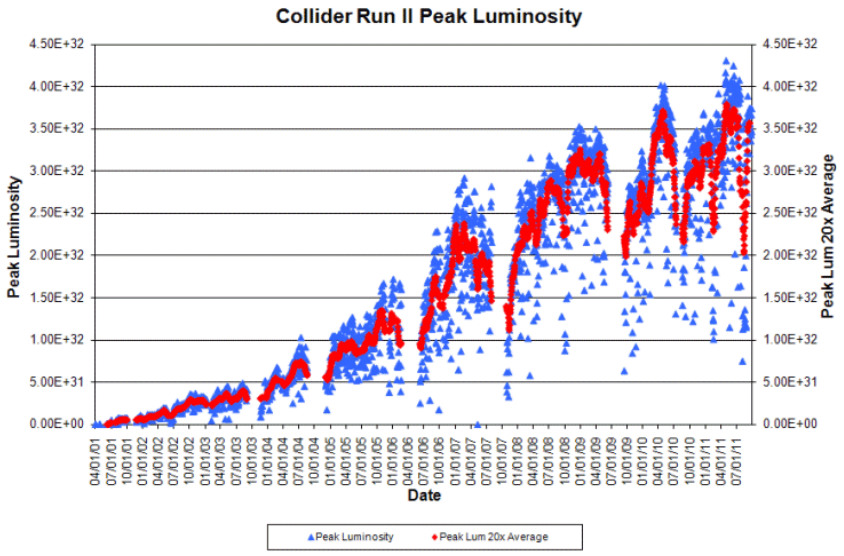

Figure 4.3: The initial instantaneous luminosity delivered by the Tevatron.

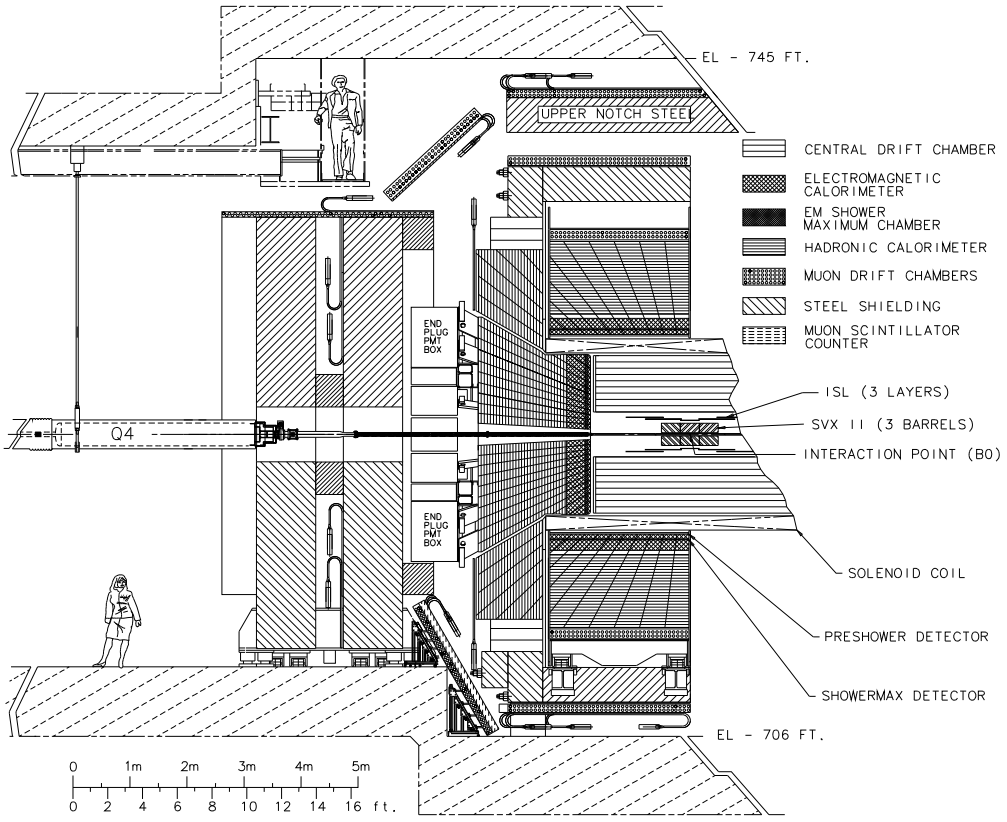

Figure 4.4: A cutaway of the CDF detector.

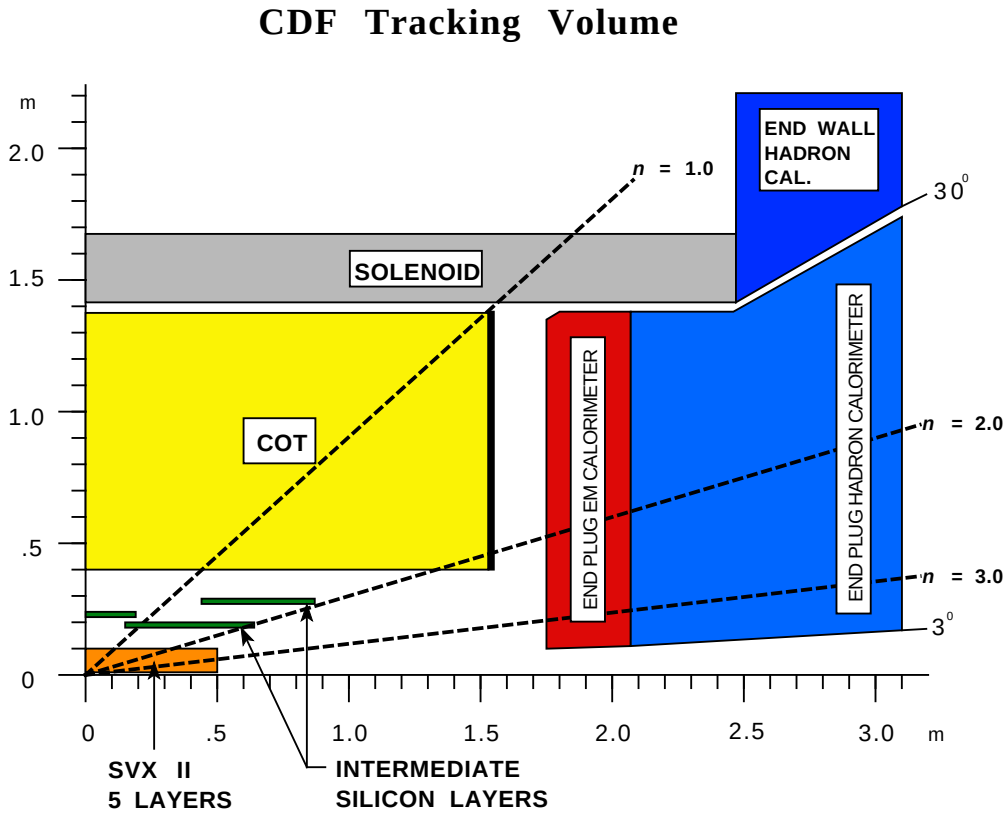

Figure 4.5: The tracking volume of the CDF detector.

4.2.2 Tracking

For tracking we made use of a drift chamber, the Central Outer Tracker (COT), and several silicon detectors. The detector immersed all the tracking sub-detectors in a 1.4 T magnetic provided by a superconducting solenoid. The magnetic field ran parallel to the beam axis. A schematic of the CDF tracking volume appears in Figure 4.5.

Central Outer Tracker

The COT was an open cell drift chamber and contained argon-ethane gas within its volume [9]. It covered the polar range of $|\eta| \leq 1.0$ and the radii of 44 to 132 cm. We divided the COT into eight superlayers, each consisting of multiple cells. The cells each have 12 layers of sense wires. The COT alternated the superlayers between being axial (parallel to the beam axis) and stereo (being off parallel to the beam axis by 2.0°). A schematic of a portion of the COT appears in Figure 4.6.

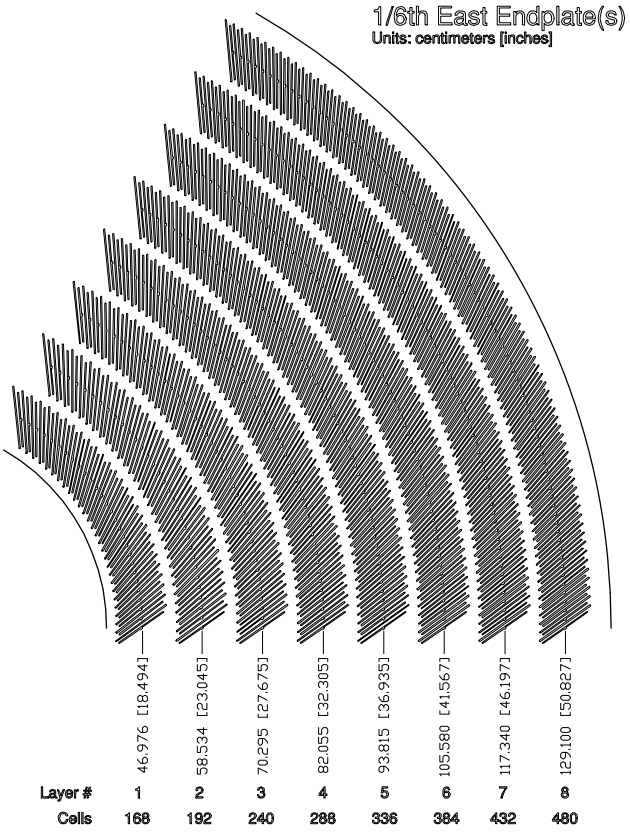

Figure 4.6: A section of the COT end plate.

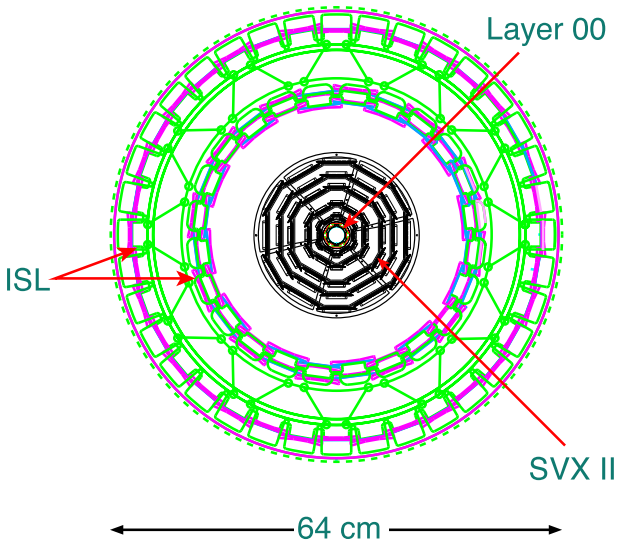

Figure 4.7: The silicon sub-detectors of the CDF detector.

Layer 00

The inner most sub-detector is a single sided silicon detector called Layer 00 (L00) [10]. This detector is mounted directly on the beam pipe, located 1.6 cm off the beam axis. It provided coverage of $|\eta| \leq 4.0$.

Silicon Vertex Tracker II

Outside of L00, sat the Silicon Vertex Tracker II (SVXII), a silicon microstrip detector [10]. The SVXII comes in five double sided layers, extending from radii of 2.1 to 17.3 cm. All layers have the inner strips aligned axially. Layers 1, 2, and 3 have the outer strips rotated by 90° to provide stereo information. Layers 4 and 5 have the outer strips rotated by 1.2° for additional stereo information.

Intermediate Silicon Layers

Outside of the SVXII sat the Intermediate Silicon Layers (ISL) [10]. The ISL was a collection of three layers of double sided microstrips, each having an axial side and a stereo side (strips rotated by 1.2°). One layer covered the central region of $|\eta| \leq 1.0$ and sat at a radius of 22 cm from the beam axis. The two other layers covered the forward regions of $1.0 \leq |\eta| \leq 2.0$ and sat at radii of 20 and 28 cm.

An end view schematic of the silicon detectors appears in Figure 4.7.

4.2.3 Calorimetry

The calorimeters sat outside of the tracking volume and held responsibility for measuring the energies and directions of both neutral and charged particles.

The CDF detector made use of two types of calorimeters, an inner electromagnetic calorimeter and an outer hadronic calorimeter [11]. The electromagnetic calorimeters registered particles which interact electromagnetically, primarily electrons and photons. The hadronic calorimeters registered particles which interact strongly such as mesons and baryons.

The electromagnetic calorimeter consisted of alternating layers of lead and scintillator while the hadronic calorimeter used alternating layers of iron and scintillator. When particles interacted with the lead or iron layers, they created showers of charged particles. When the charged particles pass through the scintillator layers, the scintillators fluoresce. The detect the generated light, we passed it through a wavelength shifter and further onward to a photomultiplier tube via wave guides.

The CDF detector divided the calorimeter in five components: the Central Electromagnetic (CEM), the Central Hadronic (CHA), the Wall Hadronic (WHA), the Plug Electromagnetic (PEM), and the Plug Hadronic (PHA) [11]. A description of these components follows.

Central calorimeter

The CDF detector divided the CEM into towers, each with coverage of 15° in ϕ and 0.11 in η [11]. As a whole, the CEM covers the range of $|\eta| \leq 1.1$. A schematic of a portion of the CEM appears in Figure 4.8. Outside of the CEM, the CHA covered the range of $|\eta| \leq 0.9$. To augment the coverage of the CHA, the WHA covered the range of $0.8 \leq |\eta| \leq 1.2$. The towers of the CHA and WHA match the 15° in ϕ and 1.1 in η coverage of the CEM.

The CEM had two additional detectors embedded in it, the Central Electromagnetic ShowerMax chamber (CES) and the Central Pre-radiate (CPR) chamber [11]. The CES was a strip and wire chamber placed six radiation lengths into the CEM where the electromagnetic shower from particles is expected to be the widest. The CES provided additional capabilities for particle identification and linking to particle tracks. A CES module appears in Figure 4.9.

The CPR was a collection of wire chambers lying on the inner surface of the CEM [11]. The CPR provided early measurements of showers and useful discrimination of electrons from pions. The CPR also proved useful for photon identification.

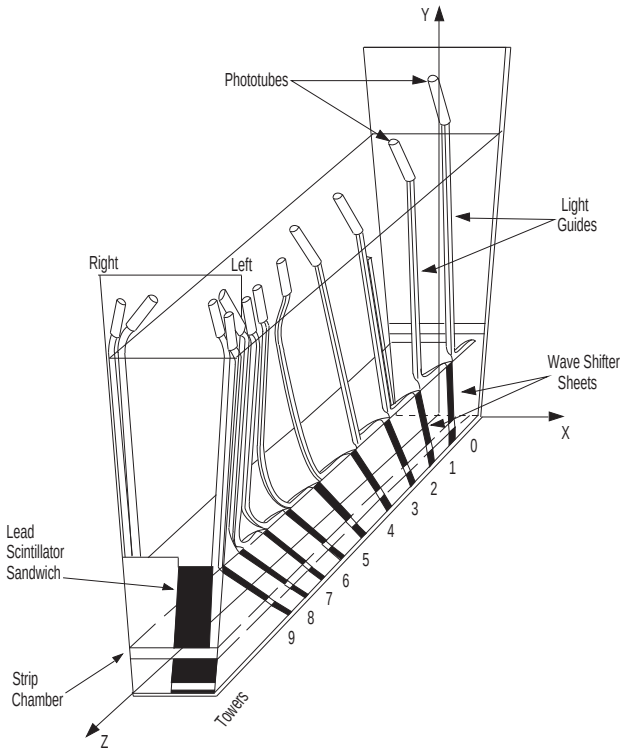

Figure 4.8: A portion of the CEM.

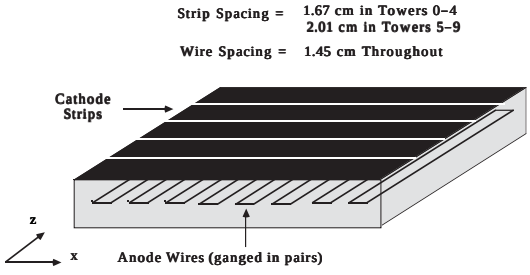

Figure 4.9: A portion of the CES wire and strip chamber.

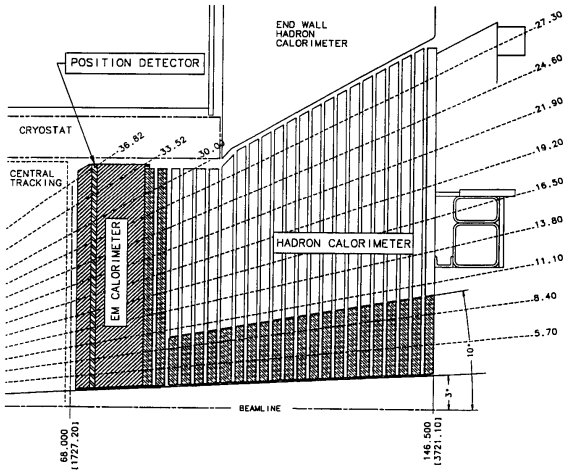

Figure 4.10: A cross-section of the plug calorimeter.

Forward calorimeter

The PEM and PHA sat on the ends of the COT, covering the range of $1.2 \leq |\eta| \leq 3.6$ [11]. The calorimeter divided the towers into 12 groups in η. The innermost four towers grouped in $\eta|$ have 24 wedges in in ϕ (each tower covers 15°). The outermost eight towers in ϕ have 48 wedges in η (each tower covers 8.5°).

Similar to the CEM, the PEM embedded two additional detectors within itself, the Plug Electromagnetic ShowerMax chamber (PES) and the Plug Pre-radiate (PPR) chamber [11]. The PES, like the CES, sat behind six radiation lengths into the PEM and performs the same function as the CES in the forward region. A cross-section of the plug calorimeter appears in Figure 4.10.

4.2.4 Muon sub-detectors

The CDF muon system used in this analysis covered a range of $|\eta| \leq 1.5$. The muon system sat behind several layers of shielding to prevent non-muons from leaking beyond the calorimeters. The muon system was an assortment of wire chambers and scintillators. A brief description follows.

The Central Muon Detector (CMU) sat behind $\approx 5.5\lambda$ of absorber material (the CHA) and provides coverage of $|\eta| \leq 0.6$ [11][12]. The CMU is composed of 144 modules, each consisting of 16 wire chambers, arranged in cylindrical fashion.

The Central Muon Upgrade (CMP) sat behind the CMU and an additional layer of 61 cm of steel [12]. The CMP, also constructed from wire chambers, covered the same range of $|\eta| \leq 0.6$ as the CMU. As opposed to the CMU, the CMP composed roughly a rectangular box surrounding the rest of the CDF detector.

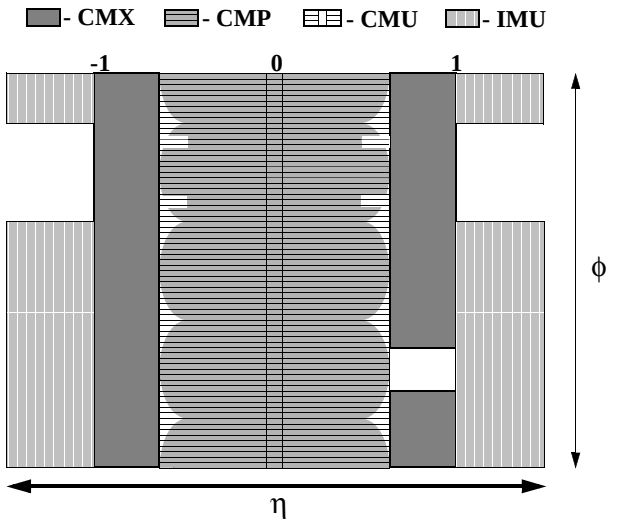

Figure 4.11: The CDF detectors muon coverage. The Intermediate Muon Detector (IMU) corresponds to the CMU in this diagram.

Just on the inside of the CMP, sat the Central Scintillator Upgrade (CSP) [12]. The CSP is a collection of scintillators that assisted with the timing of muon hits in the muon chambers.

The Central Muon Extension (CMX) covered the region $0.6 \leq |\eta| \leq 1.0$ [12]. The CMX consisted of two portions, a conically shaped upper section covering roughly 270°, and a lower planar shaped section covering roughly 90° called the "miniskirt".

On the inside of the CMX (both upper and lower portions), sat the Central Scintillator Extension (CSX) and the Miniskirt Scintillator (MSX) [12]. Both fulfilled the role of the CSP for the CMX.

In the forward region, sat the Barrel Muon Detector (BMU). The BMU, also built from wire chambers, covers the region of $1.0 \leq |\eta| \leq 1.5$ [12]. The chambers assume a cylindrical shape similar to the CMU.

As with the previous muon chambers, a scintillator sat in front of the BMU called the Barrel Scintillator Upgrade (BSU) [12].

A diagram of the CDF muon coverage appears in Figure 4.11.

4.2.5 Cerenkov Luminosity Counters

The Cerenkov Luminosity Counters (CLC) consisted of long, gaseous tubes developed to measure the luminosity of the Tevatron at the CDF interaction point [13]. The CLC counters made use of isobutane gas at atmospheric pressure. The CDF detector divided the CLC into two modules, one for each side of the detector. Each module had 48 tubes divided into three groups of 16 and cover the region of roughly $3.7 \leq |\eta| \leq 4.7$. The tubes pointed back to the interaction point, having photomultiplier tubes on the other

end to detect Cerenkov radiation generated from particle interacting with the gas.

4.3 The CDF II trigger system

The Tevatron operated with a crossing every 396 ns at a frequency of 2.5 MHz. The CDF detector had the ability to write to tape at a rate of only 50 Hz. This required a substantial amount of event rejection, a function performed by CDF's trigger system.

The CDF detector divided the trigger system into three levels: 1, 2, and 3. Levels 1 and 2 were primarily hardware based, while level 3 relied on software run on a PC farm. The trigger system sought to perform the best event reconstruction available at the needed rejection rate.

The CDF trigger system is described in the following section.

4.3.1 Level 1 trigger

The level 1 trigger took information from the calorimeters, the COT, and the muon system to create primatives. The primatives were prospective physics objects such as muons, electrons, or jets constructed from tracks, muon stubs, and calorimeter clusters.

The level 1 trigger made use of several pieces of dedicated hardware. Once piece called the eXtremely Fast Tracker (XFT), took output from the COT to reconstruct tracks. Using the axial superlayers, the XFT began its reconstruction by looking for hits in the COT. After the XFT found hits, the XFT proceeded to link up the hits in order to reconstruct tracks. The XFT had the capability to find tracks with $P_T > 1.5$ GeV/c, placing tracks into 128 bins of p_T and into 288 bins of ϕ with widths of 1.25° .

After finding tracks, the XFT fed the tracks into another set of dedicated hardware called the Extrapolation Unit (XTRP). The XTRP extrapolated the tracks found by the XFT to two subdetectors, the muon system and the calorimeter. The level 1 trigger system could then construct primitives from muon stubs and calorimeter clusters in combination with the extrapolated tracks from the XTRP. This allowed us to implement trigger requirements at level 1 based on muons and electrons having tracks produced in the COT. The electron and muon triggered events we used in the analysis entered in this fashion. The XTRP also distributed tracks further up the trigger system to level 2 to later be used by the Silicon Vertex Trigger (SVT). The SVT will be described in the next subsection.

Other than the aforementioned electron primitive based trigger, the level 1 calorimeter trigger also sought to trigger on jets, photons, missing transverse energy ($\not\!\!E_T$), and total event transverse energy ($\sum E_T$). We divided the calorimeter triggers up into two categories: object triggers for finding objects such as photons

or jets, and global triggers for finding $\not\!\!E_T$ and $\sum E_T$. The object triggers applied thresholds to calorimeter towers while the global triggers applied thresholds to energy summations over all towers. The trigger had the ability to group towers to look for events having two objects such as dijets.

4.3.2 Level 2 trigger

Events that satisfied the requirements at level 1 got passed into level 2 where a more thorough reconstruction is performed. At level 2, further information became available for processing. In particular, information from the silicon detector became available for the level 2 triggers. While we designed the level 1 decision time to be rigid with respect to the bunch crossing rate, the level 2 trigger had a more flexible amount of time to determine whether or not an event should be rejected.

Upon a level 1 accept, the tracking information from the silicon detectors was read out and sent into the SVT. The SVT provided the means to trigger on tracks having high impact parameters. With the long b-hadron lifetime, the tracks produced by a b decay typically have large impact parameters. Many physics signatures produce b-hadrons naturally, such as Higgs events and $t\bar{t}$ events. The SVT allows triggers to look for these signals.

At level 2, data coming from the CES and PES detectors became available. The ShowerMax detectors provided information on electron and photon candidates in the electromagnetic calorimeters.

A dedicated PC held final responsibility for making the level 2 accept for an event. The level 2 PC ran Gentoo linux and took input via FILAR PCI optical fiber link interface cards [14]. A total of three spares had the functionality to replace the main node should it have failed.

4.3.3 Level 3 trigger

Having satisfied the requirements of level 2, the event information moved onward to level 3. The level 3 trigger consisted of a PC farm that performed nearly a complete reconstruction of the events. Objects such as tracks and jets became available that were identical to their offline reconstruction minus the effect of calibrations.

Chapter 5

Object identification

In order to reconstruct decays of $H \rightarrow WW \rightarrow l\nu l\nu$, we first needed to construct identification algorithms to isolate signal events. We started by categorizing leptons based on which sub-detectors they registered in during the event. We catered the cuts applied to each category to increase the likelihood that the candidate lepton is of good quality. We divided the leptons into electrons, muons, and a third group called crack tracks. The crack tracks are lepton candidates which pass through cracks in the calorimeter and leave no hits in the muon chambers.

As mentioned previously, the analysis we present here is an updated version of the previous result over 7.1 fb^{-1}. In addition to the increase in data to 8.2 fb^{-1}, we made a strong effort to improve the analysis itself. With the analysis employing multivariate techniques, we implemented improvements with the primary goal of improving acceptance. The improvements in this version of the analysis focused on improving our lepton identification in order to increase our signal acceptance. We implemented four primary upgrades. Firstly, we evaluated new track and calorimeter isolations for electron and muon candidates. Secondly, we implemented a new category for likelihood based plug electrons. Thirdly, we added a new category specifically to include electrons which pass through cracks in the calorimeter. Finally, we created a new category for muons originating from the CMU sub-detector. During the discussion of lepton identification, the analysis improvements will be introduced.

5.1 Improved isolation

In decays of $H \rightarrow WW \rightarrow l\nu l\nu$, as mentioned earlier, we normally expect the lepton to be isolated, in that there is not a large amount of activity around them in the detector. The isolation, which will be defined in detail later, quantifies this and is evaluated for both track and calorimeter activity. The isolation requirements work as a fairly effective veto of several backgrounds such as $W+$ jets. However, there is a predisposition for the charged leptons to be in close proximity to each other in $H \rightarrow WW \rightarrow l\nu l\nu$ decays.

In decays of the spin 0 scalar H to WW, the two spin 1 W bosons must have a net spin of 0. They can

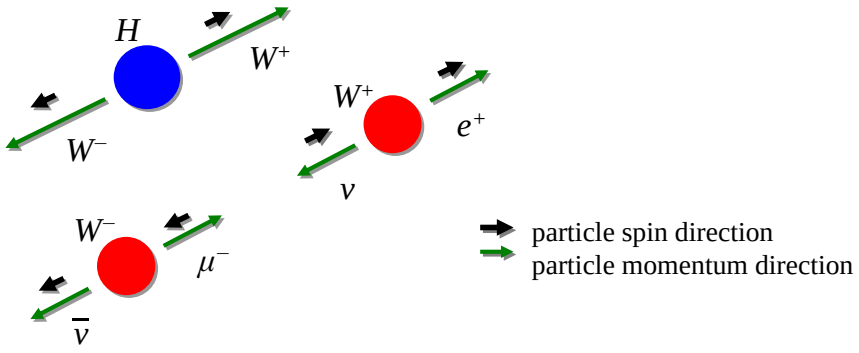

Figure 5.1: An example of the spin correlation resulting in the two charged leptons heading in the same direction. The new track and calorimeter isolations capitalize on the correlation to increase acceptance.

either individually have spin 0 or take on spins in opposite directions. Due to the chirality requirements of the weak interaction, the W^- decays only to left handed charged leptons while the W^+ decays only to right handed charged antileptons. This results in a constraint on the direction in which the charged leptons can move, causing them to prefer the same direction.

For example, if an H decay results in a spin up W^+ and a spin down W^-, the l^+ will move in the same direction as the spin of the W^+ while the l^- will move in the opposite direction of the spin of the W^-. This results in the l^+ and l^- moving in the same direction. In this circumstance, there is a possibility that the l^+ and l^- will spoil the other's or one another's track or calorimeter isolations. A diagram of the spin correlation appears in Figure 5.1.

To prevent mutual isolation spoilage, we reevaluated the isolation quantities for electron and muons by punching out nearby electron or muon candidates in the isolation calculation. A description of the procedure follows.

5.1.1 Electron and muon candidate lists

We started the isolation reevaluation by creating lists of strong muon and electron candidates in an event which could be vetoed from a candidate's isolation. To appear on the list, muons must have met the requirements of $E_{em} < 2 + \text{Max}(0, 0.0115 \times p - 100)$, $E_{had} < 6 + \text{Max}(0, 0.0280 \times p - 100)$, $z_0 < 60$ cm, $p_T > 10$ GeV/c, $d_0 < 0.02$ cm (if track had SVX hits), and $d_0 < 0.20 <$ cm (if track had no SVX hits).

Electrons needed to have a track, $E_{had}/E_{em} < 0.055 + 0.0045 \times (E_{em} + E_{had})$, $z_0 < 60$ cm, and $E_T > 10$ GeV.

Recalculating isolation values requires knowledge of the calorimeter towers corresponding to the muon and electron candidates. To differentiate the towers, CDF assigns two indices to each tower called **iPhi** and **iEta**. The index **iPhi** roughly corresponds to the ϕ coordinate in the detector while **iEta** roughly corresponds to the η coordinate.

The quantities we stored for muons were track number (a unique identification number for the track) and all calorimeter towers they passed through. For electrons, we stored track number and towers belonging to the electron's calorimeter cluster. To construct the electron cluster in the central calorimeter, we stored two towers, one corresponding to the tower where the electrons track entered the calorimeter and the tower adjacent in **iEta** with the highest electromagnetic energy deposit. We took the tower adjacent in **iEta** only since shielding prevents leakage into towers adjacent in **iPhi**. In the forward calorimeter, no shielding between towers in either **iEta** or **iPhi** exists. Because of this, we stored up to three towers for the electron cluster, allowing towers adjacent in both **iPhi** and **iEta**.

5.1.2 Evaluation of the new isolations

With the lists of track numbers and calorimeter towers, we could evaluate the new isolations. To evaluate the isolations, we used the quantity $\Delta R = \sqrt{(\Delta\eta)^2 + (\Delta\phi)^2}$ to measure the spatial separation between two points in η-ϕ space. With ΔR, we defined the original calorimeter isolation for electrons as

$$CalIso = \frac{E_T(\text{in cone of } \Delta R < 0.4) - E_T^e}{E_T^e}, \tag{5.1}$$

where $E_T(\text{in cone of } \Delta R < 0.4)$ is the sum of all energy around the electron cluster's center within a cone of $\Delta R < 0.4$ and E_T^e is the transverse energy of the electron candidate.

To evaluate the new calorimeter isolation, if any tower from the muon or electron lists described above came within the electron's cone of of $\Delta R < 0.4$, we vetoed that tower's energy from being added to $E_T(\text{in cone of } \Delta R < 0.4)$. We conducted the same procedure for the muon calorimeter isolations.

The original electron and muon track isolations are given by

$$TrkIso = \frac{\sum_i p_T^i(\text{in cone of } \Delta R < 0.4) - p_T(e \text{ or } \mu)}{p_T(e \text{ or } \mu)} \tag{5.2}$$

For the new track isolation, if any track from the list described above came within the electron's cone of of $\Delta R < 0.4$, we vetoed that track's p_T from being added to $p_T(\text{in cone of} \Delta R < 0.4)$. We carried out the same procedure for the muon track isolations.

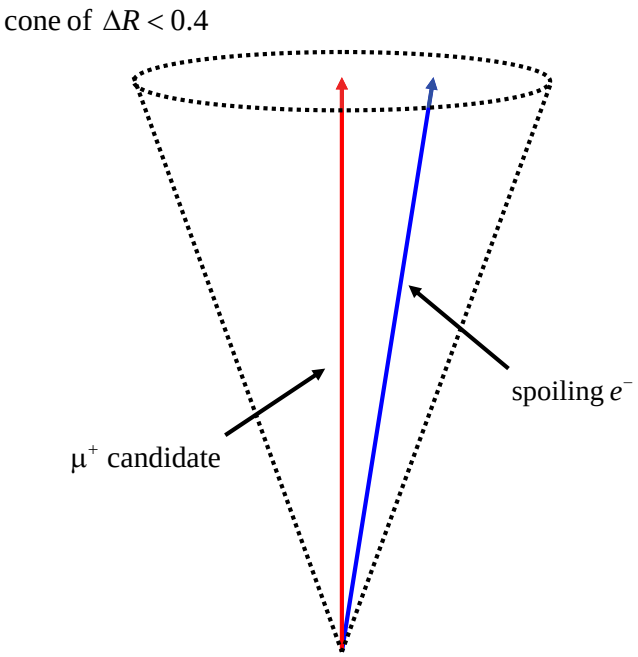

Figure 5.2: A muon candidate's track isolation cone appears here with a spoiling electron. Using the new isolation, the electron's track would be ignored in the track isolation calculation.

An example of a muon candidate's track isolation cone with a spoiling electron appears in Figure 5.2.

5.1.3 Limits of the new isolations

We implemented the new isolation successfully in all of the central electron and muon categories. A difficulty emerged in the forward region with duplicate tracks. In the forward region of the detector, tracks pass through smaller portions of the tracking volume. As a result, charge mismeasurements became frequent. This resulted in duplicate tracks being stored on the lepton lists, the tracks being nearly identical to each other with the exception of charge. As a consequence, we abandoned the new isolation for the forward categories of electrons and muons.

To easily identify the categories which were able to capitalize on the new isolations, we end their names with an uncapitalized "ni".

	TCEni
Region	central
Track p_T	> 10 GeV/c (> 5 GeV/c if $E_T < 20$ GeV/c)
Track $\lvert z_0 \rvert$	< 60 cm
Num. axial SL hits (5 hits)	≥ 3
Num. stereo SL hits (5 hits)	≥ 2
L_{shr}	< 0.2
E_T/p_T	$< (2.5 + 0.015 \times E_T)$
E_{HAD}/E_{EM}	$< 0.055 + 0.00045 \times E$
signed CES Δx	$-3 < q \times \delta X < 1.5cm$
CES $\lvert \Delta z_0 \rvert$	< 3 cm
Fiducial	in CES
NewCalIso	≤ 0.1
NewTrkIso	≤ 0.1
Track	Beam constrained

Table 5.1: The criteria used to define a TCEni electron.

5.2 Electron identification

We constructed electron candidates by matching a track to a cluster deposited in the electromagnetic calorimeter. We considered the electron's mass to be negligible in the determination of the candidate's four momenta. Ignoring the mass of the electron produces an effect on the order of 10^{-8} for the value of the momentum. We constructed the four momenta from momentum information in the tracking sub-detectors and energy information in the calorimeters.

We divided the electron candidates into two categories based on whether they are central (fiducial to the central calorimeter) or forward (fiducial to the forward calorimeter). In both the central and forward divisions, we employed both cut based and likelihood based selections.

5.2.1 Central electrons

The primary central electron category are TCEni (tight central electron) electrons. Being cut based, we required TCEni electrons to pass requirements consistent with quality electrons. These included requiring the electron to be fiducial to the CES detector and implementing cuts on quantities such as E_{had}/E_{em} and E/p. The selection for the TCEni category are summarized in Table 5.1.

As mentioned earlier, we have an additional likelihood based category employed for central electrons called LBEni (likelihood based electron). Electron candidates that fail the TCEni selection have an opportunity to pass into the analysis as an LBEni electron. In building the LBEni category, we needed to first construct the likelihood function. The variables we chose to incorporate are:

- E_{had}/E_{em}: The ratio of the electron's energy deposited in the hadronic calorimeter to the electron's energy deposited in the electromagnetic calorimeter. For a real electron, this quantity is typically small.

- E_T/p_T: Electron's transverse energy divided by the electron track's transverse momentum. For a quality electron, this is expected to be close to unity.
- L_{shr}: Electron's lateral shower profile in the plane transverse to the direction of the electron.
- $CalIso$: Calorimeter isolation as defined previously.
- $TrkIso$: Track isolation as defined previously.
- Signed CES Δx: In the r-ϕplane, the distance between the electron's reconstructed track and the best matching CES cluster times the electron's charge.
- CES Δz: In the r-$z$plane, the distance between the electron's reconstructed track and the best matching CES cluster times the electron's charge.
- COT χ^2: The χ^2 generated from the fit of the COT track.
- Num. axial SL hits: The number of hits from the electron's track in the COT found in axial superlayers.
- Num. stereo SL hits: The number of hits from the electron's track in the COT found in axial superlayers.
- Num. SVX hits: The number of hits from the electron's track SVX sub-detector.

We can then constructed the likelihood as:

$$\mathcal{L}(\overrightarrow{x}) = \frac{L_{sig}}{L_{sig} + L_{bkg}} = \frac{\prod_{i=1}^{N} P_i^{sig}(x_i)}{\prod_{i=1}^{N} P_i^{sig}(x_i) + \prod_{i=1}^{N} P_i^{bkg}(x_i)} \tag{5.3}$$

Here, x_i is the i-th identification variable, N is the total number of variables, $P_i^{sig}(x_i)$ ($P_i^{bkg}(x_i)$) is the i-th probability to find the value of x_i in the given signal (background) likelihood template.

We constructed the signal templates using $Z \rightarrow ee$ events selected from high p_T electron data. We required the Z candidates to fall in the mass range of $76 < M_{ll} < 106$ GeV/c^2. We required one decay leg of the Z to pass the selection for a TCE electron, while requiring the other to be of opposite sign and pass a probe selection described in Table 6.5. A TCE electron is an older version of the aforementioned TCEni electron, identical to a TCEni electron with the exception that it used the old isolations in place of the new. Provided the event passed requirements, the probe electron's variables created the needed templates. In the event that both legs are identified as TCE electrons, we used both electrons in the templates' construction.

Since we did not update the signal templates for the new TCEni category, we fed the new isolation values into the signal templates for the old isolations.

	Central electron probe
Track p_T	> 5.0 GeV/c
Track $\|z_0\|$	≤ 60 cm
Fiducial	Track is to CEM

Table 5.2: The criteria used to define a probe for central electrons.

	Fake central
Fiducial	Track in CES
E_{HAD}/E_{EM}	$< 0.125 + 0.00045 \times E$
CalIso	≤ 0.3
Track p_T	> 10 GeV/c
Track $\|z_0\|$	< 60 cm
Conversion	No
Leading jet	No

Table 5.3: The criteria used to define denominator objects for electrons.

To build the background templates, we looked for faked electrons in a sample of dijet data coming off of a trigger requiring a jet to have $E_T > 20$ GeV. With one jet having $E_T > 20$ GeV, we looked for an additional object which could have faked an electron. We define the "fakeable" object in Table 6.11. We required the pairing of the jet and fake central electron to meet the following criteria:

- The combined jet-fake electron mass must not be in the Z mass range of $76 < M_{ll} < 106$ GeV/c^2.
- The leading jet must have $|z_0| < 60$ cm and $|\Delta z_0(\text{leading jet}, \text{fake electron})| < 4$ cm.

The signal templates have a small background of fake central electrons which we subtracted out by normalizing the background templates to an estimate of the number of fake events entering the signal templates. In the background templates, an amount of signal from $W \to lv$ and $Z \to ll$ enters. To subtract this out, we used a sample of MC for $W \to lv$ and $Z \to ll$ to estimate the amount that enters and to provide templates for the subtraction.

With the templates constructed, we list the final requirements for the LBEni category in Table 5.4.

	LBEni
Region	central
Track p_T	> 10 GeV/c (> 5 GeV/c if $E_T < 20$ GeV/c)
Track $\|z_0\|$	< 60 cm
E_{HAD}/E_{EM}	< 0.125
Fiducial	in CES
NewCalIso	≤ 0.3
Track	Beam constrained
Likelihood ($\mathcal{L}$)	> 0.90

Table 5.4: The criteria used to define a LBEni electron.

	PHX
Region	plug
PES 2-D η	$1.2 < \eta < 2.0$
E_{HAD}/E_{EM}	< 0.05
$PEM\ 3 \times 3\ fit\ tower$	true
$PEM\ \chi^2$	< 10
$PES5 \times 9U$	> 0.65
$PES5 \times 9V$	> 0.65
$CalIso$	< 0.1
$PESPEM\ \Delta R$	< 3.0
$NSVXHits$	≥ 3
Num. SVX hits	≥ 3
Track $\lvert z_0 \rvert$	< 60 cm

Table 5.5: The criteria used to define a PHX.

5.2.2 Forward electrons

As with the central electrons, the forward electrons have a cut based category and a likelihood based category. The cut based category, PHX, introduces candidates by matching a forward track from the SVX with a cluster from the electromagnetic cluster. The cuts used to define the PHX category appear in Table 5.5.

In order to further improve acceptance, we implemented a new category of likelihood based forward electrons for this analysis. The category was previously used in CDF's measurement of the Standard Model $ZZ \rightarrow llll$ cross-section. The new category called plug likelihood-based electrons (PLBE) was based on the LBE category previously incorporated into the analysis. This category did not replace the PHX category used in previous iterations. We implemented the PLBE category to recover forward electrons that failed the PHX criteria.

We build the PLBE likelihood discriminant based on the following information:

- E_T: Electron calorimeter energy projected into the transverse plane.
- Track η: Electron track's η .
- E_T/p_T: Electron's transverse energy divided by the electron track's transverse momentum. For a quality electron, this is expected to be close to unity.
- $CalIso$: Calorimeter isolation as defined previously.
- $TrkIso$: Track isolation as defined previously.
- p_T: Electron track's momentum projected into the transverse plane.
- E_{had}/E_{em}: The ratio of the electron's energy deposited in the hadronic calorimeter to the electron's energy deposited in the electromagnetic calorimeter. For a real electron, this quantity is typically small.

	PLBE
Region	plug
PES 2-D η	$1.2 < \eta < 2.0$
Track $\lvert z_0 \rvert$	≤ 60 cm
NSiHits	≥ 3
E_{HAD}/E_{EM}	< 0.05
CalIso	≤ 0.3
Track	Beam constrained
Likelihood	> 0.70
Orthogonality	Was not already a PHX

Table 5.6: The criteria used to define a PLBE.

- $PES\ \eta$: Electron's η as measured by the PES detector.
- $PESPEM\ \Delta R$: The distance in ΔR between the electron's cluster reconstruction in the PES and the electron's cluster reconstruction in the PEM.
- $PES5 \times 9U$: The ratio of the energy of the five PES U strips in the center of the cluster to the nine total U strips composing the full cluster.
- $PES5 \times 9V$: The ratio of the energy of the five PES V strips in the center of the cluster to the nine total V strips composing the full cluster.
- $PEM\ 3 \times 3\ fit\ tower$: The number of towers used in the comparison of the 3×3 PEM energy distribution compared to the expectation for a real electron.
- $PEM\ \chi^2$: The χ^2 generated from the comparison of the 3×3 PEM energy distribution compared to the expectation for a real electron.
- z_0: Electron track's z_0 .
- $NSVXHits$: The number of hits the electron's track produces in the SVX.
- d_0: Electron track's corrected d_0 .

As with the LBEni category, we can then construct the likelihood using Equation 5.3. Once completed, the likelihood was combined with the cuts shown in Table 5.6 to create the PLBE category. The templates were built in the same manner as in the case of the LBEni category.

5.3 Muon identification

We divided up the muon candidates based on which specific muon subdetect0rs recorded hits during the event. We refer to track segments produced in the muon detectors as stubs. Stubbed muons are muons

	CMUPni
Region	central
Num. axial SL hits (5 hits)	≥ 3
Num. stereo SL hits (5 hits)	≥ 2
Track d_0	< 0.02 cm with > 0 NSiHits or < 0.2 cm with 0 NSiHits
Track $\|z_0\|$	< 60 cm
Track $\chi^2/n.d.f.$	< 4 for runs < 186598 or < 3 for all else
NewCalIso	≤ 0.1
NewTrkIso	≤ 0.1
E_{EM}	$< 2.0 + 0.0115 \times \text{Max}(0, p - 100)$ GeV
E_{Had}	$< 6.0 + 0.0280 \times \text{Max}(0, p - 100)$ GeV
Fiducial	in CMU and CMP
ΔX_{CMU}	< 7 cm
ΔX_{CMP}	$< \text{Max}(6, 150.0/p_T)$ cm

Table 5.7: The criteria used to define a CMUPni.

which produced a stub in a muon subdetector. Additionally, there are a few categories which incorporated muons which do not produce stubs, referred to as stubless muons.

5.3.1 Stubbed muons

We created six categories to handle the stubbed muons. We composed the primary category, CMUPni, of muons producing stubs in both the CMU and CMP muon sub-detectors. The criteria used to select CMUPni muons appear in Table 5.7. We describe candidates registering stubs in the CMP (CMPni) or CMX (CMXni) in Table 5.8. Finally, we describe candidates registering stubs in the CMXMsKs (CMXMsKsni) or BMU (BMU) in Table 5.9.

New for this analysis, we added a new category for muons having hits only in the CMU. The trigger for the CMUni category was only turned on after run 270062. We list the requirements placed on a CMUni muon in Table 5.6.

5.3.2 Stubless muons

We included muons lacking stubs with the requirement that the tracks be minimally ionizing. They are high p_T tracks with only a small amount of energy deposited in the calorimeters. We define two versions, one for central muons (CMIOCESni) and another for forward muons (CMIOPES). Detailed descriptions appear in Table 5.11.

5.4 Crack track identification

We define a third grouping of lepton categories for isolated tracks that pass through cracks in the CES and leave no stubs in the muon chambers. We refer to these as crack tracks. We established two versions. We

	CMPni
Region	central
Num. axial SL hits (5 hits)	≥ 3
Num. stereo SL hits (5 hits)	≥ 2
Track d_0	< 0.02 cm with > 0 NSiHits or < 0.2 cm with 0 NSiHits
Track $\|z_0\|$	< 60 cm
Track $\chi^2/n.d.f.$	< 4 for runs < 186598 or < 3 for all else
NewCalIso	≤ 0.1
NewTrkIso	≤ 0.1
E_{EM}	$< 2.0 + 0.0115 \times \text{Max}(0, p - 100)$ GeV
E_{Had}	$< 6.0 + 0.0280 \times \text{Max}(0, p - 100)$ GeV
Fiducial	in CMP
ΔX_{CMP}	$< \text{Max}(6, 150.0/p_T)$ cm
	CMXni
Region	central
Num. axial SL hits (5 hits)	≥ 3
Num. stereo SL hits (5 hits)	≥ 2
Track d_0	< 0.02 cm with > 0 NSiHits or < 0.2 cm with 0 NSiHits
Track $\|z_0\|$	< 60 cm
Track $\chi^2/n.d.f.$	< 4 for runs < 186598 or < 3 for all else
NewCalIso	≤ 0.1
NewTrkIso	≤ 0.1
E_{EM}	$< 2.0 + 0.0115 \times \text{Max}(0, p - 100)$ GeV
E_{Had}	$< 6.0 + 0.0280 \times \text{Max}(0, p - 100)$ GeV
Fiducial	in CMX
ΔX_{CMX}	$< \text{Max}(6, 125.0/p_T)$ cm

Table 5.8: The criteria we used to define the CMPni and CMXni categories.

	CMXMsKsni
Region	central
Num. axial SL hits (5 hits)	≥ 3
Num. stereo SL hits (5 hits)	≥ 2
Track d_0	< 0.02 cm with > 0 NSiHits or < 0.2 cm with 0 NSiHits
Track $\|z_0\|$	< 60 cm
Track $\chi^2/n.d.f.$	< 4 for runs < 186598 or < 3 for all else
NewCalIso	≤ 0.1
NewTrkIso	≤ 0.1
E_{EM}	$< 2.0 + 0.0115 \times \text{Max}(0, p - 100)$ GeV
E_{Had}	$< 6.0 + 0.0280 \times \text{Max}(0, p - 100)$ GeV
Fiducial	in CMXMsKs
ΔX_{CMP}	$< \text{Max}(6, 125.0/p_T)$ cm
Trigger present for runs	> 227704
	BMU
Region	forward
Num. axial SL hits (5 hits)	≥ 3
Num. stereo SL hits (5 hits)	≥ 2
Track d_0	< 0.02 cm with > 0 NSiHits or < 0.2 cm with 0 NSiHits
Track $\|z_0\|$	< 60 cm
Track $\chi^2/n.d.f.$	< 4 for runs < 186598 or < 3 for all else
CalIso	≤ 0.1
TrkIso	≤ 0.1
E_{EM}	$< 2.0 + 0.0115 \times \text{Max}(0, p - 100)$ GeV
E_{Had}	$< 6.0 + 0.0280 \times \text{Max}(0, p - 100)$ GeV
CalEnergy	≥ 0.1
Num. hits in BMU	> 2
Num. SVX hits	≥ 3
COT hit fraction	> 0.6
Fiducial	in BMU
ΔX_{CMX}	$< \text{Max}(6, 125.0/p_T)$ cm
Valid for runs	> 162312

Table 5.9: The criteria we used to define the CMXMsKsni and BMU categories.

	CMUni
Region	central
Num. axial SL hits (5 hits)	≥ 3
Num. stereo SL hits (5 hits)	≥ 2
Track d_0	< 0.02 cm with > 0 NSiHits or < 0.2 cm with 0 NSiHits
Track $\|z_0\|$	< 60 cm
Track $\chi^2/n.d.f.$	< 3
NewCalIso	≤ 0.1
NewTrkIso	≤ 0.1
E_{EM}	$< 2.0 + 0.0115 \times \text{Max}(0, p - 100)$ GeV
E_{Had}	$< 6.0 + 0.0280 \times \text{Max}(0, p - 100)$ GeV
Fiducial	Not in CMX or CMP
ΔX_{CMU}	< 7 cm
Trigger present for runs	> 270062

Table 5.10: The criteria used to define a CMU.

	CMIOCESni
Region	central
Num. axial SL hits (5 hits)	≥ 3
Num. stereo SL hits (5 hits)	≥ 3
Track d_0	< 0.02 cm with > 0 NSiHits or < 0.2 cm with 0 NSiHits
Track $\|z_0\|$	< 60 cm
Track $\chi^2/n.d.f.$	< 3
NewCalIso	≤ 0.1
NewTrkIso	≤ 0.1
E_{EM}	$< 2.0 + 0.0115 \times \text{Max}(0, p - 100)$ GeV
E_{Had}	$< 6.0 + 0.0280 \times \text{Max}(0, p - 100)$ GeV
$E_{HAD} + E_{EM}$	< 0.1 GeV
Fiducial	in CES

	CMIOPES
Region	central
Track d_0	< 0.02 cm with > 0 NSiHits or < 0.2 cm with 0 NSiHits
Track $\|z_0\|$	< 60 cm
NewCalIso	≤ 0.1
NewTrkIso	≤ 0.1
E_{EM}	$< 2.0 + 0.0115 \times \text{Max}(0, p - 100)$ GeV
E_{Had}	$< 6.0 + 0.0280 \times \text{Max}(0, p - 100)$ GeV
$E_{HAD} + E_{EM}$	< 0.1 GeV
COT hit fraction	> 0.6
Fiducial	in PES

Table 5.11: The criteria we used to define the CMIOCESni and CMIOPES categories.

	CrkTrk
Num. axial SL hits (5 hits)	≥ 3
Num. stereo SL hits (5 hits)	≥ 3
Track d_0	< 0.02 cm with > 0 NSiHits or < 0.2 cm with 0 NSiHits
Track $\|z_0\|$	< 60 cm
Track $\chi^2/n.d.f.$	< 3
CalIso	≤ 0.1
TrkIso	≤ 0.1
Fiducial	Not in CES or PES

Table 5.12: The criteria used to define a IsoCrkTrk.

	IsoCrkTrk
NAxL (5 hits)	≥ 3
NStL (5 hits)	≥ 3
Track d_0	< 0.02 cm with > 0 NSiHits or < 0.2 cm with 0 NSiHits
Track $\|z_0\|$	< 60 cm
Track $\chi^2/n.d.f.$	< 3
CalIso (optimized for IsoCrkTrk)	≤ 0.1
TrkIso	≤ 0.1
Fiducial	Not in CES or PES

Table 5.13: The criteria used to define a IsoCrkTrk.

used one, CrkTrk, for more muon like crack tracks. The description of CrkTrk appears in Table 5.12. We used another, IsoCrkTrk, which is new to the analysis and attempted to recover electrons passing through calorimeter tracks. We present a more detailed description of IsoCrkTrk below.

5.4.1 IsoCrkTrk category

As described above, the CrkTrk category placed a requirement on calorimeter isolation. This calorimeter isolation requirement has the potential to spoil quality electrons however. If an electron passed through a calorimeter crack and produced a shower in the electromagnetic calorimeter, the shower would result in the electron failing the calorimeter isolation. Additionally, an electron could radiate a photon before passing through a calorimeter crack, also resulting in the electron failing the calorimeter isolation criteria.

To reincorporate these electrons, we created the new IsoCrkTrk category. If an electron were to pass through a crack, either the electron's shower or the shower produced by the radiated photon would likely create energy deposits in the four nearest calorimeter towers. In order to recover these candidates during the isolation calculation, we left out the nearest four towers' electromagnetic energy in the E_T(in cone $\Delta R < 0.4$) sum. We show an example of an electron entering a crack and depositing energy in the calorimeter in Figure 5.3.

As with the PLBE category, IsoCrkTrk does not replace the CrkTrk category. Only candidates that fail the CrkTrk criteria qualify to be reclassified as IsoCrkTrk's. We list the requirements placed on IsoCrkTrk leptons in Table 5.13.

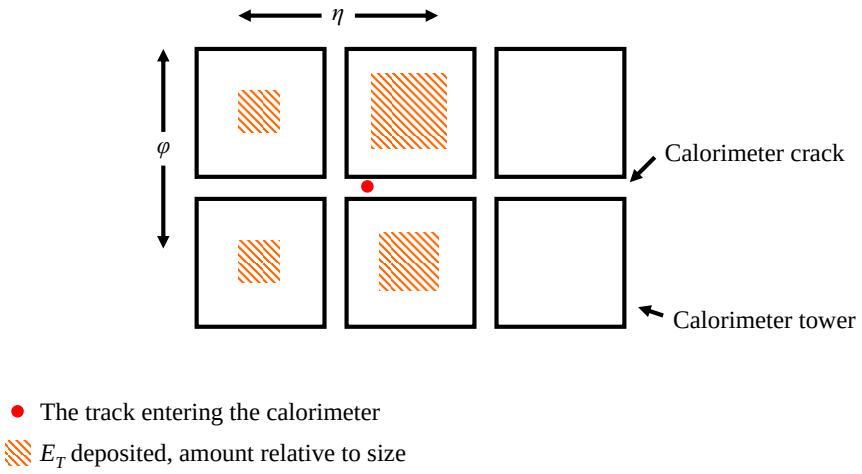

Figure 5.3: An example of an electron entering a crack and depositing energy into the calorimeter. The size of the orange boxes correspond to the amount of E_T deposited in the respective tower. The four towers with energy deposites would not enter the calorimeter isolation calculated specifically for the IsoCrkTrk catergory.

5.5 Jet identification

5.5.1 Jet clustering algorithm

We reconstruct jets using a clustering algorithm described in Reference [15]. The algorithm creates a list of seed towers having $E_{Ti} = E_i \sin(\theta_i) > 1$ GeV, where E_i is the energy deposited in the i-th tower and θ_i is the azimuthal angle of the center of the i-th tower. The algorithm then ranks them in order of E_{Ti}. Starting with the tower having the highest E_T, the algorithm builds a precluster around the center of the seed towers using neighboring towers whose centers lie within $\Delta R < 0.4$ of the seed. Note that once the algorithm includes a seed tower in one jet cluster, we do not assign it to another.

Once the algorithm forms preclusters, it loops over them to create clusters. Using the towers in the preclusters, the algorithm finds new centers in η and ϕ by using the weighted tower transverse energies. The algorithm then examines all towers in the new ΔR cone around the new cluster center. The algorithm now adds in all towers in the cone with $E_T > 100$ MeV into the cone. The algorithm keeps any towers that were previously in the precluster, even if they fall out of the new ΔR cone. The algorithm repeatedly runs over the clusters, determining their new centers and adding towers, until the clusters stabilize.

There are several instances of overlap which can cause difficulties. For instance, the towers of a cluster can be contained entirely within another cluster. In this event, the algorithm drops the cluster with the lowest E_T. In another instance, the clusters can partially overlap. To correct this, the algorithm evaluates

an overlap fraction defined as the sum of the E_T of the overlapping towers divided by the total E_T of the smaller cluster. If the overlap fraction is above 0.75, the two clusters get merged into one. If it is less than 0.75, the algorithm assigns overlapping towers to the cluster having the closest center.

5.5.2 Jet energy correction

The calorimeter is not uniform in its ability to measure jet energies as a function of pseudorapidity. This arises from separations in the calorimeter that occur at $\eta = 0$ and again where the central and plug meet at roughly an $|\eta|$ of 1.1. Additionally, further η dependencies arise from the central and plug calorimeters displaying different responses from each other. To correct for this effect, we scaled the response of the calorimeter outside of the region of $0.2 < |\eta| < 0.6$ to be consistent with the response in the region of $0.2 < |\eta| < 0.6$ [15]. We chose the region of $0.2 < |\eta| < 0.6$ since it lies far from cracks and is well covered by instrumentation. We determined the correction by using dijet events and balancing them against each other in E_T.

We needed a further jet energy correction to cover nonlinear response and uninstrumented regions of the calorimeter. To produce this correction, we used a finely tuned set of PYTHIA MC samples to determine the needed scaling based on the measured jet energy in the calorimeter versus the energy of the hadron level jet [15]. We took great care to make sure that the simulation accurately modeled calorimeter response to single particles such as pions or kaons. We incorporated systematic uncertainties, taking into account the MC's ability to model single particle response and fragmentation resulting from hadronization.

As the luminosity in the CDF detector increases, the average number of $p\bar{p}$ interactions per bunch crossing, $\langle N \rangle$, also increases. At a luminosity of $\mathcal{L} = 40 \times 10^{30}$ cm^{-2}s^{-1}, the average number of $p\bar{p}$ is around one. When the luminosity increases to $\mathcal{L} = 100 \times 10^{30}$ cm^{-2}s^{-1}, $\langle N \rangle$ increases to three and goes up to eight when $\mathcal{L} = 300 \times 10^{30}$ cm^{-2}s^{-1}. The multiple interactions have the effect of increasing the jet energy by introducing background hadrons into the jet's cone in the calorimeter. To correct for this, we use the number of reconstructed z-vertices, N_{vtx}, as an estimate of the number of interactions. We determined the correction itself using minimum bias data and randomly selecting seed towers to construct a cluster within a ΔR cone of 0.4. We then averaged the energy within the cone over many events as a function of $\langle N_{vtx} \rangle$. We applied the correction as determined by the event's N_{vtx}.

5.6 Missing transverse energy

Missing transverse energy ($\not\!\!E_T$) is the final object necessary for the analysis. Missing transverse energy enters from the neutrinos resulting from the leptonically decaying W bosons. Normally, if all products of a collision are detected, we expect the vector sum of the transverse energy E_T to be zero. The CDF detector lacks the ability to register neutrinos. As a result, a nonzero vector sum of E_T is typically found in the presence of neutrinos.

In this analysis, we define $\not\!\!E_T$ as follows:

$$\not\!\!E_T = |\sum_i E_{T,i}\hat{n}_{T,i}|, \tag{5.4}$$

where $\hat{n}_{T,i}$ is the transverse component on the unit vector pointing from the interaction point to the i-th calorimeter tower. We apply a correction to $\not\!\!E_T$ to account for muons which do not dump all of their energy into the calorimeter and for tracks which pass through regions of the calorimeter without instrumentation.

Chapter 6

Base event selection, backgrounds, and modeling

6.1 Base event selection

The decays of the Higgs in $H \to WW \to l\nu l\nu$ provides us with several handles for event selection, namely the two charged leptons and the two neutrinos. To identify these events, we looked for two opposite sign high p_T leptons and missing energy ($\not\!\!E_T$) corresponding to neutrinos the CDF detector does not measure. On triggered leptons, we required electron candidates to have $E_T > 20$ GeV and muons to have $p_T > 20$ GeV/c. For the nontriggered leptons, we required electron candidates to have $E_T > 10$ GeV and muons to have $p_T > 10$ GeV/c. Additionally, we required the z-positions of the leptons at closest approach to the beam line to be within 4 cm of each other.

As for the dilepton pairs taken, we selected e-e, e-μ, μ-μ, e-track, and μ-track. Here, "e" and "μ" represent the electron and muon categories established in the last chapter; "track" refers to leptons in the CrkTrk and IsoCrkTrk categories of whose flavor we are not able to identify.

Drell-Yan (DY) backgrounds consisting of $p\bar{p} \to Z \to ll$ are not expected to exhibit $\not\!\!E_T$ in significant quantities. However, the detector's energy resolution is not perfect. As a result, $\not\!\!E_T$ can appear in DY events from the mismeasurement of jet or lepton energy. To suppress the Drell-Yan background, we defined a variable called $\not\!\!E_{T\,spec}$, expressed as follows:

$$\not\!\!E_{T\,spec} = \begin{cases} \not\!\!E_T & \text{if } \Delta\phi(\not\!\!E_T, \text{nearest lepton or jet}) > \pi/2 \\ \not\!\!E_T \sin(\Delta\phi(\not\!\!E_T, \text{nearest lepton or jet})) & \text{if } \Delta\phi(\not\!\!E_T, \text{nearest lepton or jet}) < \pi/2 \end{cases}. \tag{6.1}$$

We required $\not\!\!E_{T\,spec} > 25$ GeV for electron-electron and muon-muon pairs. For electron-muon pairs, since they do not originate from DY, we loosened the requirement to $\not\!\!E_{T\,spec} > 15$ GeV. Since the DY background enters primarily from the mismeasurement of lepton or jet energy, the $\not\!\!E_{T\,spec}$ cut places an increasingly stricter requirement on $\not\!\!E_T$ the more collinear $\vec{\not\!\!E}_T$ gets to a jet or lepton. This significantly lowers the efficiency of DY events entering the analysis.

silicon good	muon chambers good	CMX/CMXMsKs good	luminosity (pb^{-1})
no	no	no	8,250
yes	no	no	7,960
no	yes	no	8,178
no	yes	yes	8,013
yes	yes	no	7,896
yes	yes	yes	7,737

Table 6.1: The luminosity of the sample for each required component.

To suppress a background from $W\gamma$ as well as heavy flavor decays such as Υ resonances, we required an invariant dilepton mass of $M_{ll} > 16$ GeV/c^2. There is a subanalysis that looks specifically in the $M_{ll} < 16$ GeV/c^2 region. That analysis will be described briefly later on. To suppress a background from WZ production, we required the two selected leptons to have opposite sign. As with the M_{ll} cut, there is a subanalysis that looks explicitly for two same sign leptons resulting from $WH(H \rightarrow WW) \rightarrow l\nu l\nu l\nu$ and $ZH(H \rightarrow WW) \rightarrow lll\nu l\nu$. That analysis will also be described briefly later on.

We divided the events in the analysis into three bins based on jet content: 0 jets, 1 jet, and 2 or more jets. For jets, we require $E_T > 15$ GeV and $|\eta| < 2.5$.

With the CDF detector being comprised of several sub-detectors, it is not always possible to keep all components operational at all times. If one component is malfunctioning, data can still be taken with the remaining functional components. Running in a compromised state though has an impact on which components of the detector can safely be included in an analysis. For example, if the CMU muon chamber is nonoperational, no muons making use of the CMU should be included. To guarantee that analyses use the correct components, CDF has lists of runs (good run lists) for which different combinations of components were in operational order. We required events to appear on a good runs list that had the relevant detector components operations. We list the luminosities for different combinations of active components in Table 6.1.

The cuts applied in the analysis are summarized as:

- Require two high p_T, opposite sign leptons, with $p_T > 20$ GeV/c for the triggered lepton and a $p_T > 10$ GeV/c for the nontriggered lepton
- Require the z-positions of the leptons at closest approach to the beam line to be within 4 cm of each other
- Select e-e, e-μ, μ-μ, e-track, and μ-track combinations
- Require $\not\!\!E_{T\,spec} > 25$ GeV for ee and $\mu\mu$ and $\not\!\!E_{T\,spec} > 15$ GeV for $e\mu$
- Require the dilepton mass $M_{ll} > 16$ GeV/c^2

- For jets in the analysis, require them to have $E_T > 15$ GeV and $|\eta| < 2.5$
- The event must also appear on the relevant good runs list for the needed detector components

6.2 Backgrounds and modeling

Several backgrounds emerge in the dilepton plus $\not\!\!E_T$ final state. We list below how each background enters and rough estimates of their expected contributions:

- WW: The production of a WW pair from $p\bar{p} \to WW$ represents the largest background in the analysis with an expected contribution of 40 percent. It is very similar to the signal with the W bosons decaying to lv.
- WZ and ZZ: Additional diboson production also enters with an expectation of roughly 3 percent each for WZ and ZZ.
- $W+$ jets: A background of $W+$ jets emerges when the W boson decays leptonically and a jet ends up faking a lepton. The expected contribution of this background is around 15 percent. The modeling of this background is driven by data.
- $W + \gamma$: This background comes into the analysis when the W boson decays leptonically and the γ undergoes a conversion, accounting for about 10 percent. In a photon conversion, the process $\gamma \to e^+e^-$ occurs and one of the electrons is lost.
- $t\bar{t}$: The $t\bar{t}$ background enters in the portion of the analysis using two or more jets and accounts for roughly 13 percent.
- DY: The Drell-Yan background enters when accompanied by $\not\!\!E_T$ and constitutes roughly 16 percent of the background.

6.3 Monte Carlo simulations

Ideally, we would be able to provide clean, data driven models for all the backgrounds listed above. Unfortunately, with the exception of the $W+$ jets background, it's not feasible. This forced us to rely on simulations (Monte Carlo or MC) designed to model the backgrounds as accurately as possible. We go through great lengths to check modeling out as thoroughly as possible. We employ several control regions to cross-check our modeling.

The MC simulation pass through three phases of simulation:

- Generator
- Detector simulation
- Trigger efficiency and incorporation

Each of these will be described briefly below.

6.3.1 Generator level simulation

The generator level MC lies at the very heart of the MC used in the analysis. The generator level MC models the $p\bar{p}$ collision and the particles produced in the immediate physics process. For example in case of the WW background, the generator handles the underlying process consisting of $p\bar{p} \rightarrow WW \rightarrow lvlv$.

We modeled the WZ, ZZ, $t\bar{t}$, and DY MC samples with the PYTHIA generator [16]. The PYTHIA generator models the parton distributions of the proton-antiproton pairs to leading order. The parton distribution functions model the probability of finding a parton with a certain momentum after a hard scatter. The PYTHIA generator is also responsible for modeling initial state radiation, final state radiation, and hadronization. We modeled any other physics processes that result from the $p\bar{p}$ collision with PYTHIA.

We modeled the $W + \gamma$ background with the Baur generator [17]. We found the Baur generator demonstrated better modeling of the QED radiation associated with these events. We then fed the results of the Baur MC generation into the PYTHIA generator to complete the samples.

To produce the most dominate background WW, we used the next-to-leading order generator MC@NLO [18]. To generate the samples used, the output from the MC@NLO generation was fed into the HERWIG generator [19] to handle parton showers.

The production of the MC samples is rather computationally intensive. In order to make the production more reasonable, we applied cuts to the generated samples to veto the full generation of events which would not normally be expected to appear in the analysis. For the DY samples ($q\bar{q} \rightarrow Z \rightarrow ll$), we placed cuts on the dilepton mass of $M_{ll} > 20$ GeV/c^2. We generated additional DY samples to fill gaps created by the cut, generating for $10 < M_{ll} < 20$ GeV/c^2. The $W + \gamma$ samples required $p_T(\gamma) > 5$ GeV/c and $\Delta R(lepton, \gamma) > 0.2$. We accounted for the effects of these cuts through efficiency corrections applied to the samples.

For signal MC, we incorporated Higgs production from three mechanisms: gluon fusion, associated production, and vector boson fusion. Gluon fusion is by far the dominate mode of production used in the anlaysis. The gluon fusion cross-section ($\sigma_{gg \rightarrow H}$) we used has been calculated to next-to-next-to-leading log [20][21]. We incorporated corrections for electroweak effects from [22][23]. For associated Higgs production ($\sigma_{q\bar{q}' \rightarrow WH}$

sample	period	$\sigma \times \mathcal{B}(pb)$	filter efficiency
$W\gamma \to l\nu\gamma$	0-32	32.38× 0.5	1.0
WW	0-32	11.66× 0.1027	1.0
WZ	0-32	3.46× 0.101	0.754
ZZ	0-32	1.511	0.233
$t\bar{t}$	0-11	7.04× 0.1027	1.0
$Z \to ll$ ($M_{ll} > 20$ GeV/c^2)	0-27	355	1.0
$Z \to ee$ ($10 < M_{ll} < 20$ GeV/c^2)	0-11	920	0.0156
$Z \to \mu\mu$($10 < M_{ll} < 20$ GeV/c^2)	0-11	920	0.0156
$Z \to \tau\tau$($10 < M_{ll} < 20$ GeV/c^2)	0-11	1272	0.00713
$gg \to H \to WW$	0-32	0.397	1.0
$q\bar{q}' \to WH \to WWW$	0-32	0.046	0.7108
$q\bar{q} \to ZH \to ZWW$	0-32	0.030	0.7172
$q\bar{q}(') \to q\bar{q}(')H \to q\bar{q}(')WW$	0-32	0.035	1.0

Table 6.2: A description of the samples used in the analysis for the background and signal. The filter efficiency refers to the efficiency of the cuts applied at generator level. The values given for Higgs production all assume a Higgs mass of 160 GeV/c^2.

and $\sigma_{q\bar{q}\to ZH}$), we used cross-sections as determined from [24], which begin with a next-to-leading order calculation and incorporates next-to-next-to-leading order QCD corrections from [25]. as well as electroweak corrections from [26]. In the case of vector boson fusion ($\sigma_{q\bar{q}(')\to q\bar{q}(')H}$), we determined the production cross-section also from [27]. We caculated electroweak corrections to the vector boson cross-section using the HAWK program [28]. To determine the Higgs branching ratios, we used the HDECAY program [29]. To maximize sensitivity at each Higgs mass, we generated MC samples for 19 Higgs masses running from 110-200 GeV/c^2, in increments of 5 GeV/c^2.

A description of the background and signal samples used in the analysis appear in Table 6.2.

6.3.2 Detector simulation

Once the generator level MC has been run, we fed the results consisting of particle positions and four-momenta into another level of simulation. The detector simulation models the physics processes as they would occur in the physical detector. Many of the aspects of the detector are simulated at this level. These include luminosity, beam position, particle-detector interactions and sub-detector condition. As an example, the photon produced in a simulated $W + \gamma$ event might convert to an electron-antielectron pair. This is an effect that would be modeled at this stage of the MC sample creation.

The CDF detector simulation is based on the GEANT MC program [30].

6.3.3 Trigger efficiency and incorporation

In order to incorporate the generated samples into the anlaysis, we give the MC samples a per event weight of

$$weight = \frac{\sigma \times \mathcal{B} \times \epsilon_{filter} \times \epsilon_i^{trigger} \times s_i^{lepton} \times \epsilon_{vertex} \times \mathcal{L}_i}{N_i^{generator}(|z_0| < 60 \text{ cm})}, \tag{6.2}$$

for

- σ: The cross-section for the MC process being modeled
- $\mathcal{B}$: The braching ratio for the MC process being modeled
- ϵ_{filter}: The filter efficiency originating from cuts applied at generator level
- ϵ_i^{trgger}: The relative trigger efficiency for the i-th lepton cetegory, described in more detail below
- s_i^{lepton}: The scale factor for the i-th lepton category, described in more detail in the next section
- ϵ_{vertex}: The efficiency of the $|Z|$-vertex position requirement which depends on run number
- $\mathcal{L}_i$: The luminosity for the i-th lepton category as determined from the necessary good runs list
- $N_i^{generator}(|z_0| < 60 \text{ cm})$: The number of generated events which meet the requirement of $(|z_0| < 60 \text{ cm})$

We measured the needed trigger efficiency from data using a tag and probe method was used. The exercise took a $Z \to ll$ data sample in the range of $76 < M(ll) < 106$ GeV/c^2, requiring electrons (muons) to have an $E_T(P_T) > 20$ GeV/c. To measure the efficiency, we identfified a trigger confirmed muon or electron. Trigger confirmed refers to a lepton which was confirmed as having fired the trigger to accept the event. We then sought a second muon or electron, which either did or did not fire the trigger in the process of decaying from the Z to check trigger efficiency.

6.4 Efficiencies and DY cross-sections

One difficulty in modeling the data with MC simulations arises from differences in the lepton identification efficiency between data and MC samples. To account for this, we measured efficiencies for each lepton type, for both data and MC samples. We then took efficiency ratios and applied them to the MC samples, to properly account for the efficiency differences. We refer to this correction as s_i^{lepton}.

6.4.1 Measurement of efficiencies and scale factors

To evaluate the lepton efficiencies, we used a tag and probe method using electrons and muons from Z candidates. We selected Z decays in which one of the legs passes a full selection (referred to as a *tag*-leg) and the other a base selection (referred to as a *probe*-leg). This then allows a determination of the efficiency for a final lepton selection (referred to as a *tight*-leg). Depending on the lepton type, the *tag*- and *tight*-legs may or may not be the same lepton selection.

With the following notation:

- V: corresponds to the *tag*-leg
- T: corresponds to *tight*-legs which are not already a *tag*-leg, this is the selection being measured
- F: corresponds to the *probe*-leg

we can then define the efficiency as:

$$\epsilon = \frac{2 \times N_{VV} + N_{VT}}{2 \times N_{VV} + N_{VT} + N_{VF}}. \tag{6.3}$$

Here, N_{VV} is the number of candidates with two *tag*-legs; N_{VT} is the number of candidates with one *tag*-leg and one *tight*-leg; and N_{VF} is the number of candidates with one *tag*-leg and one *probe*-leg.

In the instance that the *tag*-leg is the selection whose efficiency is being measured, the efficiency becomes

$$\epsilon = \frac{2 \times N_{VV}}{2 \times N_{VV} + N_{VF}}. \tag{6.4}$$

As an example, for an LBEni, we required the *tag*-leg to be a TCEni while requiring the *tight*-leg to be an LBEni. In this instance, we used equation 6.7. Alternatively, for a TCEni, the *tag*-leg is a subset of the *tight*-leg, and we made use of equation 6.4.

For the *probe*-legs, we defined four selections for electrons and two for muons. The central electron selection is listed in Table 6.5. For forward electrons, we divided up the efficiency into two components, one for forward tracking (PHXTrk) and another for electromagnetic calorimeter identification (PHXPEM). The criteria for the two froward electron probes are listed in Table 6.6. For central muons and forward muons, the criteria are listed in Table 6.7.

The list of lepton selections and their probe and tag legs are listed in Table 6.3 for electrons and Table 6.4.

For CrkTrk and IsoCrkTrk, we evaluated efficiencies for muons and electrons separately and then combined them.

lepton selection	tag leg	probe leg
LBEni	TCEni	central electron probe
TCEni	TCEni	central electron probe
PHXTrk	TCEni	probe PHXTrk
PHXPEM	TCEni	probe PHXPEM
PLBEPEM	TCEni	probe PHXPEM
CrkTrk e	TCEni	probe CMIOCentral
IsoCrkTrk e	TCEni	probe CMIOCentral

Table 6.3: The efficiencies and resulting scale factors averaged over the full data set.

lepton selection	tag leg	probe leg
CMUPni	CMUPni	probe CMIOCentral
CMUni	CMUPni	probe CMIOCentral
CMPni	CMUPni	probe CMIOCentral
CMXni	CMUPni	probe CMIOCentral
CMXMsKsni	CMUPni	probe CMIOCentral
BMU	CMUPni	probe CMIOForward
CMIOCESni	CMUPni	probe CMIOCentral
CMIOPES	CMUPni	probe CMIOForward
CrkTrk μ	CMUPni	probe CMIOCentral
IsoCrkTrk μ	CMUPni	probe CMIOCentral

Table 6.4: The efficiencies and resulting scale factors averaged over the full data set.

	Central electron probe
Track p_T	> 5.0 GeV/c
Track $\lvert z_0 \rvert$	≤ 60 cm
Fiducial	Track is to CEM

Table 6.5: The criteria used to define a probe for central electrons.

	PHXPEM
E_{HAD}/E_{EM}	< 0.125
$\lvert PES\ \eta \rvert$	> 1.2 and < 2.0
Track $\lvert z_0 \rvert$	≤ 60 cm
NSvxHits	≥ 3

	PHXTrk
E_{HAD}/E_{EM}	< 0.125
$\lvert PES\ \eta \rvert$	> 1.2 and < 2.0
Track $\lvert z_0 \rvert$	≤ 60 cm
NSvxHits	≥ 3
CalIso	≤ 0.1
$PESPEM\ \Delta R$	< 3.0
$PES5 \times 9U$	> 0.65
$PES5 \times 9V$	> 0.65
$PEM\ 3 \times 3\ fit\ tower$	> 1.0
$PEM\ \chi^2$	< 10

Table 6.6: The criteria used to define probes for PHX and PLBE electrons.

	CMIOCentral
NAxL (5 hits)	≥ 2
NStL (5 hits)	≥ 2
Track $\lvert z_0 \rvert$	≤ 60 cm
Fiducial	Not in PES

	CMIOForward
Track $\lvert z_0 \rvert$	≤ 60 cm
Fiducial	in PES
COT hit fraction	> 0.6

Table 6.7: The criteria used to define a probe for central (CMIOCentral) and forward (CMIOForward) muons.

Average over full run range

	data efficiency	MC efficiency	Scale Fac
LBEni	0.117 ± 0.001	0.098 ± 0.000	1.162 ± 0.007
TCEni	0.773 ± 0.001	0.804 ± 0.000	0.971 ± 0.001
PHXTrk	0.872 ± 0.001	0.857 ± 0.000	1.021 ± 0.001
PHXPEM	0.804 ± 0.001	0.874 ± 0.000	0.932 ± 0.001
PLBEPEM	0.121 ± 0.001	0.084 ± 0.000	1.343 ± 0.011
CrkTrk e	0.599 ± 0.003	0.719 ± 0.001	0.851 ± 0.004
IsoCrkTrk e	0.231 ± 0.002	0.166 ± 0.001	1.314 ± 0.015
CMUPni	0.777 ± 0.002	0.887 ± 0.000	0.883 ± 0.002
CMUni	0.765 ± 0.006	0.878 ± 0.003	0.872 ± 0.007
CMPni	0.771 ± 0.005	0.904 ± 0.001	0.855 ± 0.005
CMXni	0.870 ± 0.003	0.905 ± 0.001	0.966 ± 0.003
CMXMsKsni	0.771 ± 0.006	0.896 ± 0.001	0.864 ± 0.007
BMU	0.728 ± 0.005	0.710 ± 0.001	1.035 ± 0.007
CMIOCESni	0.253 ± 0.001	0.259 ± 0.000	1.160 ± 0.007
CMIOPES	0.551 ± 0.003	0.594 ± 0.001	0.943 ± 0.006
CrkTrk μ	0.589 ± 0.002	0.679 ± 0.001	0.956 ± 0.004
IsoCrkTrk μ	0.010 ± 0.001	0.007 ± 0.000	1.232 ± 0.082

Table 6.8: The efficiencies and resulting scale factors averaged over the full data set.

In evaluating the values of N_{VV}, N_{VT}, and N_{VF} from reconstructed $Z \to ll$, we employed sideband subtraction. We take the signal region as $76 < M(ll) < 106$ and the background region as $61 < M(ll) < 76$ GeV/c$^2 \cup 106 < M(ll) < 121$ GeV/c^2.

With the efficiencies finished, we evaluated the scale factors to be applied to the MC samples as:

$$s_i^{lepton} = \frac{\epsilon_i^{data}}{\epsilon_i^{MC}}. \tag{6.5}$$

We divided the total dataset into nine sections (run periods) based on run number and the efficiencies and scale factors were evaluated in each section. This allowed the MC sample representing a specific run period to be multiplied by a more accurate scale factor. The efficiencies and scale factors averaged over the full data set appear in Table 6.8.

6.4.2 DY cross-section measurement

One of the strongest crosschecks of the analysis is the DY control region. This control region provides a strong indication that we correctly implemented the new lepton categories and the new isolation. It additionally can indicate we performed our background modeling correctly. The control region aims to reconstruct $p\bar{p} \to Z \to l^+l^-$ for l being either an electron or muon. We required $76 < m(ll) < 106$ GeV/c^2, $\not\!\!E_T < 15$ GeV for $e\mu$ events, and $\not\!\!E_T < 25$ GeV for all others. We also required the event to appear on a good runs list, $\Delta z_0(ll) < 4$ cm, passed cosmic ray veto, and a trigger confirmed lepton.

Using the modeling described above, the expected and observed yields for the DY control region appear

Category	WW	WZ	ZZ	$t\bar{t}$	DY	$W\gamma$	W+jets	Total	Data
e e	21.0	135.5	122.0	5.6	371364.8	5.1	1154.1	372808.2	345852.0
e μ	18.4	0.4	0.2	4.0	334.1	1.5	75.2	433.9	356.0
μ μ	17.2	91.5	85.8	4.3	245931.8	0.0	1043.9	247174.5	242994.0
e trk	15.9	39.7	36.8	4.1	106188.1	1.0	5142.2	111427.8	99665.0
μ trk	9.7	26.0	23.9	2.5	70191.5	0.1	4186.3	74440.0	66644.0
Total:	82.2	293.1	268.7	20.5	794010.3	7.8	11601.6	806284.2	755511.0

Table 6.9: Predicted and observed yields in the Drell-Yan Region.

Category	DY MC	Data	Data/MC	DY x-sec (pb) ± stat.	Residual [σ]
TCEni	537551.7	506198	0.94	236.65 ± 0.35	-11.7
LBEni	88021.2	84849	0.96	242.25 ± 0.89	1.7
PHX	169682.5	158101	0.93	234.15 ± 0.61	-10.9
PLBE	31026.7	28276	0.91	229.03 ± 1.44	-8.1
CMUPni	231953.7	227949	0.98	246.97 ± 0.54	11.5
CMUni	24608.1	23933	0.97	244.41 ± 1.82	2.0
CMPni	35349.8	35667	1.01	253.56 ± 1.42	9.0
CMXni	118983.4	114080	0.96	240.95 ± 0.75	0.3
CMXMsKsni	22738.2	23125	1.02	255.58 ± 1.78	8.3
BMU	18458.4	17899	0.97	243.69 ± 1.90	1.5
CMIOCESni	72806.8	74145	1.02	255.92 ± 0.99	15.4
CMIOPES	37490.8	36190	0.97	242.59 ± 1.33	1.4
CrkTrk	129226.7	120993	0.94	235.29 ± 0.70	-7.8
IsoCrkTrk	32690.9	34011	1.04	261.45 ± 1.50	13.8

Table 6.10: Predicted and observed Drell-Yan cross-sections for lepton pairings with at least one of the categories listed.

in Table 6.9. Stacked kinematic plots for the region appear in Figures 6.1 and 6.2. Stacked plots compare the contribution of the various backgrounds to data. The different background contributions are stacked on top of each other to produce the total background expectation. For example, in the DY stacked plots appearing in Figures 6.1 and 6.2, the yellow contribution representing DY-ee is stacked on top of the grey contribution representing DY-$\mu\mu$.

To evaluate the DY cross-sections, we use the formula

$$\sigma_{data} = \frac{N_{observed}}{\mathcal{L} \times \epsilon} = \frac{N_{observed}}{N_{expected}} \times \sigma_{theory}, \tag{6.6}$$

where $\mathcal{L}$ is the sample's luminosity, ϵ is an efficiency for lepton selection, and $N_{observed}$ is the number of observed events. Additionally, $N_{expected}$ is the number of events expected and is given by the formula $\mathcal{L} \times \epsilon \times \sigma_{theory}$. The cross-section used in the MC sample is then given by σ_{theory} here as 251.3 pb.

We evaluated the cross-sections for each possible lepton type combination. We included the predicted and observed Drell-Yan cross-sections for lepton pairings with at least one of the lepton categories in Table 6.10. The uncertainties listed in the table only include statistical errors and not systematics.

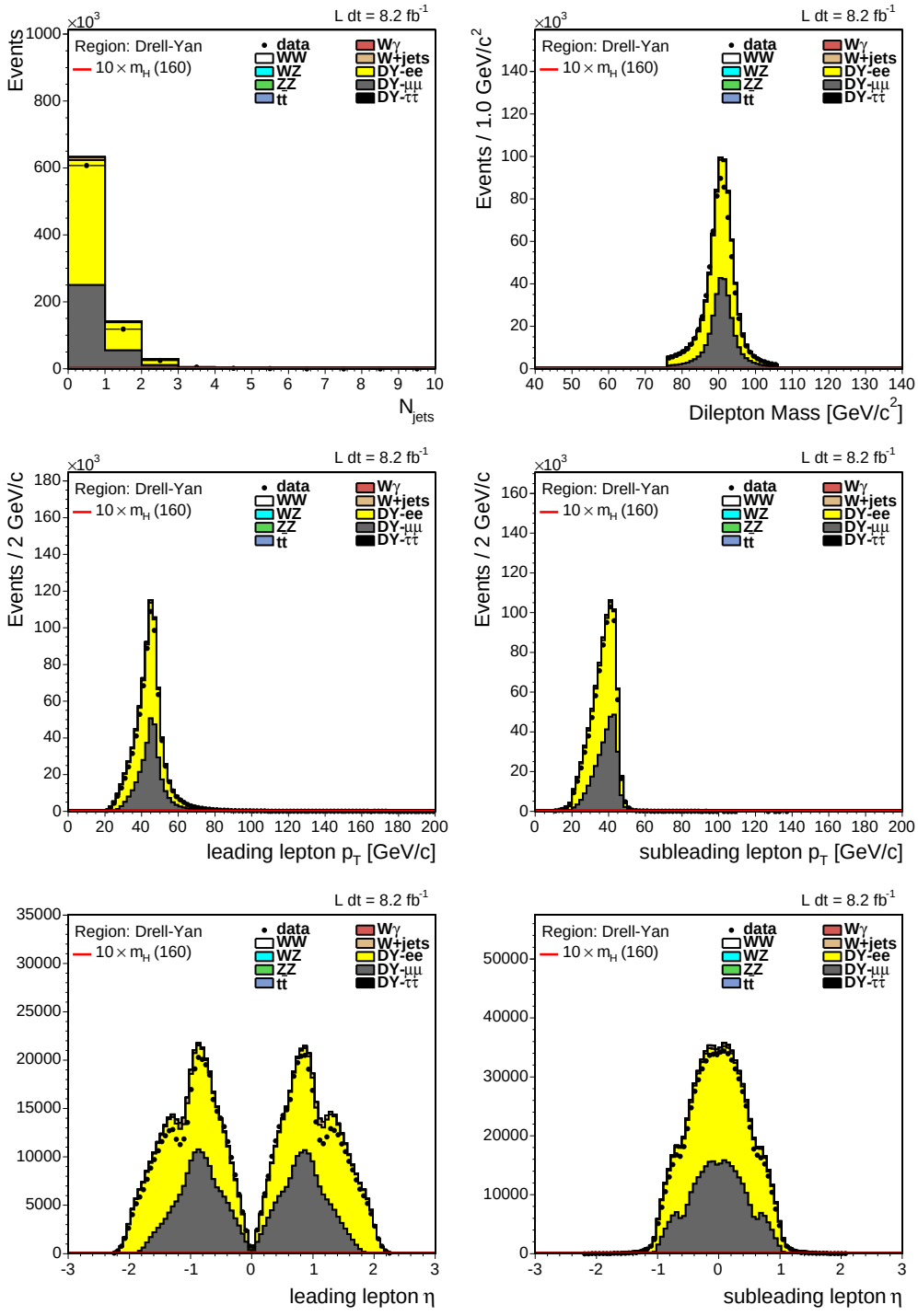

Figure 6.1: Drell-Yan ($Z \to l^+l^-$) control region.

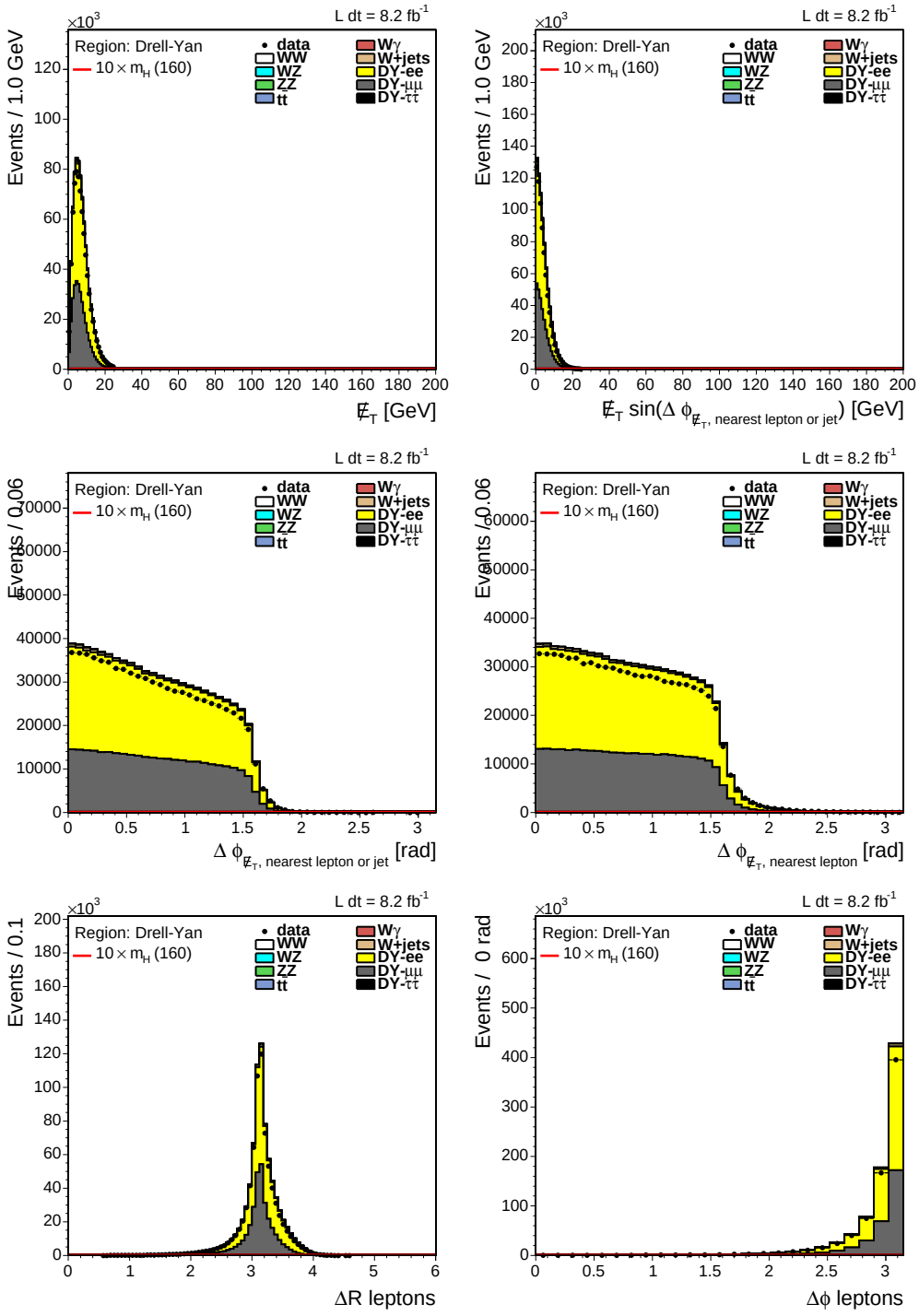

Figure 6.2: Drell-Yan ($Z \to l^+l^-$) control region.

	Denominator central
Fiducial	Track in CES
E_{HAD}/E_{EM}	$< 0.125 + 0.00045 \times E$
CalIso	≤ 0.3
Conversion	No

	Denominator forward
Fiducial	Track in PES
$\|PES\ \eta\|$	> 1.2 and < 2.0
E_{HAD}/E_{EM}	< 0.125
CalIso	≤ 0.3
NSiHits	≥ 3
Track $\|z_0\|$	≤ 60 cm
PHX electron	No

Table 6.11: The criteria used to define denominator objects for electrons.

6.5 Fake rates and $W+$ jets background modeling

6.5.1 Fake rate measurement

In order to incorporate the data driven W+jets background, we must evaluate the probability of a jet faking a lepton (fake rate). To do this, we defined a loose set of lepton selection cuts called denominator objects or "fakeable objects". When run over a sample of jet data, the goal of the denominator object or "fakeable object" selection is to pick out jets that have the potential to fake a lepton under the right circumstances. For example, in the jet data we specifically look for electromagnetic showers having tracks fiducial to the CES or PES in order to construct the denominator object or "fakeable object" for an electron. For muons, the denominator objects or "fakeable objects" are contructed to be fiducial to the already described muon categories. Incorporating the denominator objects with the standard lepton selections, we can define the fake rate f_i for a lepton category i as:

$$f_i = \frac{N_i(\text{leptons passing ID}) - \sum_{j \in EWK} N_{ij}(\text{leptons passing ID})}{N_i(\text{denominator objects}) - \sum_{j \in EWK} N_{ij}(\text{denominator objects})}. \tag{6.7}$$

Here, N_i is the number of leptons identified passing either the standard lepton selection (leptons passing ID) or the criteria to become a denominator object. For N_{ij}, summed over $j \in EWK$, these correspond to the expected number that result from electroweak processes such as $Z \to ll$ and $W \to l\nu$.

The denominator object definitions for central and forward electrons are listed in Table 6.11. The denominator object definitions for central and forward muons are listed in Table 6.12.

The goal of evaluating the fake rate is to create a weight which can be applied to events having one identified lepton and one identified denominator object corresponding to the $W+$ jets background.

To evaluate the fake rate, we ran over data samples corresponding to four jet triggers to select identified leptons and denominator objects. The triggers used required jets with $E_T > 20$ GeV, 50 GeV, 70 GeV, 100 GeV. We then measured the fake rates as functions of the jet E_T and averaged together over the four triggers. The four trigger samples each have different contributions of quark and gluon jets. Averaging over

	Denominator central
NAxL (5 hits)	≥ 2
NStL (5 hits)	≥ 2
Track $\lvert z_0 \rvert$	≤ 60 cm
Track d_0	< 0.02 cm with > 0 NSiHits or < 0.2 cm with 0 NSiHits
Track $\chi^2/n.d.f.$	< 4 for run number > 186598, < 3 for others
CalIso	≤ 0.3
Fiducial	Not in PES

	Denominator forward
COT hit fraction	> 0.6
Track $\lvert z_0 \rvert$	≤ 60 cm
Track d_0	< 0.02 cm with > 0 NSiHits or < 0.2 cm with 0 NSiHits
Track $\chi^2/n.d.f.$	< 4 for run number > 186598, < 3 for others
CalIso	≤ 0.3
Fiducial	Not in PES

Table 6.12: The criteria used to define denominator objects for muons.

the four samples provided us with a better model for quark and gluon jets.

The fake rates measured for electrons appear in Figure 6.3, for central muons in Figure 6.4, and for forward muons in Figure 6.5. In the figures, the dark grey area corresponds to statistical errors resulting from the averaging of the measured rates. We applied a systematic uncertainty based on the scatter of the values measured among the jet samples. We did this by taking the combined systematic and statistical error as being $\sqrt{\sigma_{stat}^2 + \alpha^2}$ where α quantifies the systematic error and is scaled until each jet sample's measurement is consistent with being 1σ off of the mean.

The CMIOCESni category does demonstrate a negative fake rate in the higher jet p_T bins as seen in Figure 6.4. For simplification, we do not verify the MC for the electroweak backgrounds used in the subtraction as meticulously as those used for backgrounds in the final limit setting of the analysis. In the instance of CMIOCESni, muons previously categorized as CMIOCESni were picked up as CMUni and CMUPni muons. The fake rate for CMIOCESni is small and the effect of the application of the negative fake rate is small compared to the large 40% uncertainty applied to the normalization of the QCD background.

6.5.2 $W+$ jets background modeling

To construct the $W+$ jets background samples used in the analysis, we took a sample of events with one identified lepton and one identified denominator object. We filtered the denominator object through the analysis cuts just as if it were a normal lepton. We took only the denominator object with the highest E_T. It is possible for a denominator object to fake more than one lepton type. We included these separately. Once composed, we weighted the events with their corresponding fake rate as described above to the sample.

There are a sample of $W+$ jets events that will not make it into the $W+$ jets background model. These are events when the identified lepton is not a triggerable category such as CrkTrk. To correct for the absence

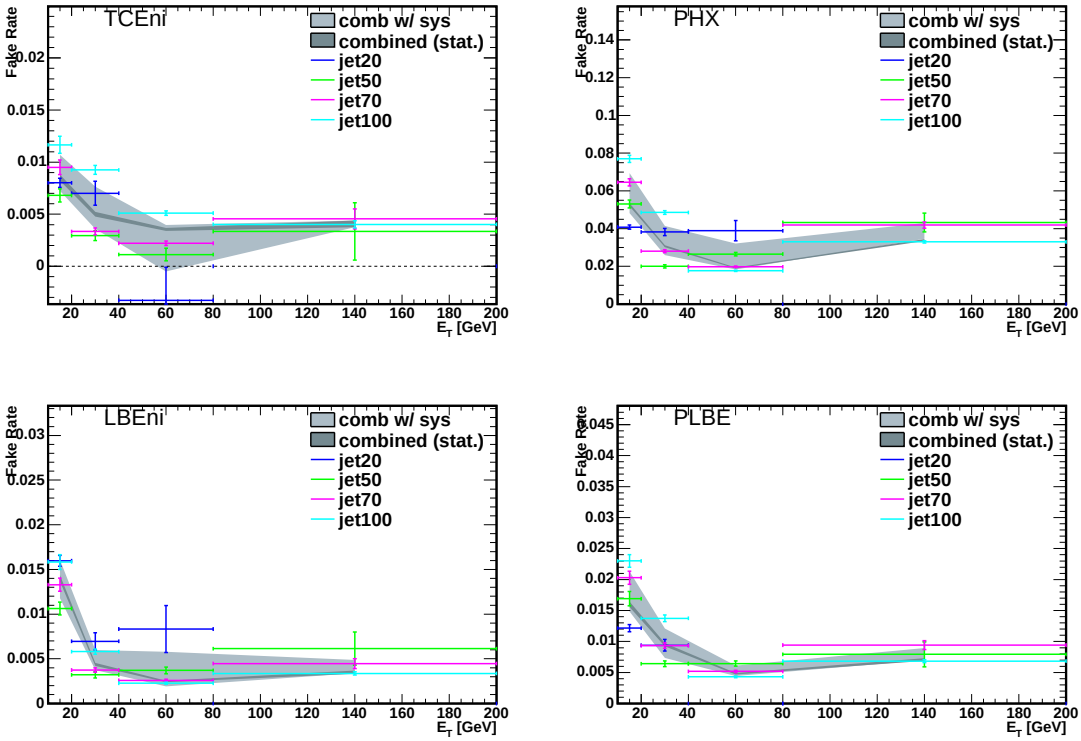

Figure 6.3: Fake rates for electrons.

of these events, we measured a non-triggerable fake rate using a MC sample of $W \to l\nu$. In the $W \to l\nu$ MC, we again looked for a real lepton and a denominator object. We then constructed a ratio of the number of events where the l from $W \to lv$ is not triggerable to the number of events where the l is triggerable. This then makes the total number of events in the $W+$ jets backgound

$$N^{data}_{total} = N^{data}_{triggerable} + N^{data}_{triggerable} \times \frac{N^{MC}_{nontriggerable}}{N^{MC}_{triggerable}}. \tag{6.8}$$

6.6 Control regions

6.6.1 $W+$ jets and $W+\gamma$ control region

To check that the $W+$ jets and $W+\gamma$ backgrounds are modeled accurately, we defined a control region comprised primarily of the $W+$ jets and $W+\gamma$ contributions. The events that make it into this sample follow the normal analysis cuts with the exception that we require same-charge lepton candidates. The number of expected and observed events appear in Table 6.13. Kinematic plots for the region appear in Figures 6.6 and 6.7.

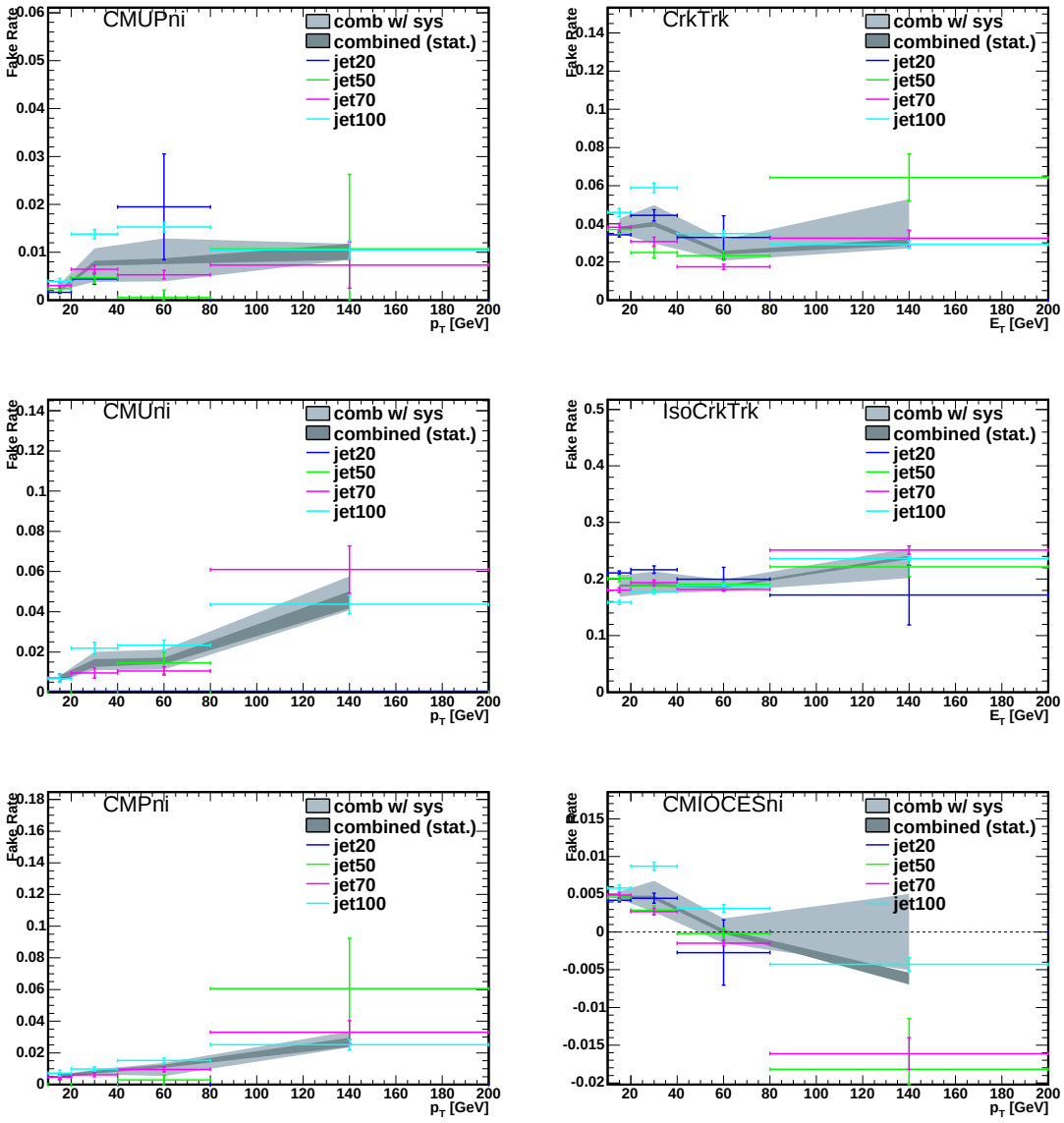

Figure 6.4: Fake rates for central muons.

Category	WW	WZ	ZZ	$t\bar{t}$	DY	$W\gamma$	W+jets	Total	Data
e e	14.4	9.1	2.4	6.5	29.3	118.2	131.0	310.8	346.0
e μ	15.7	15.0	1.2	6.8	93.1	97.6	158.4	387.8	363.0
μ μ	0.0	4.8	0.5	0.0	0.4	0.0	13.5	19.2	22.0
e trk	5.2	4.7	0.6	2.1	8.0	23.7	140.0	184.4	187.0
μ trk	0.0	2.6	0.2	0.0	2.1	3.5	61.2	69.6	52.0
Total:	35.3	36.2	4.9	15.5	132.9	242.9	504.1	971.9	970.0

Table 6.13: Predicted and observed yields in the W+ jets and $W + \gamma$ control region.

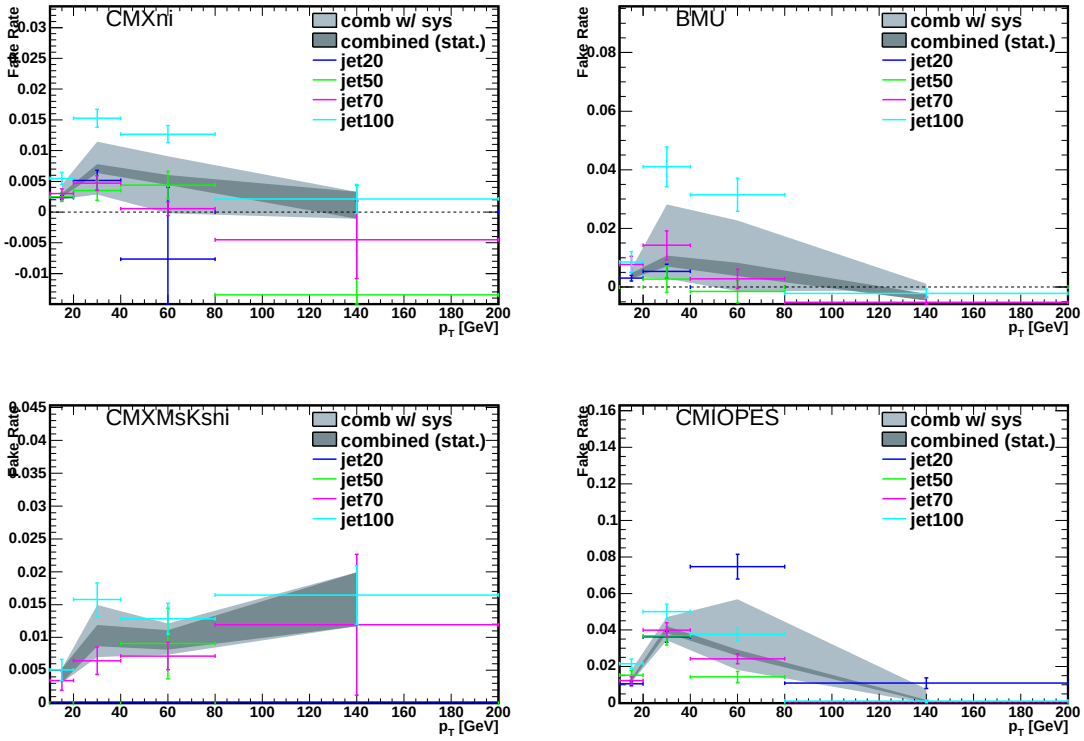

Figure 6.5: Fake rates for forward muons.

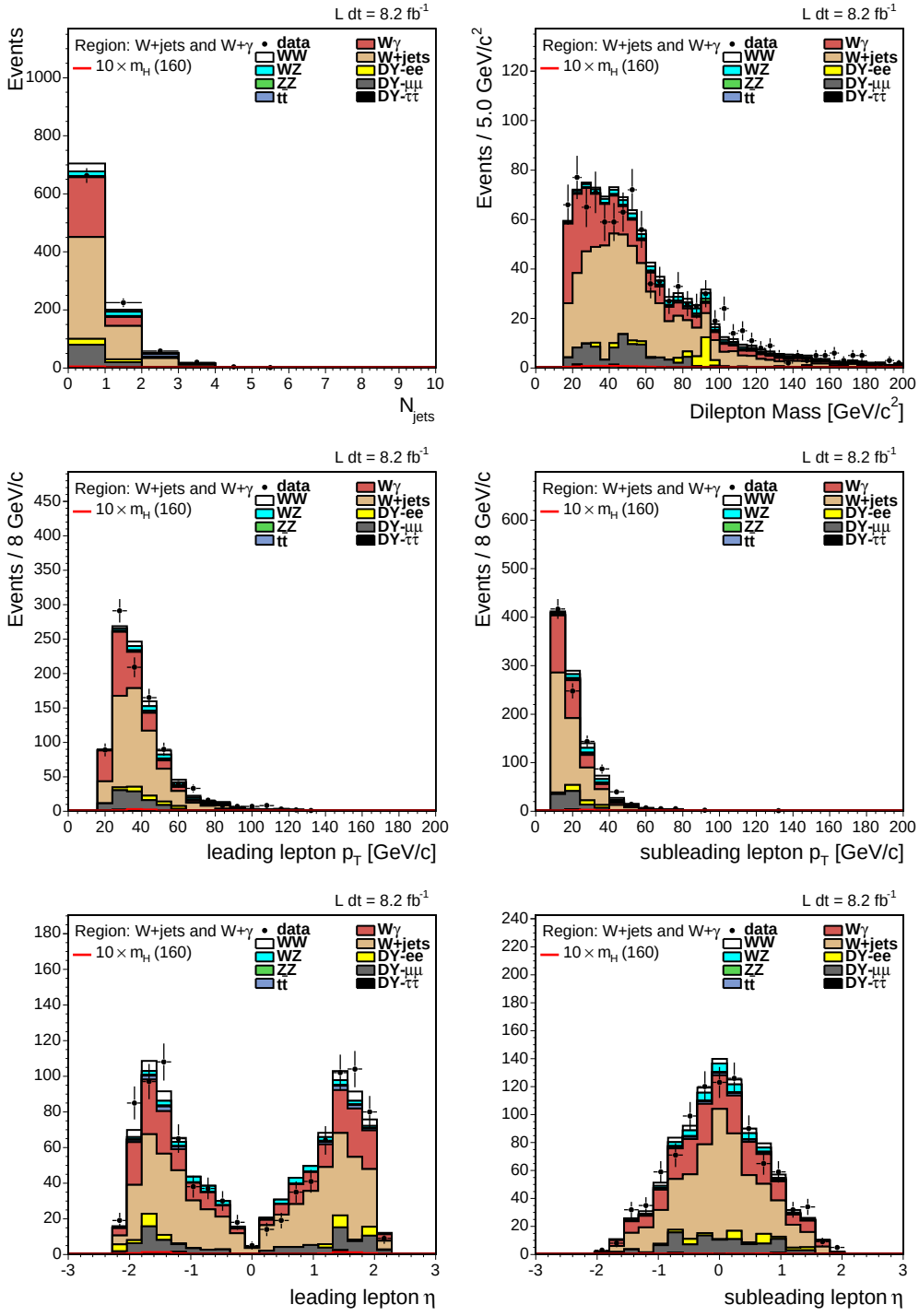

Figure 6.6: The $W+$ jets and $W+\gamma$ control region.

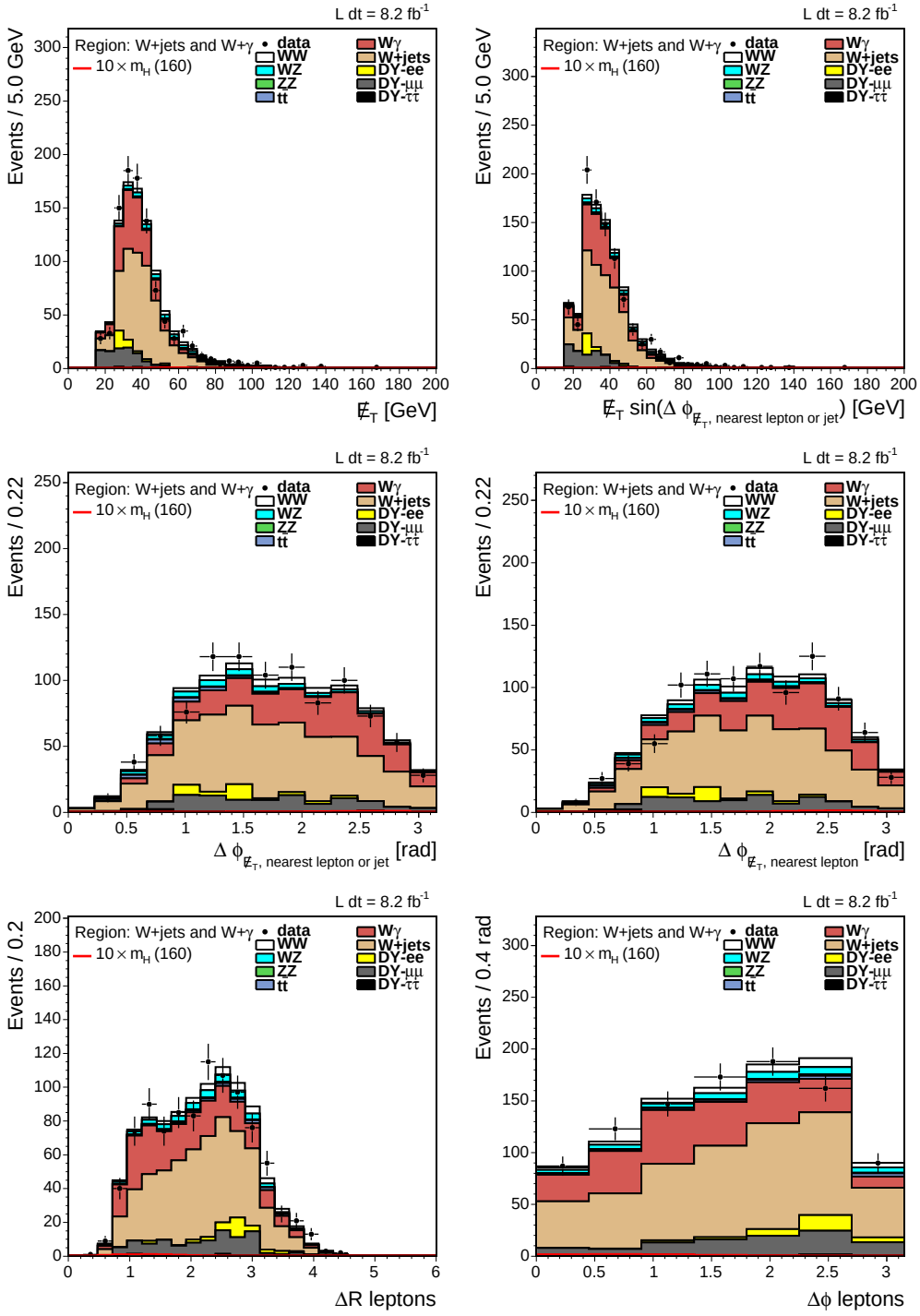

Figure 6.7: The $W+$ jets and $W+\gamma$ control region.

Category	WW	WZ	ZZ	$t\bar{t}$	DY	$W\gamma$	W+jets	Total	Data
e e	0.1	0.2	0.0	0.0	1.5	74.3	9.1	85.2	114.0
e μ	0.1	0.4	0.0	0.0	5.7	44.7	6.4	57.3	61.0
μ μ	0.0	0.2	0.0	0.0	0.0	0.0	0.9	1.2	3.0
e trk	0.0	0.1	0.0	0.0	0.9	10.9	16.3	28.1	18.0
μ trk	0.0	0.0	0.0	0.0	0.2	2.8	8.2	11.2	5.0
Total:	0.2	0.8	0.1	0.0	8.4	132.7	40.9	183.0	201.0

Table 6.14: Predicted and observed yields in the additional $W + \gamma$ control region.

6.6.2 Additional $W + \gamma$ control region

To examine the $W+\gamma$ control region, we applied the normal analysis cuts with the exception of reversing the cut on the dilepton mass (taking $M_{ll} > 16$ GeV/c^2 to $M_{ll} < 16$ GeV/c^2) and requiring the charged leptons to now have the same charge instead of opposite. The number of expected and observed events appear in Table 6.14. Kinematic plots for the region appear in Figures 6.8 and 6.9.

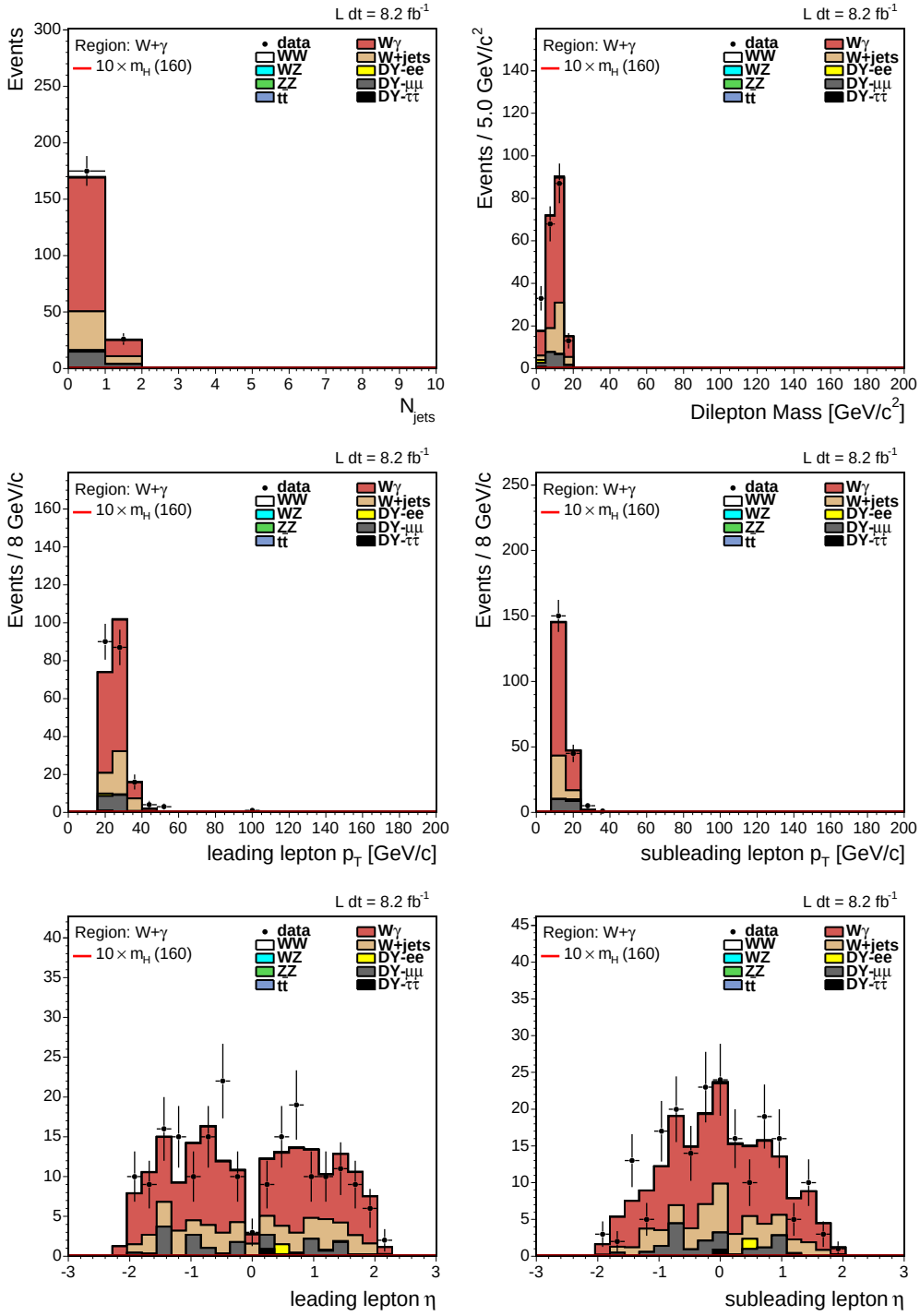

Figure 6.8: The additional $W + \gamma$ control region.

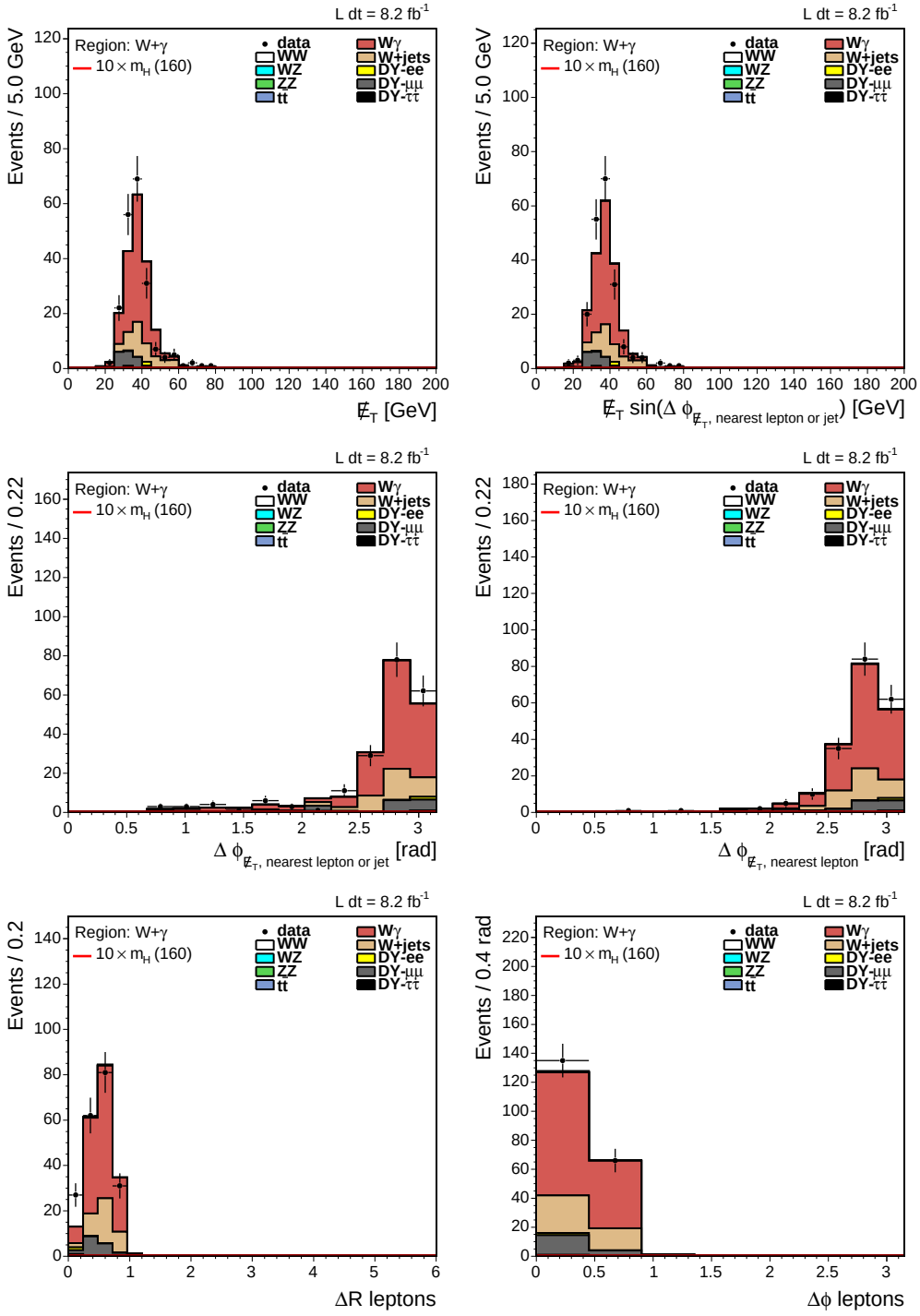

Figure 6.9: The additional $W + \gamma$ control region.

Chapter 7

Analysis of events with no jet activity

This analysis incorporated events with 0, one, and two or more jets. The background and signal samples vary widely based on the number of jets in the event. For example, in events with 0 jets, the WW background is dominant. In events with 2 or more jets, the $t\bar{t}$ is by far the dominant background. In addition to the differing backgrounds, the signal contributions change was well. In events with 0 jets, gluon fusions dominates while associated production dominates in events with jets.

In order to capitalize on the varying background contributions based on the number of jets, we divided the events into bins consisting of 0, one, and two or more jets. This allowed us to cater the analysis to counter the dominate background inherent to the specific jet bin. This chapter will describe events without jets.

Several lepton types have a large contamination from jets faking leptons. We further divide the data sample up into two categories based on the rate at which jets fake leptons, either low S/B (high fake rate) or high S/B (low fake rate). We grouped all dilepton pairings having either a forward electron (PHX or PLBE) or an IsoCrkTrk in the low S/B grouping. We also include muon categories that have also have a high fake rate such as CMPni, CMUni, and CMIOPES.

We isolate the events in the high S/B sample to prevent dilution in sensitivity from events that appear in the low S/B sample. Despite the low S/B having little sensitivity compared to the high S/B sample, we are not penalized by incorporating it into the analysis, even if it contributes only a few percent in sensitivity.

The expected signal and background contributions compared to data appear in Tables 7.1 and 7.2 for high and low S/B and assuming a Higgs mass of 165 GeV/c^2. In Table 7.3, the combination of high and low S/B appears.

7.1 Matrix Element calculation

The Matrix Element (ME) technique allowed us to determine a probability, based on kinematics, that an event is consistent with the expectation of being either signal or background. We based this probability on a

CDF Run II Preliminary	$\int \mathcal{L} = 8.2$ fb^{-1}		
$M_H = 165$ GeV/c^2			
$t\bar{t}$	2.48	$\pm$	0.76
DY	198	$\pm$	54
WW	573	$\pm$	57
WZ	24.6	$\pm$	3.7
ZZ	36.0	$\pm$	5.1
W+jets	112	$\pm$	27
$W\gamma$	56.4	$\pm$	8.2
Total Background	1000	$\pm$	100
$gg \to H$	18.3	$\pm$	5.4
WH	0.452	$\pm$	0.076
ZH	0.472	$\pm$	0.067
VBF	0.164	$\pm$	0.034
Total Signal	19.3	$\pm$	5.5
Data	957		

HighSB-0J

Table 7.1: The expected signal and background contributions compared with data for the high S/B grouping for events having no jets.

CDF Run II Preliminary	$\int \mathcal{L} = 8.2$ fb^{-1}		
$M_H = 165$ GeV/c^2			
$t\bar{t}$	0.84	$\pm$	0.26
DY	185	$\pm$	50
WW	250	$\pm$	25
WZ	13.3	$\pm$	2.0
ZZ	18.2	$\pm$	2.6
W+jets	377	$\pm$	57
$W\gamma$	150	$\pm$	22
Total Background	994	$\pm$	93
$gg \to H$	6.4	$\pm$	1.9
WH	0.161	$\pm$	0.027
ZH	0.128	$\pm$	0.018
VBF	0.052	$\pm$	0.011
Total Signal	6.7	$\pm$	1.9
Data	1187		

LowSB-0J

Table 7.2: The expected signal and background contributions compared with data for the low S/B grouping for events having no jets.

CDF Run II Preliminary	$\int \mathcal{L} = 8.2$ fb^{-1}		
$M_H = 165$ GeV/c^2			
$t\bar{t}$	3.3	$\pm$	1.0
DY	380	$\pm$	100
WW	823	$\pm$	82
WZ	37.9	$\pm$	5.7
ZZ	54.2	$\pm$	7.7
W+jets	489	$\pm$	83
$W\gamma$	206	$\pm$	30
Total Background	2000	$\pm$	190
$gg \to H$	24.6	$\pm$	7.3
WH	0.61	$\pm$	0.10
ZH	0.599	$\pm$	0.085
VBF	0.215	$\pm$	0.044
Total Signal	26.1	$\pm$	7.4
Data	2144		

All

Table 7.3: The expected signal and background contributions compared with data for the combination of the high and low S/B groupings for events having no jets.

leading-order matrix element calculation. The technique accounts for effects such as acceptances, efficiencies, and detector resolution. Once calculated, we used the outputted probability values as one of many inputs into a neural network which we used to further discriminate signal from background. The neural network will be described in the next section.

The ability to evaluate the probability depends on quantities the CDF detector is capable of measuring. We made use of eight kinematic quantities to perform the calculation: momentum for the charged leptons and missing transverse energy, $\not\!\!E_{Tx}$ and $\not\!\!E_{Ty}$. With these observables, the event probability for a given contribution m, is given by

$$P_m(x_{obs}) = \frac{1}{\langle \sigma_m \rangle} \int \frac{d\sigma_m^{th}(y)}{dy} \epsilon(y) G(x_{obs}, y) dy, \tag{7.1}$$

where $d\sigma_m^{th}/dy$ is the leading-order differential cross-section for contribution m; x_{obs} are the observable variables (charged lepton momenta and $\vec{\not\!\!E}_T$); y are the true lepton four-momenta (for electrons, muons, and neutrinos); $\epsilon(y)$ is the product of efficiencies and acceptances; and $G(x_{obs}, y)$ is the transfer function handling the effects of detector resolution. We evaluate the normalization, $\langle \sigma_m \rangle$, by using the requirement that

$$\int P_m(x_{obs}) dx_{obs} = 1. \tag{7.2}$$

We used WW, WZ, $W + \gamma$, $W+$ jets, and $H \to WW$ for the contribution m. We evaluated the efficiency $\epsilon(y)$ by using a combination of MC and data for $W + \gamma$ and $W+$ jets. For all other contributions, we used

a GEANT based MC to determine the efficiency as described previously.

We evaluated the leading-order differential cross-sections, $d\sigma_m^{th}/dy$, at parton level using the MCFM program [31]. With the presence of two neutrinos in the final state, we have missing information in $d\sigma_m^{th}/dy$ that must be taken into account. We did this by integrating over the possible neutrino momenta given the constraints provided by $\not\!\!E_{T_x}$ and $\not\!\!E_{T_y}$. Additionally, the ME incorporates information concerning the W and Z resonances. This implicitly incorporates constraints on the W and Z masses into the calculation. For the signal contribution P_{HWW}, we evaluated the probability for all 19 Higgs mass hypotheses for each event.

In order to construct a discriminant to be used as a neural network input, we defined a likelihood ratio (LR) as:

$$LR_S(x_{obs}) = \frac{P_s(x_{obs})}{P_s(x_{obs}) + \Sigma_i k_i P_i(x_{obs})}, \tag{7.3}$$

where S is either direct WW production or $H \rightarrow WW$ and k_i is the expected fractional contribution for the i-th background (constraining $\Sigma_i k_i = 1$).

Figure 7.1 shows the output of the likelihood ratio calculation assuming a Higgs mass of 160 GeV/c^2 for using either $H \rightarrow WW$ or WW as the signal contribution. Figure 7.2 shows the output of the likelihood ratio for the high and low cases for S/B. As visible in Figures 7.1 and 7.2, The $H \rightarrow WW$ signal demonstrates a peak in the lowest likelihood ratio bin. This results from components of the $H \rightarrow WW$ sample looking more kinematically similar to the WW background than to the $H \rightarrow WW$ signal.

The ME technique is very powerful for signal discrimination since all processes included are very well modeled and understood. In events with jets however, the technique is significantly less useful since jets are not predicted at leading-order and QCD uncertainties are large.

7.2 Neural Network

We employed a neural network (NN) to further increase our sensitivity to the Higgs signal. A NN is effectively a function which maps several inputs to a single output (score), in this case between -1 and 1. For inputs, we selected kinematic variables from the events. We then fit the distribution of NN scores to perform the final limit setting.

To cross-check the improvement we see by using a NN, we recently bypassed the NN and performed the full analysis using a set of analysis cuts to optimize Higgs signal using $S/\sqrt{S+B}$. Through the comparison of a cut-based version of the analysis to the NN analysis, we estimated that the use of the NN multivariate technique increases our sensitivity by 10-20%.

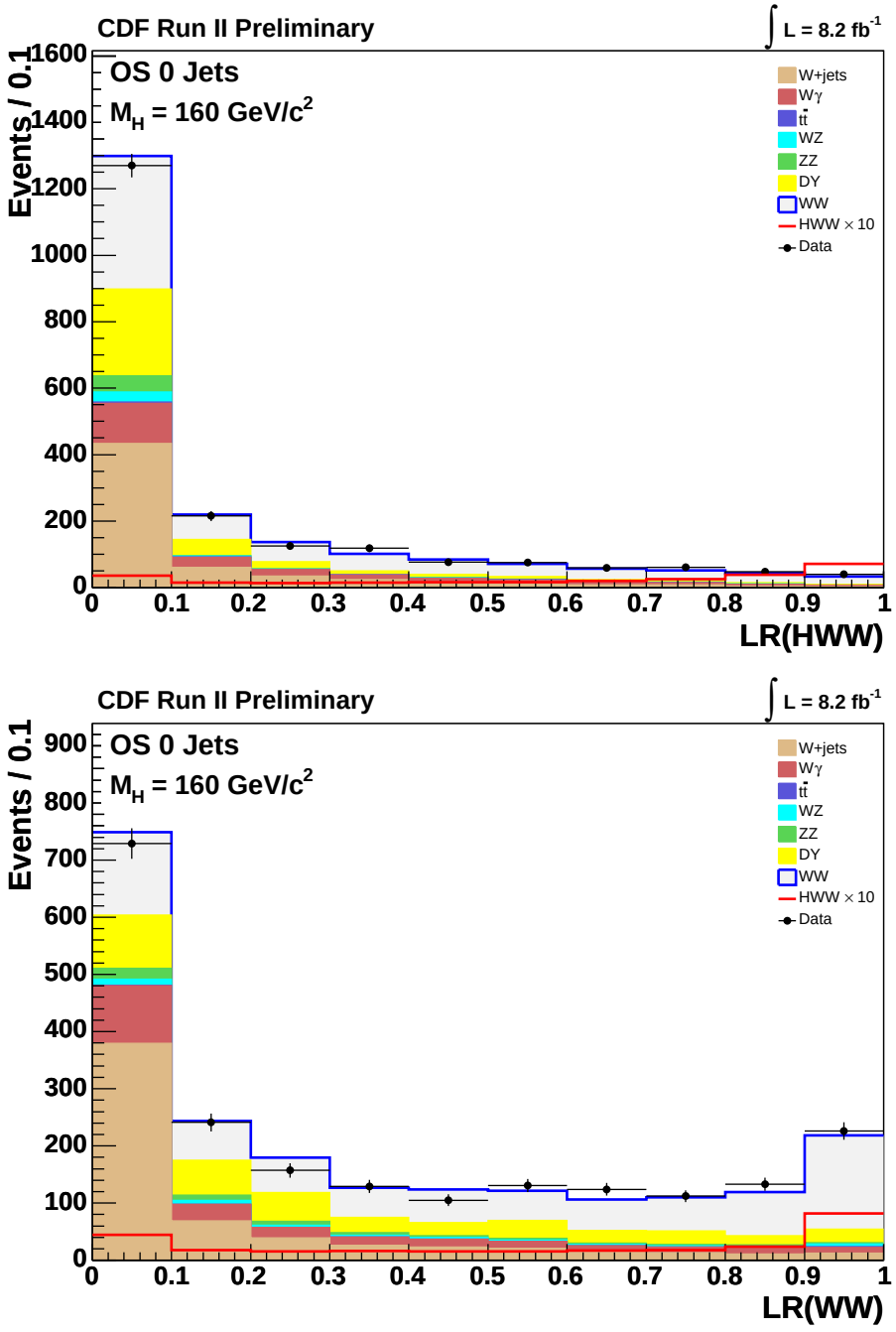

Figure 7.1: Output of the LR calculation assuming a Higgs mass of 160 GeV/c^2 for the assumption of either $H \rightarrow WW$ (top) or WW (bottom) as the signal contribution.

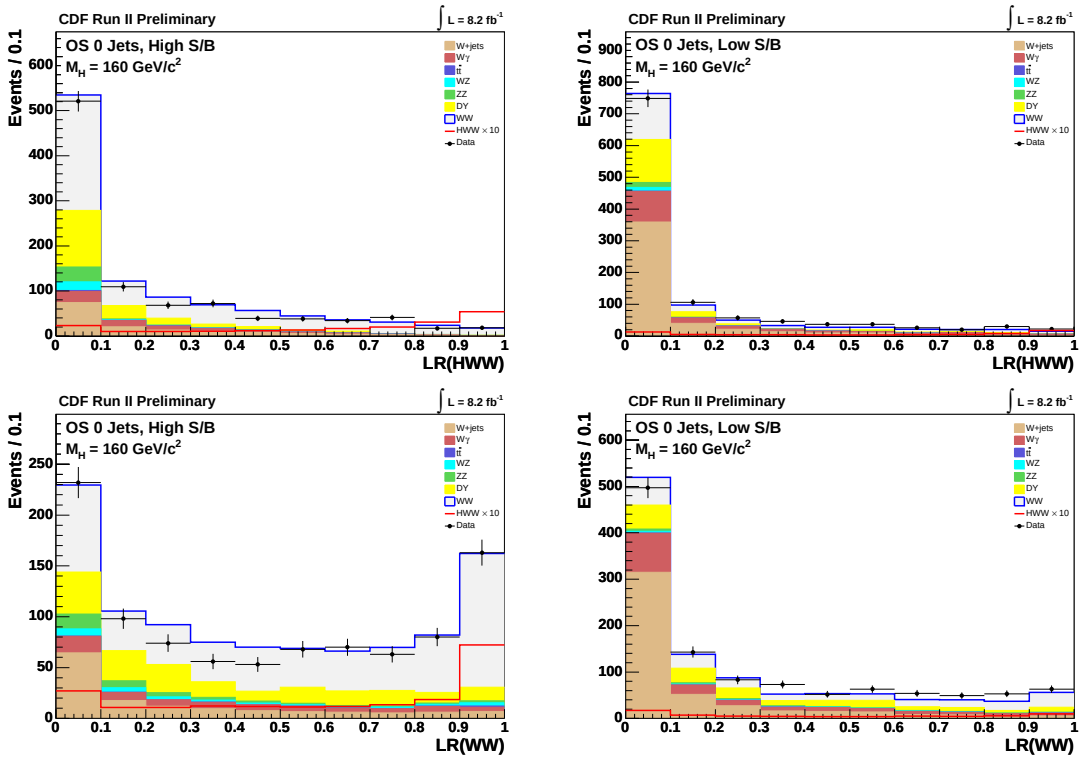

Figure 7.2: Divided into high and low S/B, the output of the LR calculation, assuming a Higgs mass of 160 GeV/c^2 for the assumption of either $H \rightarrow WW$ (top) or WW (bottom) as the signal contribution.

7.2.1 Neural network introduction

Artificial NNs model a biological network of neurons seen in nature [32]. The artificial neurons are fairly simple, being activated when a weighted sum of inputs becomes larger than a threshold. For a neuron i, the activation function z_i is simply

$$z_i = \sum_j w_{ij} x_j - s_i \tag{7.4}$$

for inputs x_j, weights w_{ij}, and threshold s_i. Once activated, the neuron calculates an output, via a transfer function, to be relayed to other neurons. The transfer function can be a simple, differentiable, smoothed version of the step function such as:

$$\sigma(z_i) = \frac{2}{1 + e^{-z_i}} - 1. \tag{7.5}$$

We employed a feed-forward neural network in which the neurons form a layered structure consisting of an input layer, a hidden layer, and an output layer. In this NN variant, the signal always gets conveyed to the next layer. Figure 7.3 shows a simple diagram of a feed-forward neural network.

In order to be used, the NN must undergo training, which is a procedure that adjusts the NN's weights to optimally distinguish signal from background. We ideally want more signal like events to have a high score

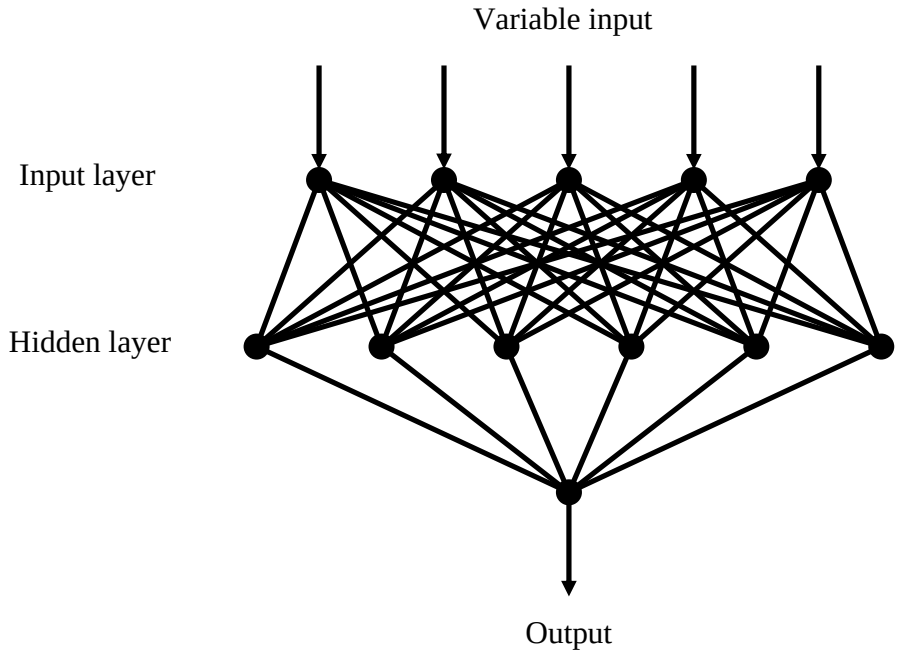

Figure 7.3: A diagram of a feed-forward NN.

(near 1), while more background like events receive a lower score (near -1). We performed the training by adjusting the weights to minimize an error function defined as the squared distance between outputs the NN nodes produce against values expected for the input type (signal or background). We performed the minimization itself through a gradient descent method.

We made use of the backpropagation algorithm to perform the error function minimization to train the NN. It is a recursive algorithm that begins with the output and climbs the network to the input, performing the error function minimization along the way.

7.2.2 Neural network application

In our application of NNs, we make ude of the NN software package *Neurobayes*® [33]. The kinematic variables we select as inputs are:

- H_T: The sum of the lepton p_T and event $\not{E}_T$
- $LW(HWW)$: The output of the ME likelihood ratio for a signal of $H \rightarrow WW$
- $LW(WW)$: The output of the ME likelihood ratio for a signal of WW
- $\Delta\phi(ll)$: The difference in ϕ between the two leptons

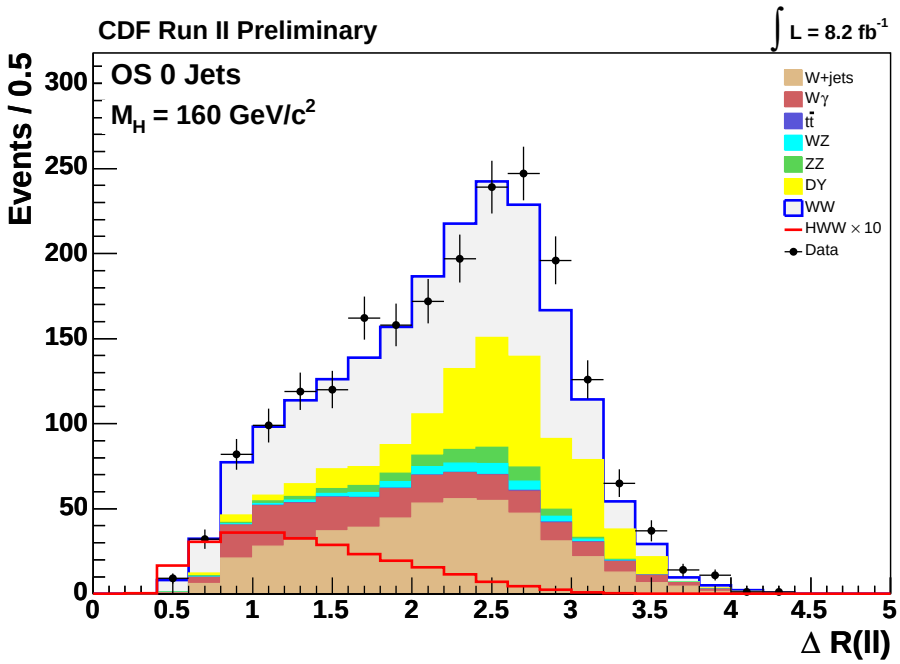

Figure 7.4: The ΔR_{ll} input to the NN for a Higgs mass of 160 GeV/c^2.

- $\Delta R(ll)$: The ΔR between the two leptons
- $M(ll)$: The combined mass of the leptons
- $p_T(l_1)$: The transverse momentum of the leading lepton
- $p_T(l_2)$: The transverse momentum of the subleading lepton
- $M_T(ll\not{E}_T)$: The transverse mass of the two leptons and $\not{E}_T$

We chose the kinematic variables above to maximize Higgs signal sensitivity. With the exception of the likelihood ratios, the neural network inputs appear in Figures 7.4 and 7.5.

We trained the neural network over 19 Higgs masses, ranging from 110 to 200 GeV/c^2, one every increment of 5 GeV/c^2. Additionally, the background samples described in the last chapter were included in training as well. We weighted the training background samples based on their expected contribution to the data sample. To check the process, we randomly divided the each sample into two groups. We used one group for training while the other was used as a check against the NN being sensitive to statistical fluctuations.

The NN output distributions, high and low S/B, for a Higgs mass of 165 GeV/c^2 appear in Figure 7.6. The NN output for the other Higgs masses appear in Figures 7.7-7.11. We can then use these NN output distributions to set the final Higgs production limits.

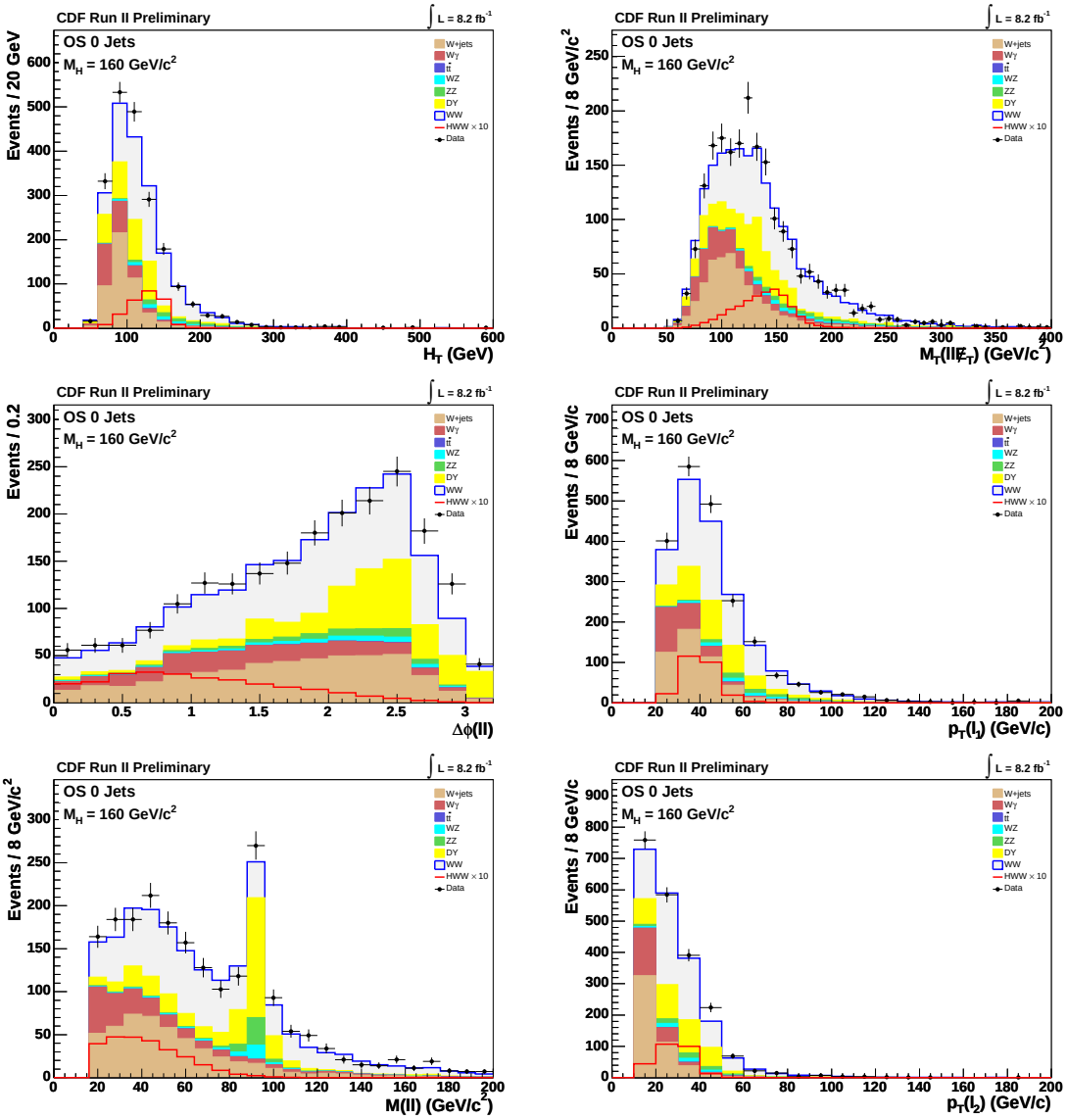

Figure 7.5: The other inputs to the NN for a Higgs mass of 160 GeV/c^2.

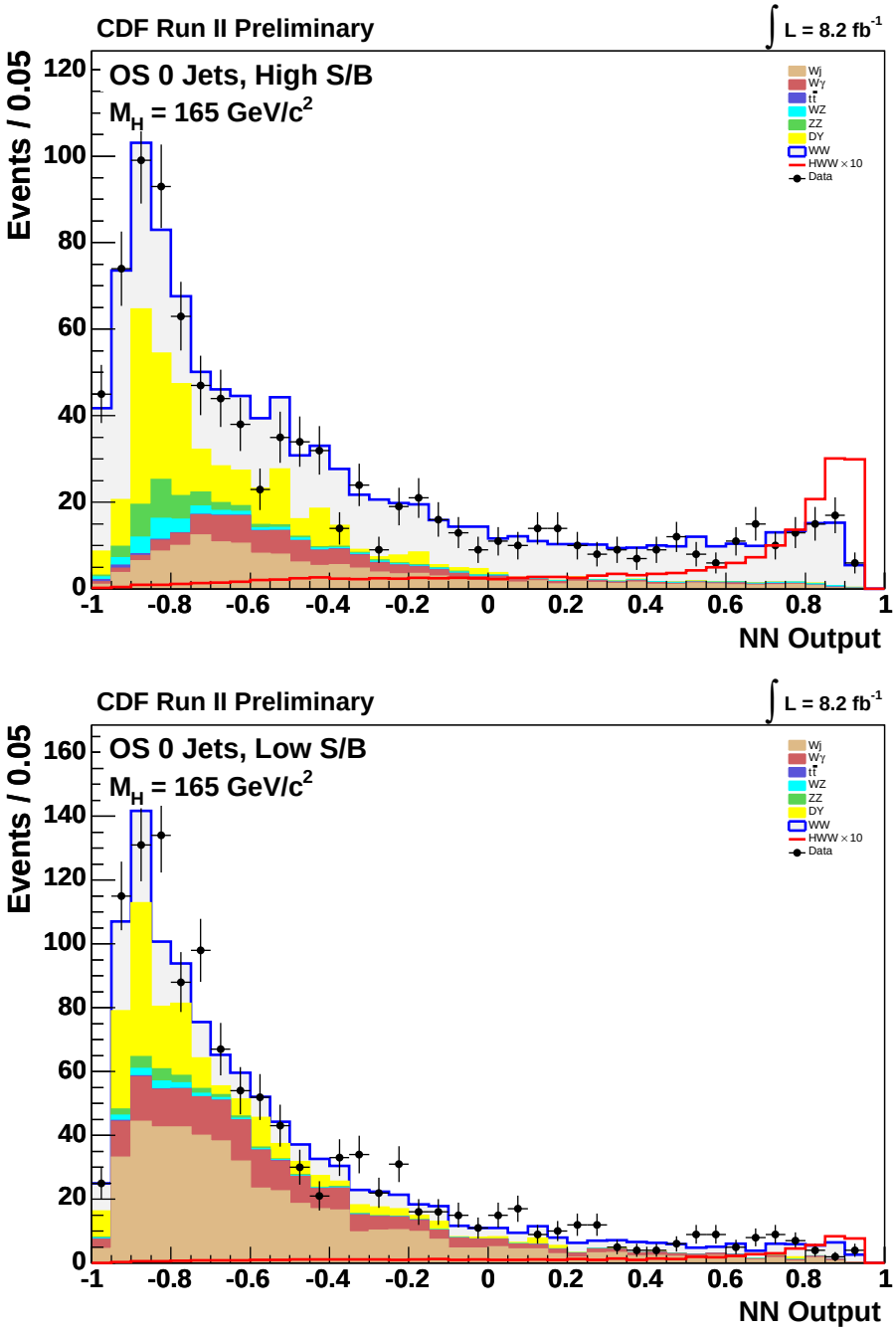

Figure 7.6: Output of the NN for a Higgs mass of 165 GeV/c^2.

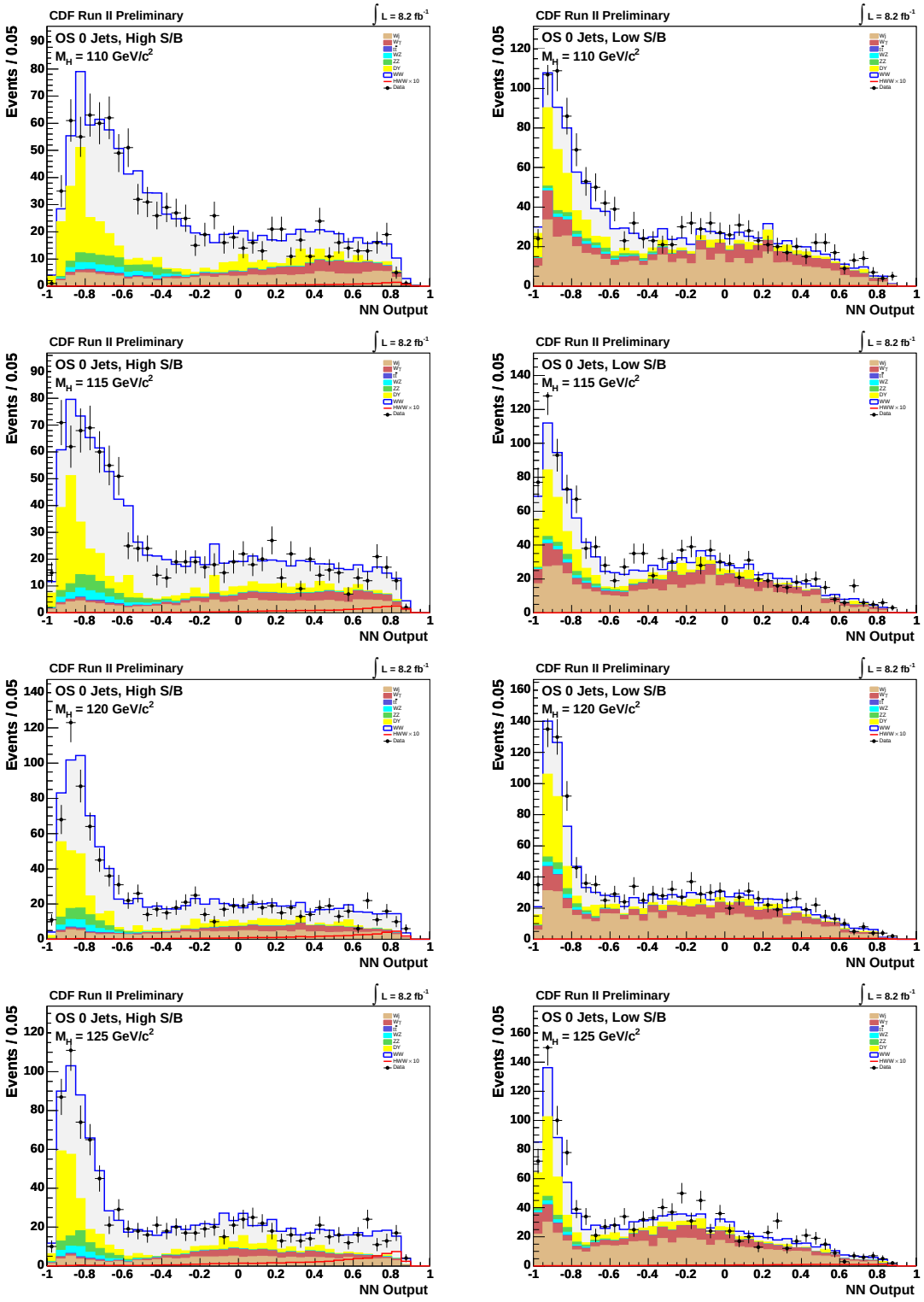

Figure 7.7: Output of the NN for Higgs masses of 110, 115, 120, and 125 GeV/c^2.

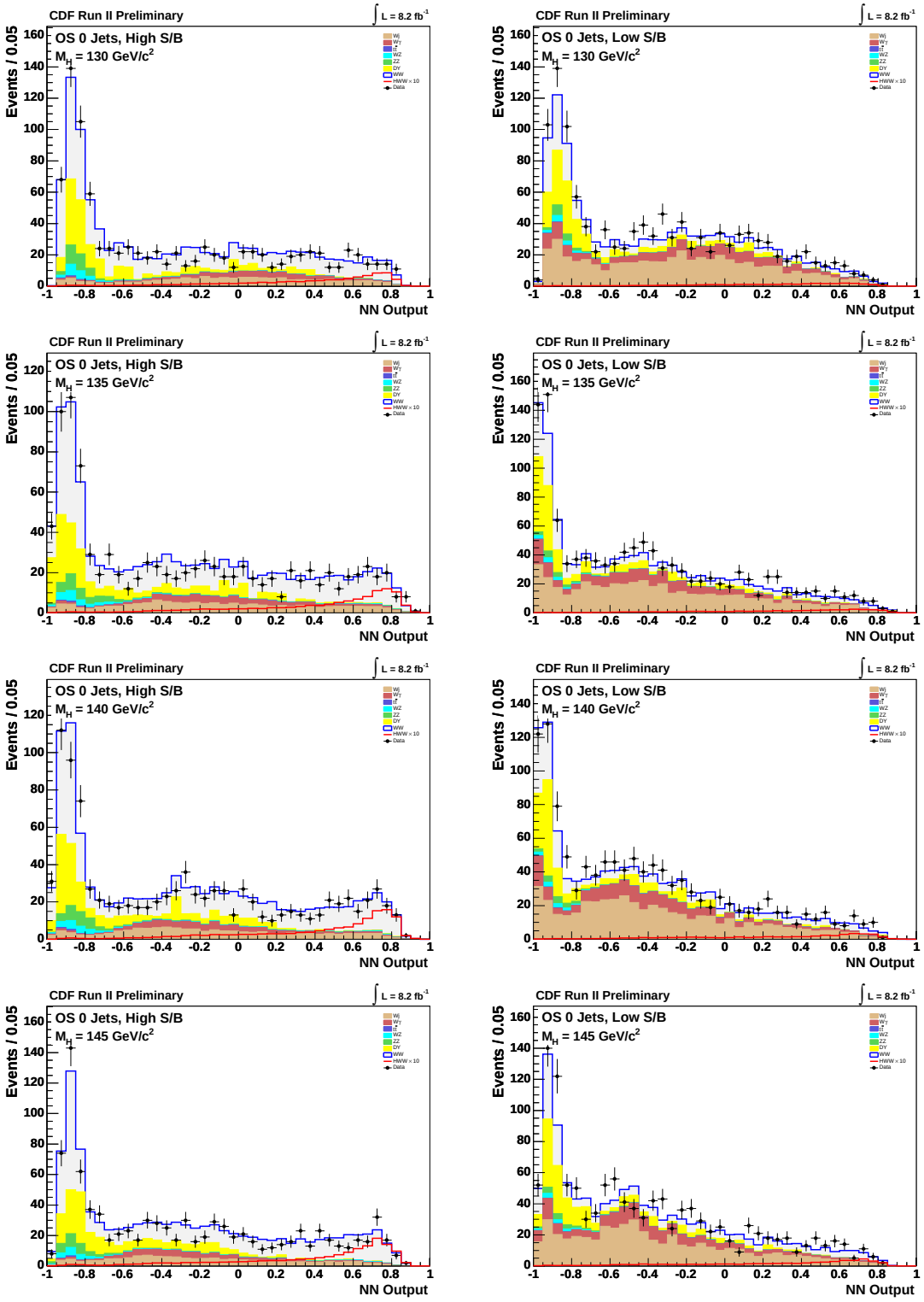

Figure 7.8: Output of the NN for Higgs masses of 130, 135, 140, and 145 GeV/c^2.

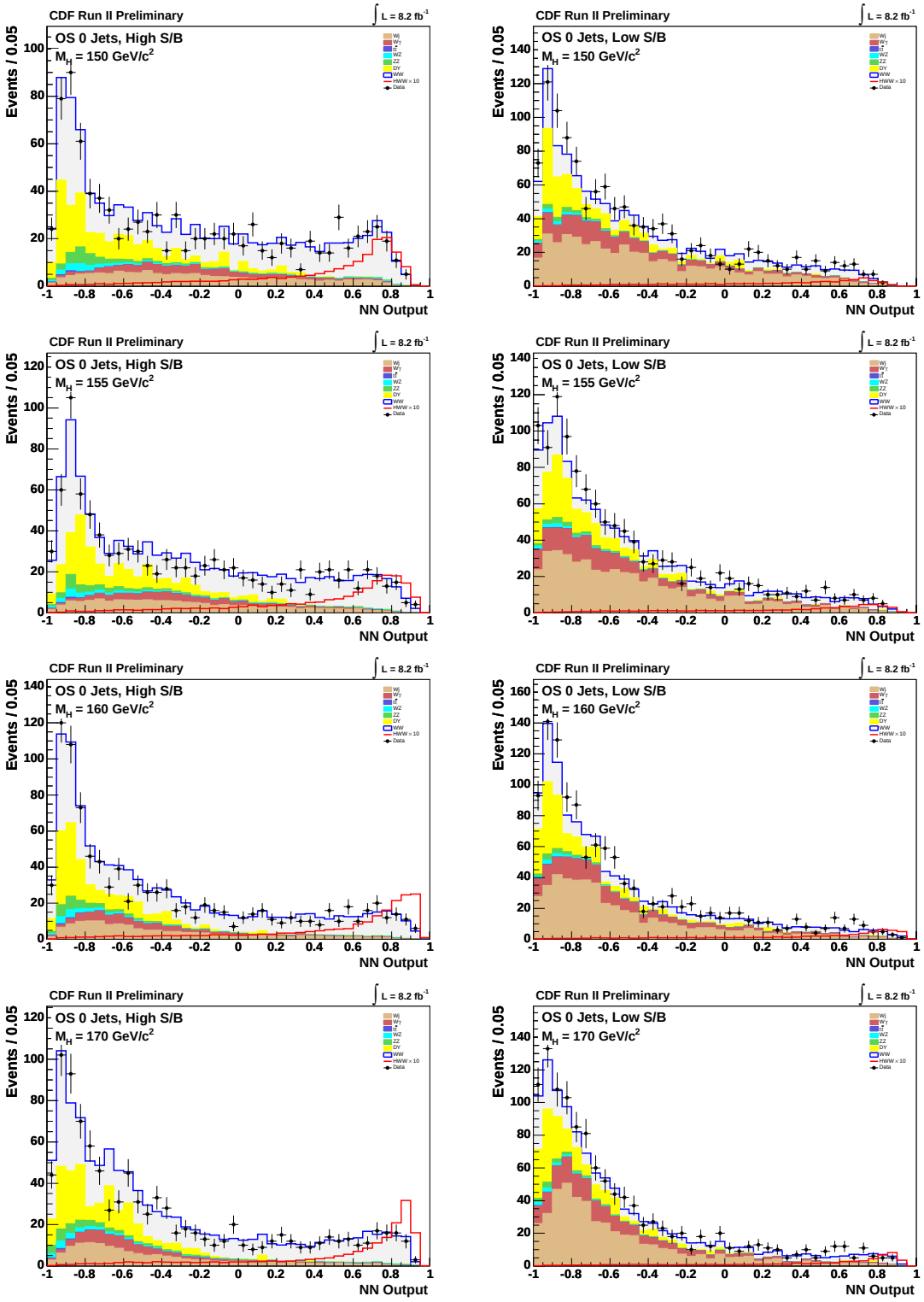

Figure 7.9: Output of the NN for Higgs masses of 150, 155, 160, and 170 GeV/c^2.

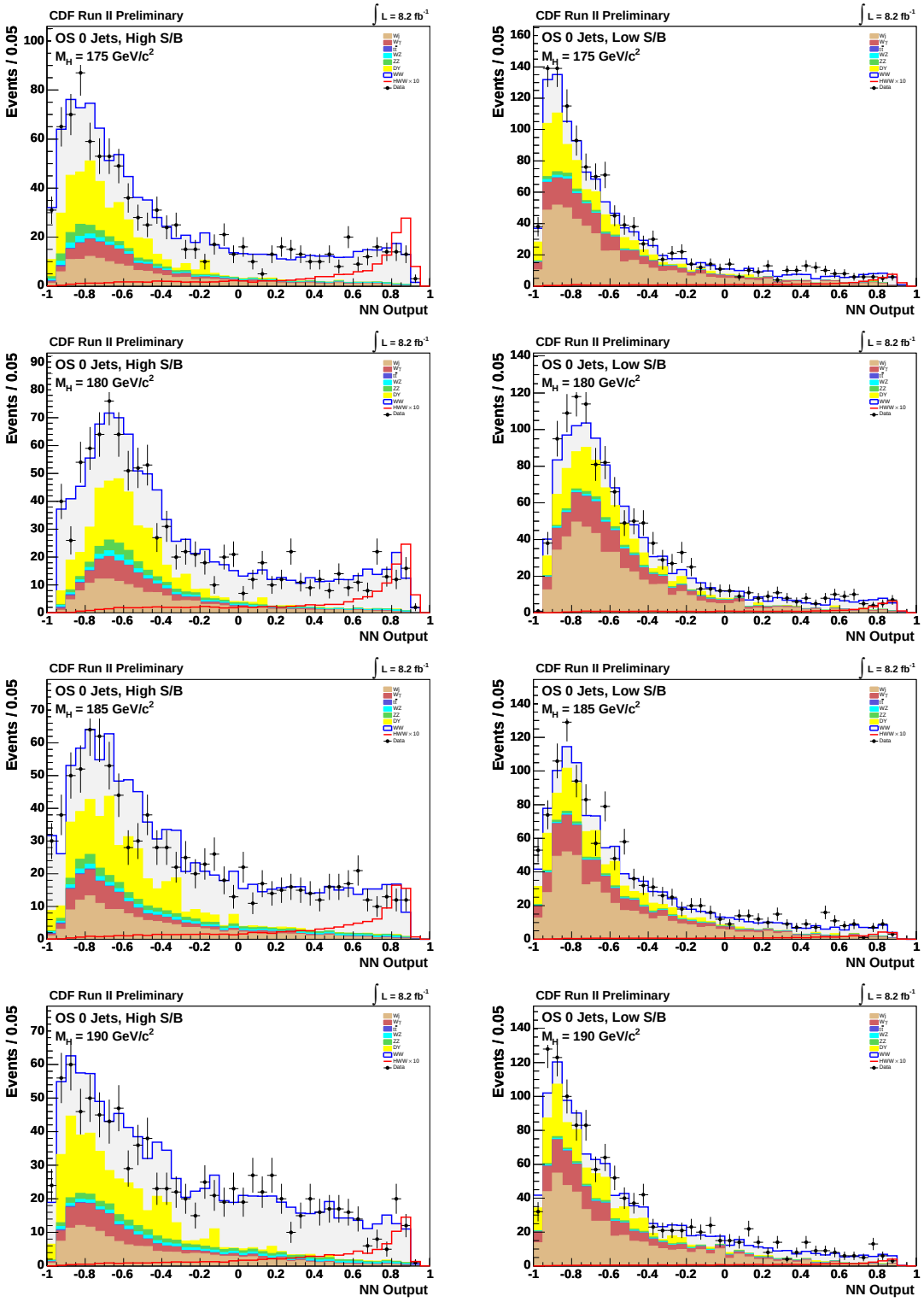

Figure 7.10: Output of the NN for Higgs masses of 175, 180, 185, and 190 GeV/c^2.

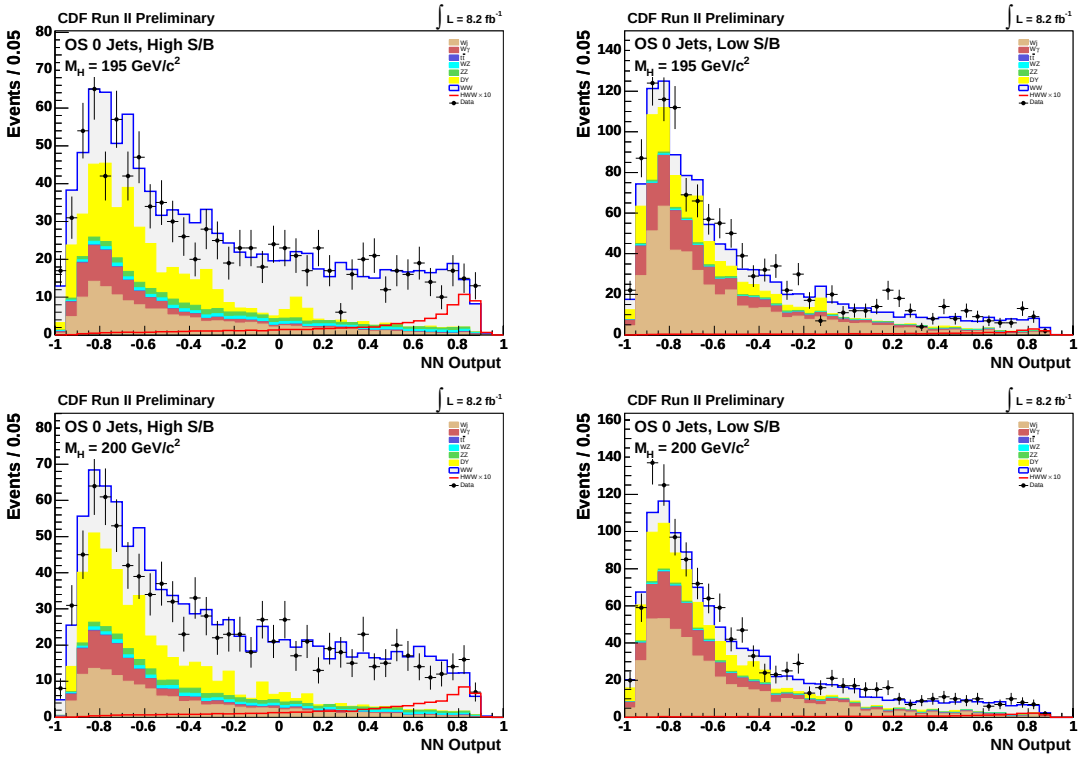

Figure 7.11: Output of the NN for Higgs masses of 195 and 200 GeV/c^2.

7.3 Systematic uncertainties

In the evaluation of systematic uncertainties, we attempted to take a conservative approach to provide the utmost confidence that the final Higgs exclusion limits are accurate. It is worth noting that the sensitivity of the analysis is statistically limited.

The systematic uncertainties we applied in this analysis fall into two categories, rate and shape. We used rate systematics to cover uncertainties in the normalizations applied to our various signal and background samples. Shape systematics cover uncertainties in the shape the signal and background contributions take in the score distributions output by the NNs.

To evaluate the individual systematic uncertainties, we varied parameters that would potentially have an impact on contributions (e.g. varying the jet energy scale by its associated uncertainty). We then determined, where applicable, the effect the parameter variation had on the overall size of a contribution to create a rate uncertainty, or the effect the contribution had on a bin by bin basis in the NN output to create a shape uncertainty.

For our rate systematics, there are three primary contributions. Cross-section uncertainties covered our lack of knowledge concerning the theoretical cross-sections used to normalize signal and background

contributions. We assigned acceptance uncertainties for variances in signal and background contributions based on efficiencies concerning selection cuts and detector geometry. We assigned an uncertainty for the amount of luminosity which was delivered to the CDF detector.

A summary of the systematic uncertainties applied in the 0 jets analysis appear in Table 7.4. Each row in the table shows a source of a systematic and the columns show the effect on a certain contribution by percent. The percentages in italic lying in the same row are considered to be 100% correlated. Negative values correspond to uncertainties which are negatively correlated among the various analysis channels.

7.3.1 Cross-section uncertainties

For the $t\bar{t}$ cross-section, which is known to next-to-next-to-leading order, we assign an uncertainty of 7% based on several theoretical calculations for the quantity [34][35][36]. For the diboson production cross-sections of $WW/WZ/ZZ$, we assign an uncertainty of 6% based on the theoretical calculation from [37].

For the purpose of setting a limit, this analysis requires knowledge of the Higgs cross-section uncertainty since we look for four production mechanisms simultaneously. The four production mechanisms each have different cross-sections, meaning we must account for each of their differing contributions.

The cross-section uncertainties for the Higgs signal vary among the production methods. The gluon fusion process dominating in this subsample, is known to next-to-next-to-leading order. However, gluon fusion is a QCD process so the uncertainty is significant. We utilized studies with the HNNLO program [38][39][40]. The HNNLO program evaluates the theoretical gluon fusion cross-section based on a next-to-next-to-leading order QCD calculation. The HNNLO program allows the user to vary the renormalization and factorization scales in the calculation and the PDF model. For the PDF models, we used the eigenfunctions from MSTW 2008 NNLO PDF [41]. These take into account uncertainties in the strong coupling constant $\alpha_s(q^2)$. We evaluated the scale uncertainty to be 7.0% and the PDF model uncertainty to be 7.7%.

For associated Higgs production, we know the production cross-section to next-to-next-to-leading order. The theoretical uncertainty is fairly small as a result. We applied an uncertainty of 5% based on results from [3]. The vector boson fusion cross-section is only known to next-to-leading order. As a result, the uncertainty is larger. We assign a systematic uncertainty of 10% [3].

7.3.2 Acceptance uncertainties

We assigned several acceptance systematics for effects such as trigger efficiency, higher order diagrams, and Drell-Yan modeling.

Uncertainty Source	WW	WZ	ZZ	$t\bar{t}$	DY	$W\gamma$	W+jet	$gg \to H$	WH	ZH	VBF
Cross Section											
ScaleInclusive								13.4%			
Scale1+Jets								−23%			
Scale2+Jets								0%			
PDF Model								7.6%			
Total	*6.0%*	*6.0%*	*6.0%*	7.0%					**5.0%**	**5.0%**	10.0%
Acceptance											
Scale (jets)	*0.3%*										
PDF Model (leptons)								2.7%			
PDF Model (jets)	*1.1%*							5.5%			
Higher-order Diagrams		*10.0%*	*10.0%*	10.0%		10.0%			**10.0%**	**10.0%**	**10.0%**
$\not{E}_T$ Modeling					19.5%						
Conversion Modeling						10.0%					
Jet Fake Rates											
(Low S/B)							22.0%				
(High S/B)							26.0%				
Jet Energy Scale	*2.6%*	*6.1%*	*3.4%*	*26.0%*	*17.5%*	*3.1%*		*5.0%*	*10.5%*	*5.0%*	*11.5%*
Lepton ID Efficiencies	*3.8%*	*3.8%*	*3.8%*	*3.8%*	*3.8%*			*3.8%*	*3.8%*	*3.8%*	*3.8%*
Trigger Efficiencies	*2.0%*	*2.0%*	*2.0%*	*2.0%*	*2.0%*			*2.0%*	*2.0%*	*2.0%*	*2.0%*
Luminosity	*5.9%*	*5.9%*	*5.9%*	*5.9%*	*5.9%*			*5.9%*	*5.9%*	*5.9%*	*5.9%*

Table 7.4: The systematics applied for the 0 jet analysis.

For lepton and trigger efficiency, we propagated the uncertainties from the measurements of each through the analysis. We assigned an uncertainty of 4.3% to the background and signal contributions to cover this.

The WW background contribution is particularly susceptible to uncertainties due to higher order effects. To examine the effect, we again employed the MC@NLO generator [18] and varied the choices for the scales and PDF input model using results from the calculations done in [41]. We took the uncertainty based on changes in the observed acceptance. For other backgrounds known only to leading order, we used the difference in the WW acceptance observed from a leading order calculation with PYTHIA [16] versus the next-to-leading order calculation with MC@NLO. We found this difference to be 10%.

A large systematic from Drell-Yan enters through the modeling of fake $\not\!\!E_T$. We tuned the model for Drell-Yan using events with an intermediate $\not\!\!E_T$. The tuning selects events just below the normal $\not\!\!E_T$ cutoff. We varied the tuning parameters and assigned a 20% systematic uncertainty based on the observed variations.

In order to account for uncertainties related to the jet energy scale, we varied the scale up and down by one standard deviation to determine its effect. The systematic uncertainties between analysis samples are highly correlated, a change in the jet energy scale can make a 1-jet event into 2-jet event.

We assigned a 10% uncertainty to the $W+\gamma$ background contribution which arises from the description of the detector material and conversion veto efficiency. Additionally, the $W+\gamma$ contribution received a scale factor from a same-sign, low M_{ll} control region. We assigned a systematic based on the sample's statistics as well as uncertainty from non-$W+\gamma$ events appearing in the sample. We propagated this uncertainty through into the signal samples.

For the uncertainty on the $W+$ jets contribution, we used the differences in the probability of a jet faking a lepton (fake rate) between the four trigger samples, each having a different requirement on E_T. The variations corresponded to uncertainties with the jet parton composition and contamination from real leptons.

7.3.3 Luminosity uncertainty

The uncertainty on the luminosity arises from primarily two sources, uncertainty in the inelastic $p\bar{p}$ cross-section and measurement acceptance based on detector geometry. We assigned a systematic of 5.9%, making it 100% correlated between the subsamples.

7.3.4 Shape uncertainties

To examine possible shape systematics in the gluon fusion Higgs shape, we varied the Higgs p_T spectrum originally obtained from the HqT program [42][43] in our simulated events. The choices for the re-weighting functions used in the variations come from the ResBos program [44][45][46]. The re-weighting functions come from the difference between the ResBos Higgs p_T spectrum using our default scale and the p_T spectrum determined by raising and lowering the scale choices by a factor of two. To implement the modified p_T spectra, we re-weighted our signal samples so that their generator level spectra matched the modified spectra. We then examine the effect on the shape of the NN output distribution.

Another shape systematic arises from uncertainties related to the p_T spectra of the WW system. We made use of the PYTHIA 8 MC generator to create reweightings for the p_T spectrum that we could then apply to our MC@NLO sample. With the reweighted WW sample, we were able to evaluate the effect that it had on the shape of the WW background in the NN output distribution.

We further examined the effect JES uncertainties would have on NN shape. To determine any effects, we varied the JES by ± 1 σ. The variations we saw were minimal, so we considered any effect the JES uncertainty had on the NN shape to be negligible.

7.4 Confidence level limit on Higgs production

With the NN output showing no signal from $H \rightarrow WW$, we set 95% confidence level limits on Higgs production in the 0-jet sample. We took a Bayesian approach in setting the limits, evaluating the limits at 19 Higgs masses between 110-200 GeV/c^2, in increments of 5 GeV/c^2. We present the ratio of the measured limit on the cross-section to the expectation from the Standard Model.

We construct a likelihood $\mathcal{L}$

$$\mathcal{L}(R|\vec{\theta},\vec{n}) = \prod_i \frac{\mu_i^{n_i} e^{-\mu_i}}{n_i!} \times \prod_k e^{-\frac{\theta_k^2}{2}}, \tag{7.6}$$

for each of the nineteen Higgs masses. The likelihood is just the product of Poisson probabilities to observe in the i-th bin of the NN distribution, a quantity of n_i events for the expectation of μ_i events. The expected number of events can also be written in terms of the expected signal s_i and the expected background b_i as

$$\mu_i = R \times s_i(\vec{\theta}) + b_i(\vec{\theta}). \tag{7.7}$$

Here, R is a multiplicative factor used to scale the signal contribution during limit setting. We assume a

flat prior for R. The amount of signal can be expressed as $s_i = L \times \epsilon \times \sigma_H^{SM}$, where L is the integrated luminosity, ϵ is the detection efficiency, and σ_H^{SM} is the cross-section for the Standard Model Higgs. The signal and background contributions depend on systematic uncertainties through

$$s_i(\vec{\theta}) = s_i \times \prod_k (1 + u_i^k \times \theta_k) \tag{7.8}$$

and

$$b_i(\vec{\theta}) = b_i \times \prod_k (1 + u_i^k \times \theta_k). \tag{7.9}$$

Here, the index k corresponds to systematic uncertainties which have an effect on the count of events. The error associated with the systematic is u_k^i. The amount of variation for a systematic k is expressed in the nuisance parameter θ_k, for which we assume a Gaussian prior.

We proceed to integrate the likelihood over the nuisance parameters θ_k, leaving the posterior probability $\mathcal{L}(R)$. We can then produce the 95% confidence level limit from

$$0.95 = \frac{\int_0^{R^{CL}} \mathcal{L}(R) dR}{\int_0^{\infty} \mathcal{L}(R) dR}, \tag{7.10}$$

where R^{CL} is the limit determined.

In order to estimate our sensitivity, we created a set of pseudo-experiments assuming a background only hypothesis. We generated the pseudo-experiments following a Poisson distribution for each bin i, for an expected number of events b_i. We account for systematic variables by varying b_i by its error. For each pseudo-experiment, we reevaluated the limit. When displaying the limit for a given channel, we display bands for deviations of 1 and 2σ off of the expected limit.

7.5 Results on the confidence level limit on Higgs production in the 0 jets subsample

With the method described in the previous section, we determined the expected and observed limits. We made use of 10,000 pseudo-experiments in determining the expected limits. We present the results as the ratio of the observed limit to the Standard Model expectation. The expected and observed limits appear in Table 7.5. A plot of the results appear in Figure 7.12. The green and yellow error bands present in Figure 7.12 incorporate both statistical and systematic uncertainties.

Overall, we see good agreement between the observed and expected limits. We end up seeing the most

OS 0 Jets	110	115	120	125	130	135	140	145	150	155
$-2\sigma/\sigma_{SM}$	15.30	8.44	5.16	3.58	2.84	2.09	1.79	1.59	1.40	1.15
$-1\sigma/\sigma_{SM}$	21.57	11.74	7.34	5.05	3.97	2.94	2.57	2.29	2.01	1.62
Median/σ_{SM}	**31.12**	**16.94**	**10.64**	**7.26**	**5.70**	**4.28**	**3.70**	**3.32**	**2.94**	**2.35**
$+1\sigma/\sigma_{SM}$	45.68	24.71	15.56	10.61	8.40	6.29	5.45	4.91	4.36	3.46
$+2\sigma/\sigma_{SM}$	66.98	36.07	22.57	15.32	12.09	9.13	7.96	7.19	6.32	5.02
Observed/σ_{SM}	**15.52**	**12.10**	**6.89**	**4.75**	**4.57**	**4.23**	**3.30**	**2.62**	**2.49**	**2.75**

OS 0 Jets	160	165	170	175	180	185	190	195	200
$-2\sigma/\sigma_{SM}$	0.81	0.82	0.89	1.13	1.39	1.81	2.18	2.69	3.09
$-1\sigma/\sigma_{SM}$	1.14	1.14	1.24	1.59	1.93	2.49	3.06	3.78	4.30
Median/σ_{SM}	1.64	**1.65**	**1.78**	**2.28**	**2.77**	**3.60**	**4.37**	**5.49**	**6.17**
$+1\sigma/\sigma_{SM}$	2.41	2.39	2.60	3.36	4.05	5.25	6.43	8.06	9.10
$+2\sigma/\sigma_{SM}$	3.46	3.51	3.76	4.89	5.86	7.46	9.46	11.77	13.24
Observed/σ_{SM}	1.93	**1.92**	**1.67**	**2.28**	**2.82**	**3.68**	**6.12**	**8.51**	**8.17**

Table 7.5: The expected and observed limits over the mass range of 110-200 GeV/c^2.

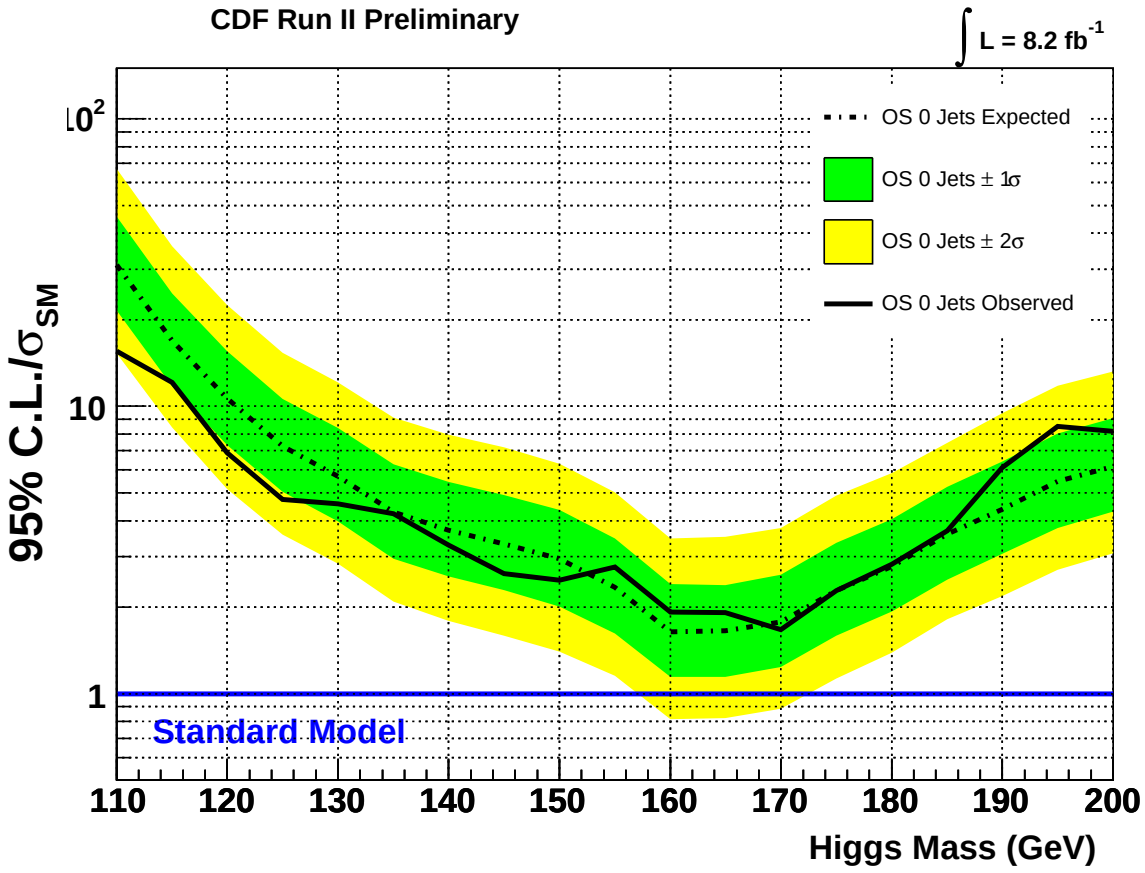

Figure 7.12: A plot of the expected and observed limits over the mass range of 110-200 GeV/c^2.

sensitivity at a mass of 170 GeV/c^2, with a ratio of limit to Standard Model expectation of 1.67.

Chapter 8

Analysis of events with jet activity

As mentioned in the last chapter, we split the data into subsamples to capitalize on the differences between signal and background contributions based on the number of jets. This chapter presents results concerning events with one jet and events with two or more jets. In these two subsamples, contributions from associated and vector boson fusion become more substantial.

8.1 Analysis of events with one jet

In the analysis of events with one jet, we divided up the sample into high and low S/B as done in the 0 jets analysis. The expected signal and background contributions compared to data appear in Tables 8.1 and 8.2 for high and low S/B and assuming a Higgs mass of 165 GeV/c^2. In Table 8.3, the combination of high and low S/B appears.

8.1.1 Multivariate techniques

The matrix element technique is not used since it is expected to not be as powerful as it was in the 0 jets category. We still make use of a NN however. We again trained the network for 19 Higgs masses between 110-200 GeV/c^2, one every increment of 5 GeV/c^2. The kinematic variables we selected as inputs are:

- H_T: The sum of the lepton p_T, jet E_T, and event $\not\!\!E_T$
- $\Delta\phi(ll)$: The difference in ϕ between the two leptons
- $\Delta R(ll)$: The difference in ΔR between the two leptons
- $M(ll)$: The combined mass of the leptons
- $p_T(l_1)$: The transverse momentum of the leading lepton
- $p_T(l_2)$: The transverse momentum of the subleading lepton
- $E(l_1)$: The energy of the leading lepton

CDF Run II Preliminary	$\int \mathcal{L} = 8.2$ fb^{-1}		
$M_H = 165$ GeV/c^2			
$t\bar{t}$	64	$\pm$	12
DY	190	$\pm$	44
WW	156	$\pm$	19
WZ	22.5	$\pm$	3.1
ZZ	9.8	$\pm$	1.4
W+jets	43	$\pm$	12
$W\gamma$	8.2	$\pm$	1.4
Total Background	493	$\pm$	63
$gg \to H$	9.3	$\pm$	3.9
WH	1.25	$\pm$	0.20
ZH	0.481	$\pm$	0.074
VBF	0.89	$\pm$	0.15
Total Signal	11.9	$\pm$	4.0
Data	457		

HighSB-1J

Table 8.1: The expected signal and background contributions compared with data for the high S/B grouping in events having one jet.

CDF Run II Preliminary	$\int \mathcal{L} = 8.2$ fb^{-1}		
$M_H = 165$ GeV/c^2			
$t\bar{t}$	20.7	$\pm$	3.9
DY	146	$\pm$	34
WW	66.0	$\pm$	8.0
WZ	13.7	$\pm$	1.9
ZZ	4.85	$\pm$	0.70
W+jets	134	$\pm$	21
$W\gamma$	25.9	$\pm$	4.4
Total Background	411	$\pm$	46
$gg \to H$	3.0	$\pm$	1.3
WH	0.394	$\pm$	0.063
ZH	0.147	$\pm$	0.023
VBF	0.254	$\pm$	0.044
Total Signal	3.8	$\pm$	1.3
Data	418		

LowSB-1J

Table 8.2: The expected signal and background contributions compared with data for the low S/B grouping in events having one jet.

CDF Run II Preliminary	$\int \mathcal{L} = 8.2$ fb^{-1}		
$M_H = 165$ GeV/c^2			
$t\bar{t}$	85	$\pm$	16
DY	336	$\pm$	78
WW	222	$\pm$	27
WZ	36.1	$\pm$	5.0
ZZ	14.6	$\pm$	2.1
W+jets	177	$\pm$	33
$W\gamma$	34.0	$\pm$	5.8
Total Background	900	$\pm$	110
$gg \to H$	12.2	$\pm$	5.2
WH	1.64	$\pm$	0.26
ZH	0.629	$\pm$	0.097
VBF	1.14	$\pm$	0.20
Total Signal	15.6	$\pm$	5.3
Data	875		

All

Table 8.3: The expected signal and background contributions compared with data for the combination of the high and low S/B groupings in events having one jet.

- $M_T(ll\not\!\!E_T)$: The transverse mass of the two leptons and $\not\!\!E_T$
- $\not\!\!E_{T\,spec}$: A variation on $\not\!\!E_T$ implemented to separate DY defined in Equation 6.1

As with the 0 jet events, we chose the kinematic variables above to maximize Higgs signal sensitivity. Note, we have redefined the variable H_T from the 0 jets portion of the analysis. The H_T variable provides useful discrimination against the more prevalent $t\bar{t}$ background seen in the one jet case. Once again, $\Delta\phi(ll)$ and $\Delta R(ll)$ are potent discriminants since the spin correlation still results in the leptons preferentially heading in the same direction. The kinematic plots of the NN inputs appear in Figures 8.1 and 8.2. The outputs of the NN for a Higgs mass of 165 GeV/c^2 appear in Figure 8.3. The outputs for the other Higgs masses appear in Figures 8.4-8.8.

8.1.2 Systematic uncertainties

We described the systematic uncertainties in the previous chapter. The size of the systematics in percentages appear in Table 8.4.

8.1.3 Results in the one jet analysis

As with the 0 jets subsample, we saw no evidence for Higgs production in events with one jet. We proceeded to set a limit using the same technique described in the previous chapter. The expected and observed limits appear in Table 8.5. A plot of the results appear in Figure 8.9.

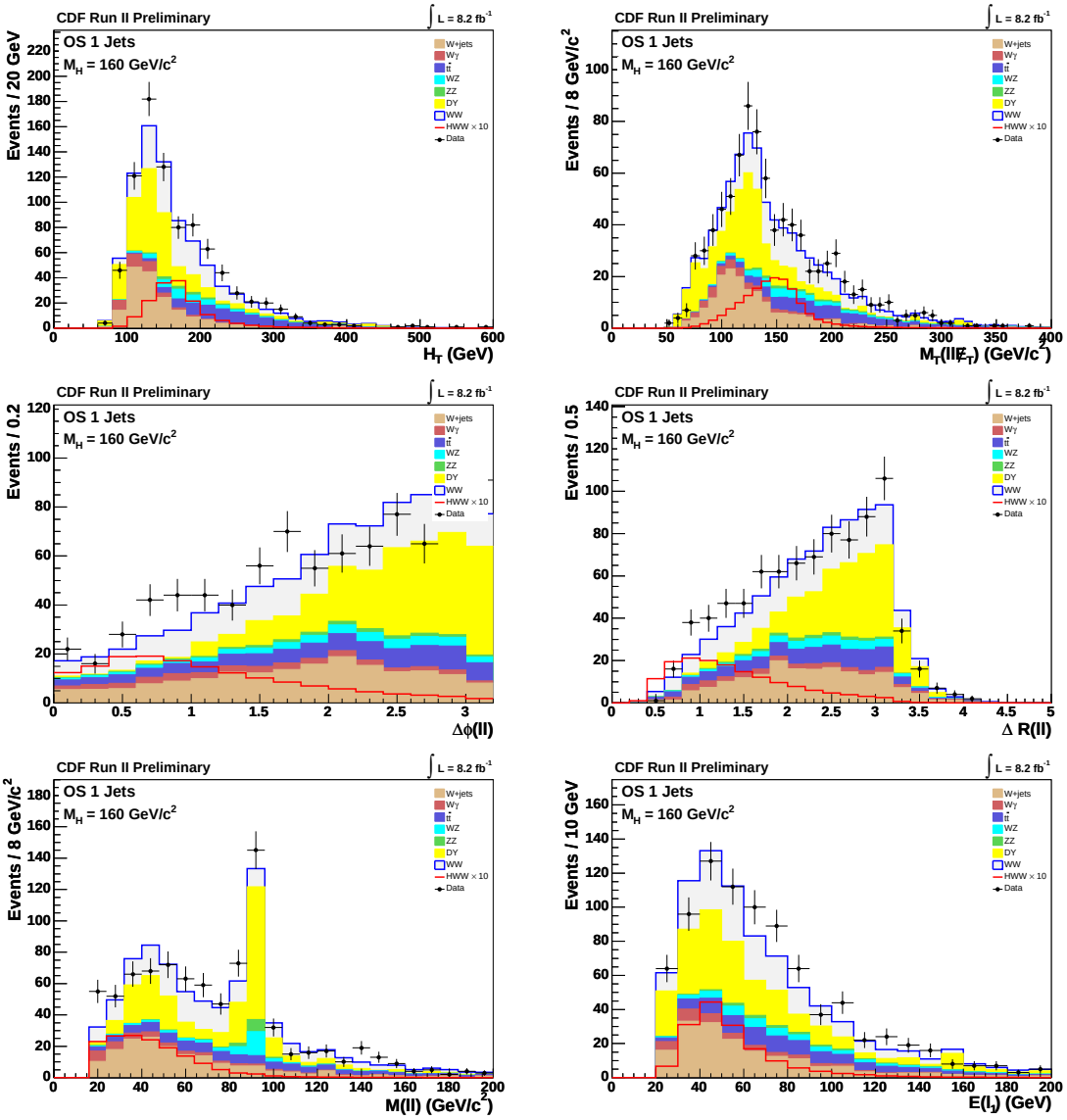

Figure 8.1: Inputs to the NN in the one jet category, for a Higgs mass of 160 GeV/c^2.

Uncertainty Source	WW	WZ	ZZ	$t\bar{t}$	DY	$W\gamma$	W+jet	$gg \to H$	WH	ZH	VBF
Cross Section											
ScaleInclusive								0%			
Scale1+Jets								35%			
Scale2+Jets								-12.7%			
PDF Model								17.3%			
Total	*6.0%*	*6.0%*	*6.0%*	7.0%					**5.0%**	**5.0%**	10.0%
Acceptance											
Scale (jets)	*-4.0%*										
PDF Model (leptons)								*3.6%*			
PDF Model (jets)	*4.7%*							-6.3%			
Higher-order Diagrams		*10.0%*	*10.0%*	10.0%		10.0%			**10.0%**	**10.0%**	**10.0%**
$\not{E}_T$ Modeling					20.0%						
Conversion Modeling						10.0%					
Jet Fake Rates											
(Low S/B)							23.0%				
(High S/B)							29.0%				
Jet Energy Scale	*-5.5%*	*-1.0%*	*-4.3%*	*-13.0%*	*-6.5%*	*-9.5%*		*-4.0%*	*-8.5%*	*-7.0%*	*-6.5%*
Lepton ID Efficiencies	*3.8%*	*3.8%*	*3.8%*	*3.8%*	*3.8%*			*3.8%*	*3.8%*	*3.8%*	*3.8%*
Trigger Efficiencies	*2.0%*	*2.0%*	*2.0%*	*2.0%*	*2.0%*			*2.0%*	*2.0%*	*2.0%*	*2.0%*
Luminosity	*5.9%*	*5.9%*	*5.9%*	*5.9%*	*5.9%*			*5.9%*	*5.9%*	*5.9%*	*5.9%*

Table 8.4: The systematics applied for the 1 jet analysis.

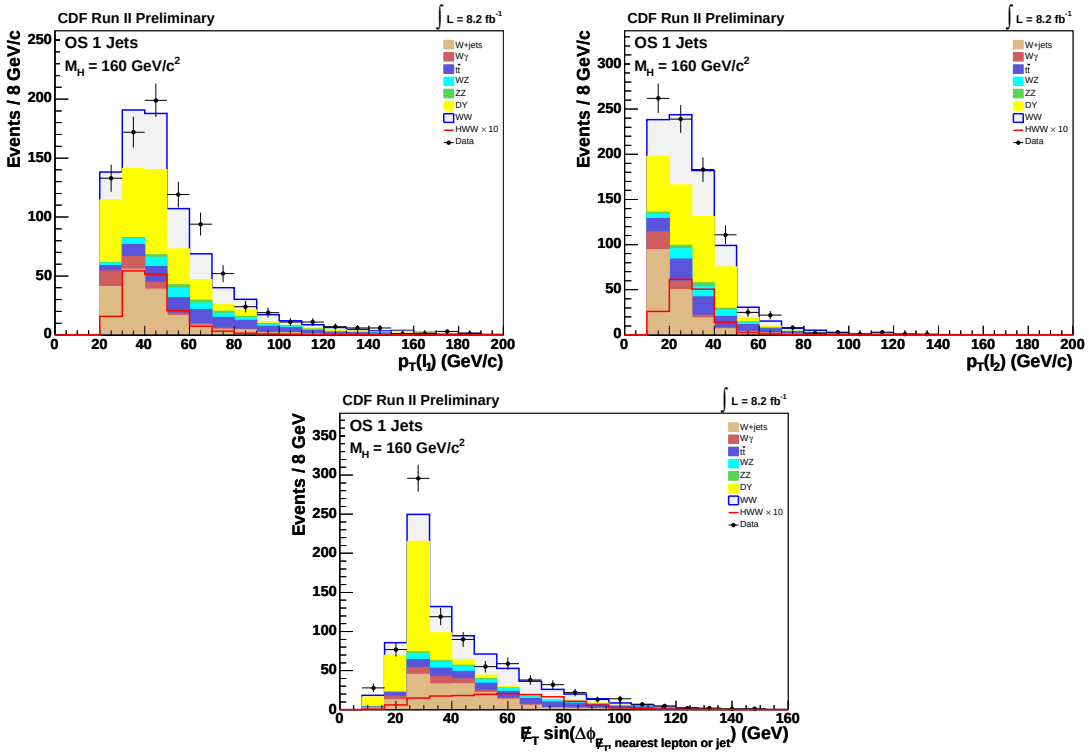

Figure 8.2: Inputs to the NN in the one jet category, for a Higgs mass of 160 GeV/c^2.

OS 1 Jet	110	115	120	125	130	135	140	145	150	155
$-2\sigma/\sigma_{SM}$	22.48	12.42	7.40	4.94	3.61	2.86	2.36	2.05	1.67	1.43
$-1\sigma/\sigma_{SM}$	31.77	17.63	10.64	7.09	5.13	4.08	3.38	2.94	2.40	2.03
Median/σ_{SM}	**47.15**	**25.99**	**15.68**	**10.52**	**7.53**	**6.00**	**4.98**	**4.33**	**3.54**	**2.97**
$+1\sigma/\sigma_{SM}$	71.72	39.45	23.53	15.85	11.45	8.95	7.56	6.44	5.30	4.53
$+2\sigma/\sigma_{SM}$	110.54	60.62	36.29	24.13	16.94	13.34	11.49	10.00	8.14	6.82
Observed/σ_{SM}	**82.54**	**34.19**	**18.23**	**12.24**	**9.13**	**6.95**	**7.10**	**5.76**	**5.38**	**3.78**

OS 1 Jet	160	165	170	175	180	185	190	195	200
$-2\sigma/\sigma_{SM}$	1.11	1.05	1.23	1.50	1.74	2.26	2.80	3.22	3.82
$-1\sigma/\sigma_{SM}$	1.54	1.47	1.75	2.14	2.49	3.22	4.01	4.71	5.64
Median/σ_{SM}	**2.27**	**2.17**	**2.57**	**3.16**	**3.66**	**4.78**	**5.89**	**7.09**	**8.42**
$+1\sigma/\sigma_{SM}$	3.45	3.28	3.89	4.76	5.54	7.18	8.94	10.80	12.79
$+2\sigma/\sigma_{SM}$	5.29	4.95	5.93	7.22	8.38	10.89	13.96	16.48	19.28
Observed/σ_{SM}	**2.45**	**2.51**	**4.48**	**4.84**	**6.64**	**8.04**	**13.13**	**14.79**	**19.60**

Table 8.5: The expected and observed limits in the one jet category, over the mass range of 110-200 GeV/c^2.

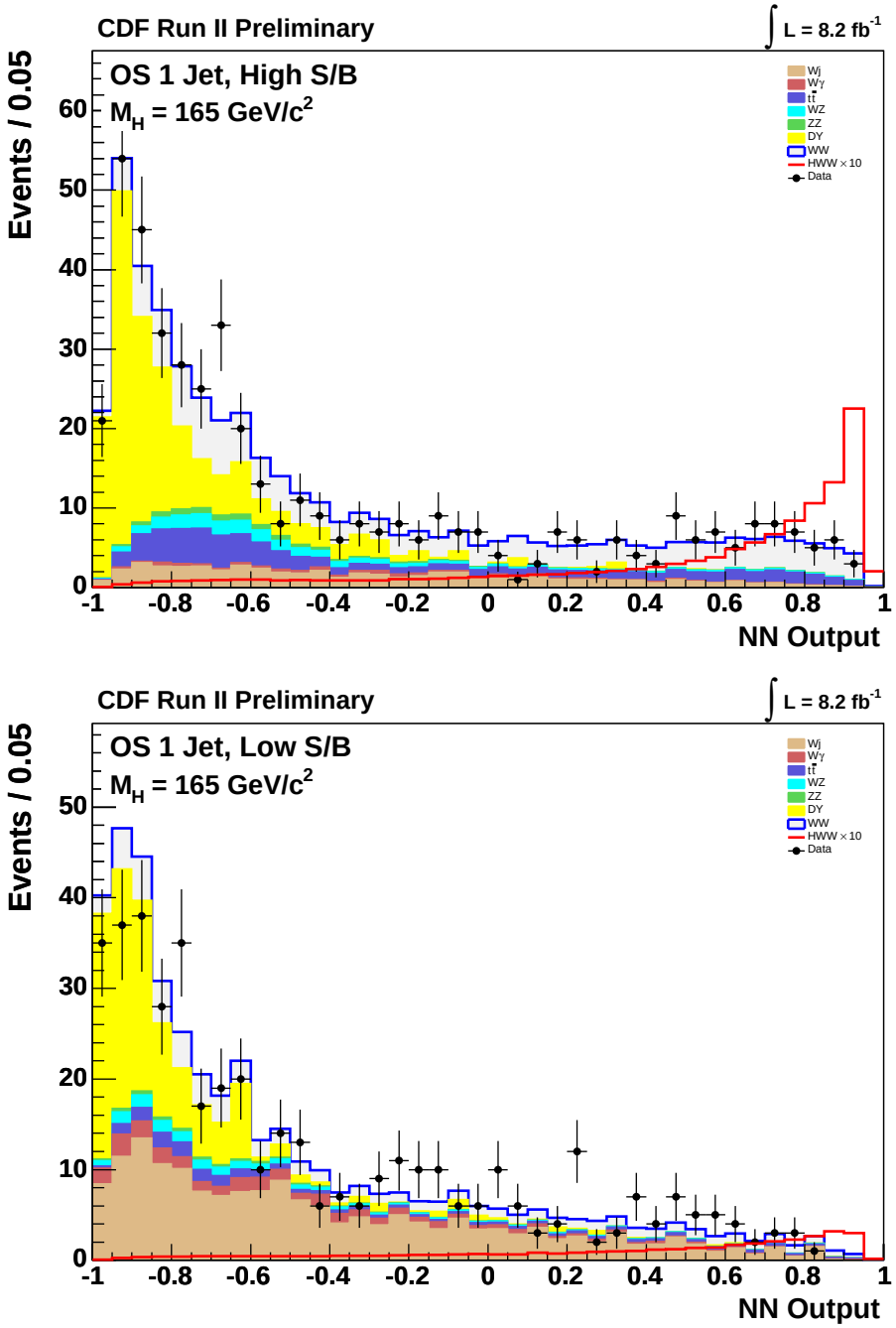

Figure 8.3: Output of the NN in the one jet category, for a Higgs mass of 165 GeV/c^2.

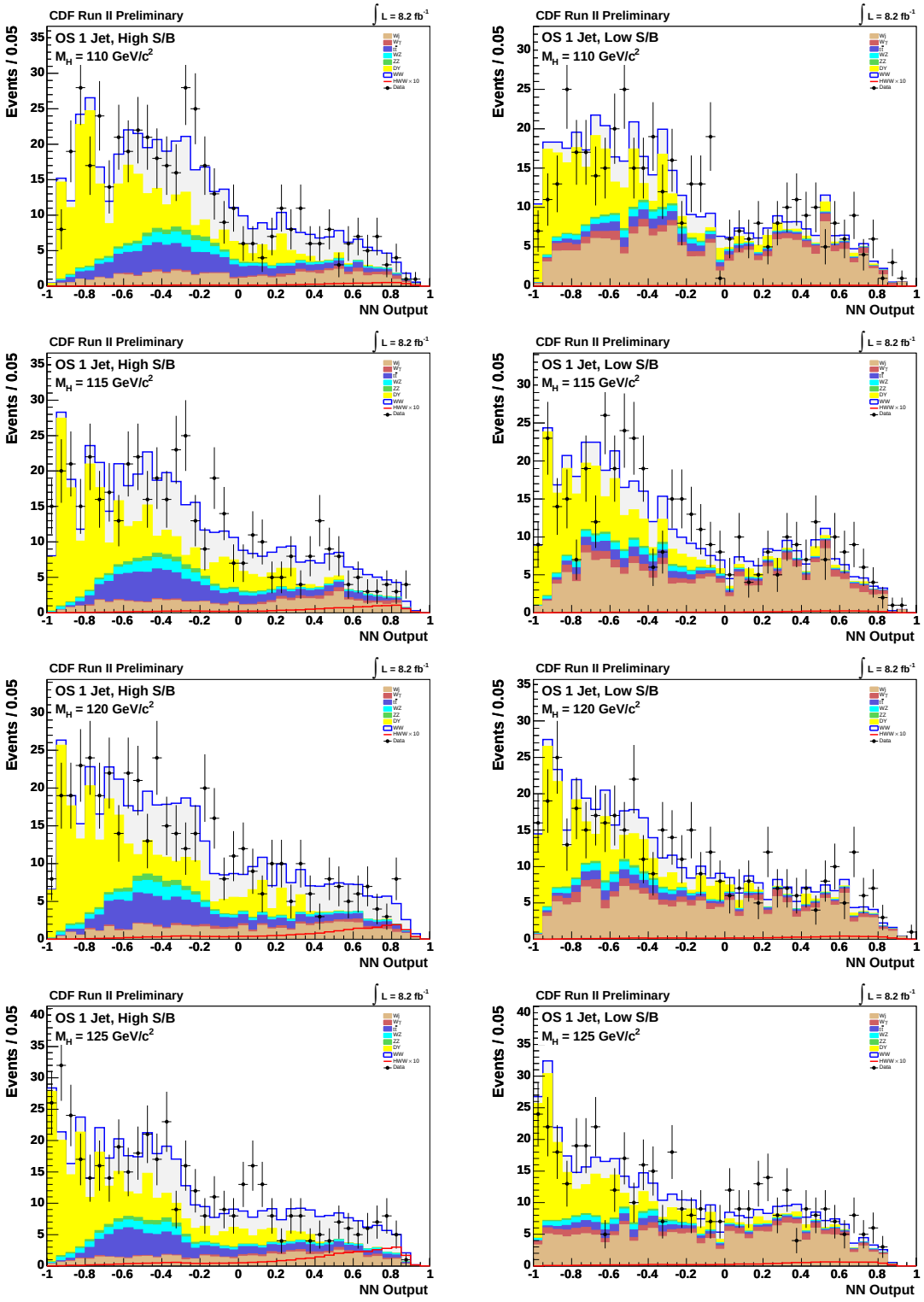

Figure 8.4: Output of the NN in the one jet category, for Higgs masses of 110, 115, 120, and 125 GeV/c^2.

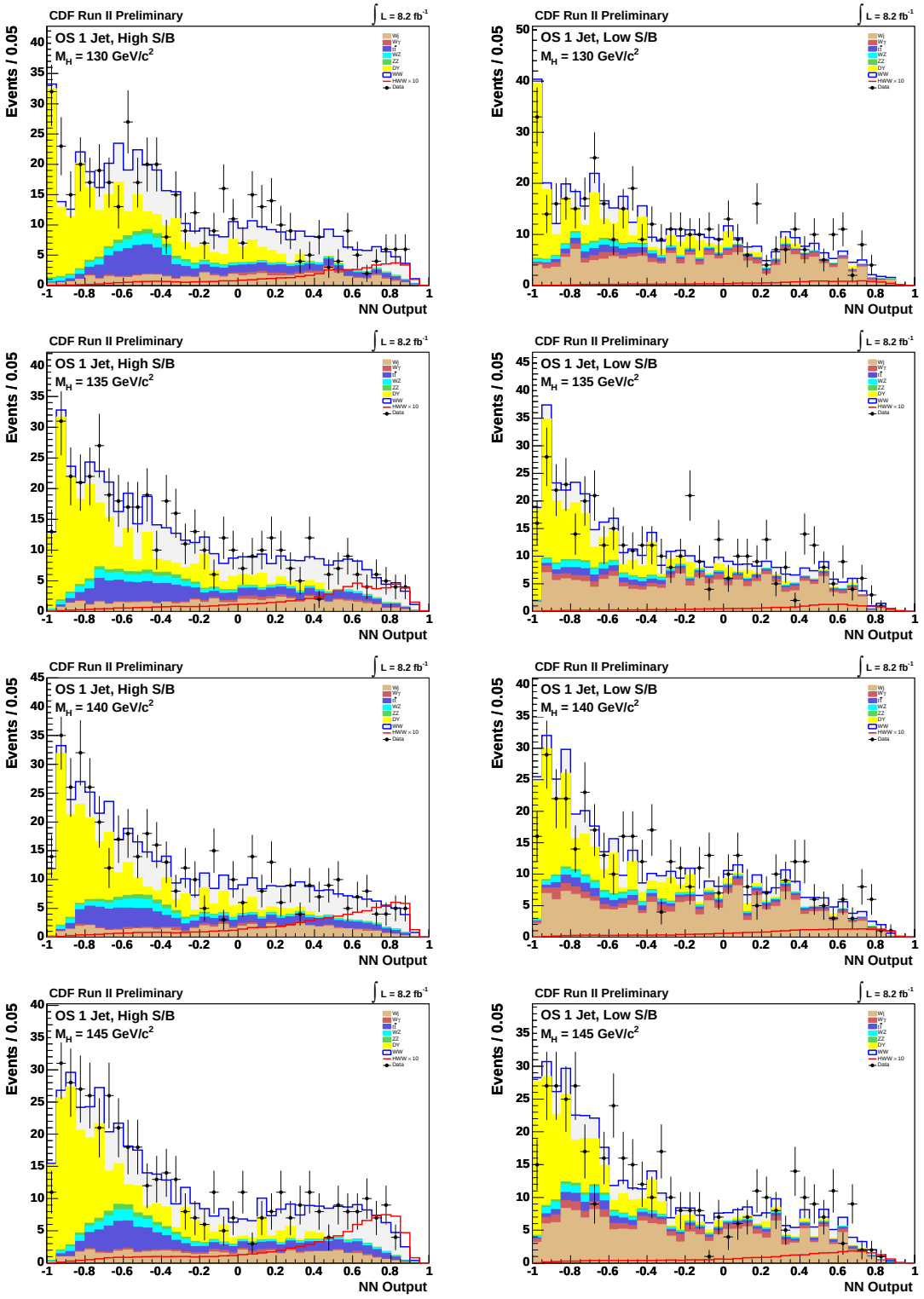

Figure 8.5: Output of the NN in the one jet category, for Higgs masses of 130, 135, 140, and 145 GeV/c^2.

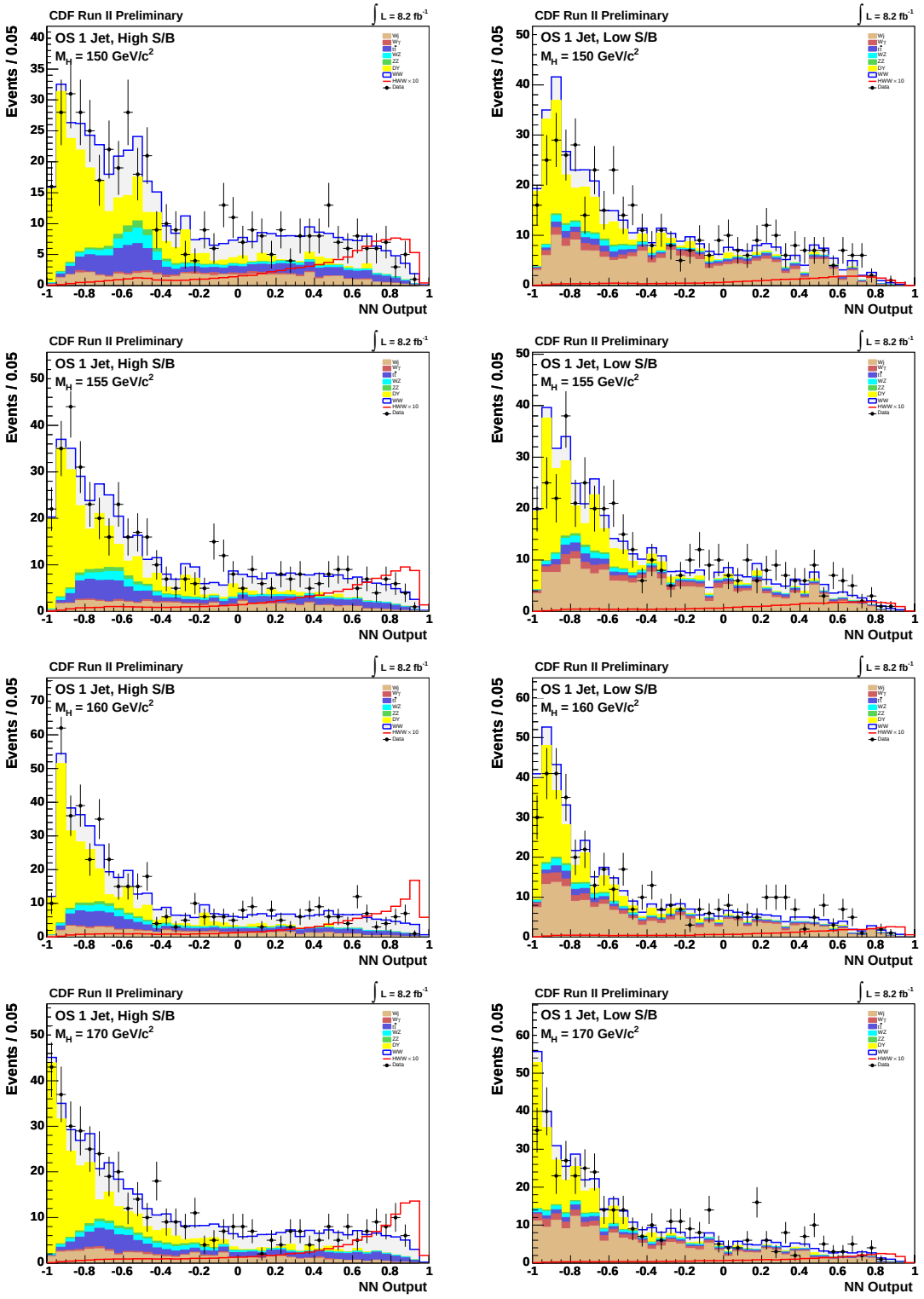

Figure 8.6: Output of the NN in the one jet category, for Higgs masses of 150, 155, 160, and 170 GeV/c^2.

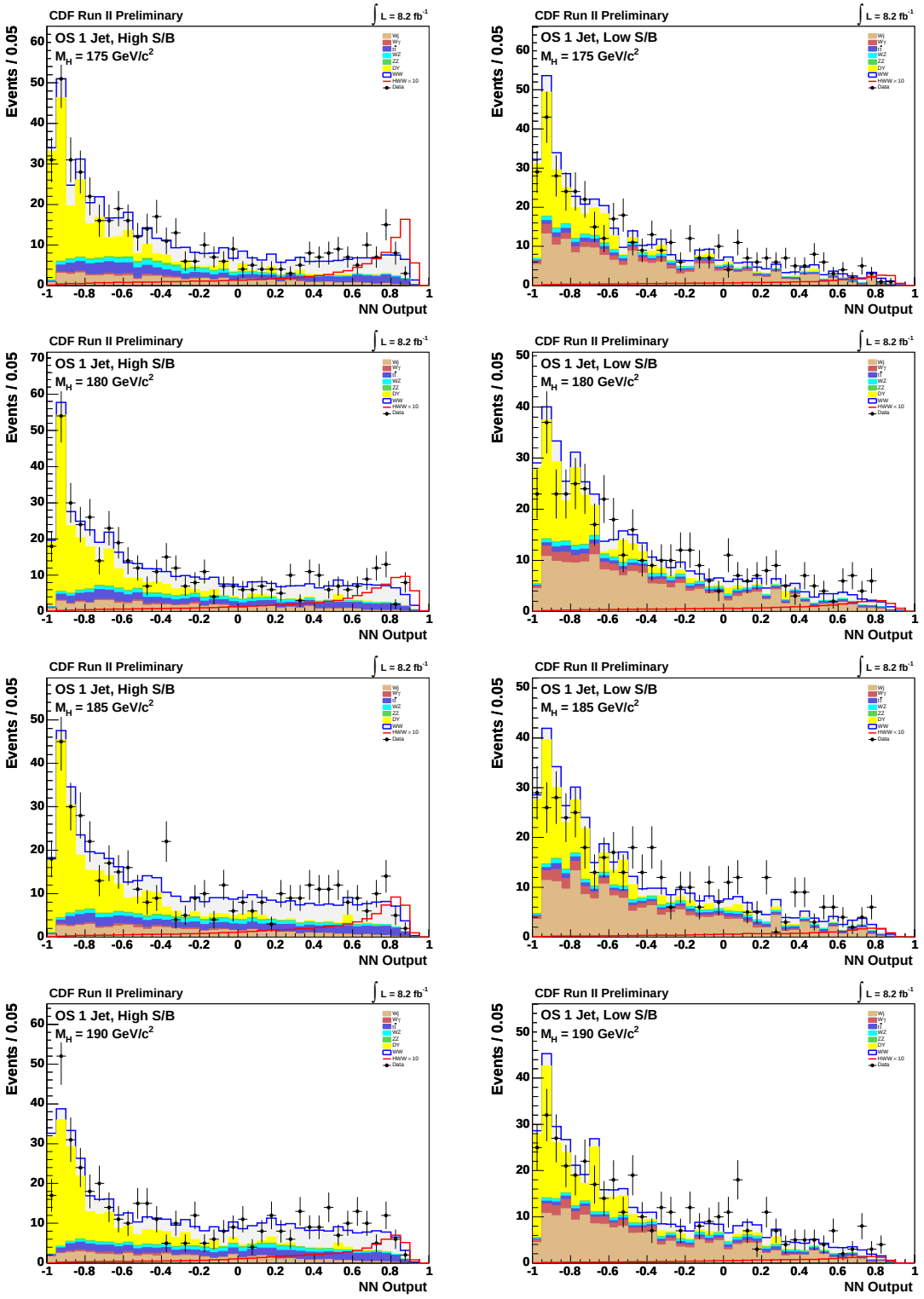

Figure 8.7: Output of the NN in the one jet category, for Higgs masses of 175, 180, 185, and 190 GeV/c^2.

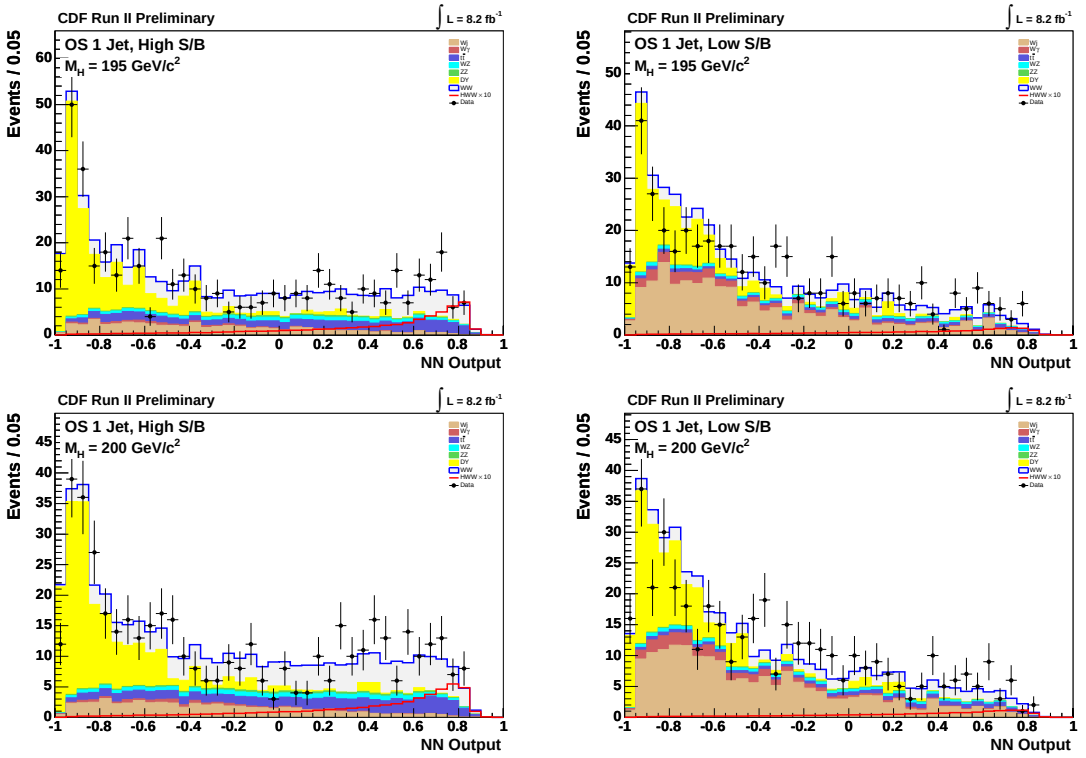

Figure 8.8: Output of the NN in the one jet category, for Higgs masses of 195 and 200 GeV/c^2.

Overall, we observed good agreement between the observed and expected limits. We end up with the most sensitivity at a mass of 160 GeV/c^2, with a ratio of limit to Standard Model expectation of 2.45.

8.2 Analysis of events with two or more jets

In the analysis of events with two or more jets, the dominate background is $t\bar{t}$. The top decays of $t \to W(W \to l\nu)b$ produce both high p_T leptons and $\not\!\!E_T$, looking very similar to our signal's signature. To suppress this background, we made use of the b-tagging algorithm `SECVTX` [47]. The `SECVTX` algorithm identifies b-jets by looking for secondary vertices consistent with a b decay. The long lifetime of bottom quarks gives us tracks with large impact parameters which the `SECVTX` algorithm looks for.

To be accepted into the analysis, events with two or more jets must not have any jets tagged by the `SECVTX` algorithm. We estimated that rejecting `SECVTX` tags eliminates 59% of the $t\bar{t}$ background from the sample with a negligible loss of signal events. Our expected number of background and signal contributions as compared to data appear in Table 8.6.

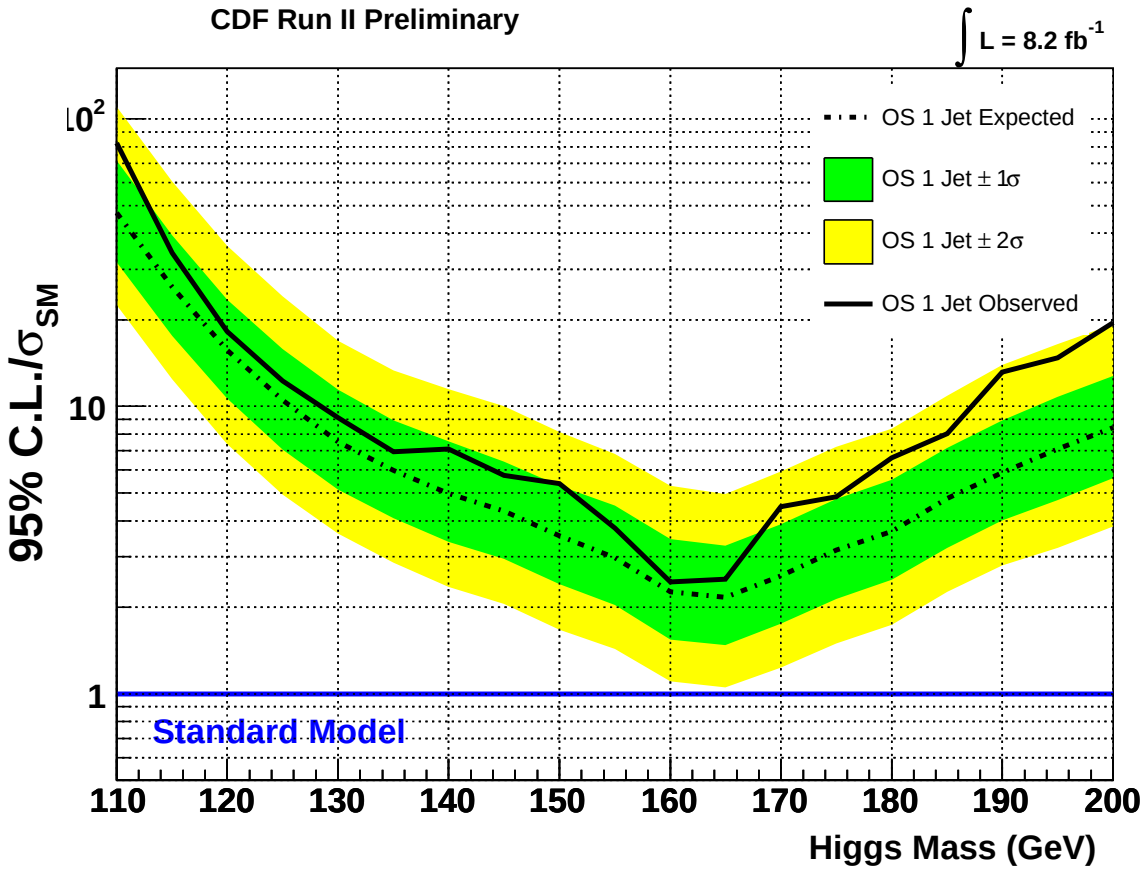

Figure 8.9: A plot of the expected and observed limits in the one jet category, over the mass range of 110-200 GeV/c^2.

CDF Run II Preliminary $\int \mathcal{L} = 8.2$ fb^{-1}			
$M_H = 165$ GeV/c^2			
$t\bar{t}$	244	±	36
DY	132	±	53
WW	49.7	±	9.7
WZ	9.9	±	1.9
ZZ	4.47	±	0.86
W+jets	62	±	12
$W\gamma$	6.2	±	1.6
Total Background	509	±	79
$gg \rightarrow H$	4.3	±	2.1
WH	3.69	±	0.51
ZH	1.84	±	0.25
VBF	2.13	±	0.35
Total Signal	11.9	±	2.5
Data		494	

AllSB-2JOS

Table 8.6: The expected signal and background contributions compared with data for events having two or more jets.

8.2.1 The $t\bar{t}$ control region

The SECVTX algorithm allowed us to define a control region to closely examine our $t\bar{t}$ modeling. We defined the region as being the events in the 2 or more jets category which posses a SECVTX b-tag. We show several kinematic variables in Figure 8.10. Overall, we see good agreement between data and our $t\bar{t}$ background model.

8.2.2 Multivariate techniques

As with the 1 jets events, we do not use the matrix element technique for 2 ore more jets events. We again use a NN, training the network for 19 Higgs masses between 110-200 GeV/c^2, one every increment of 5 GeV/c^2. The kinematic variables we selected as inputs are:

- H_T: The sum of the lepton p_T, jet E_T, and event $\not\!\!E_T$
- $p_T(j_1, j_2)$: The transverse momentum of the two leading jets
- $\Delta\phi(ll)$: The difference in ϕ between the two leptons
- $\Delta R(ll)$: The difference in ΔR between the two leptons
- $\Delta\phi(ll, \not\!\!E_T)$: The difference in ϕ between the combined p_T of the two leptons and $\not\!\!E_T$
- $M(ll)$: The combined mass of the leptons
- $p_T(l_1)$: The transverse momentum of the leading lepton
- $p_T(l_2)$: The transverse momentum of the subleading lepton

As in events with 1 jets, the H_T variable provided useful discrimination against the still dominate $t\bar{t}$ background. The $p_T(j_1, j_2)$ variable also helped discriminate Higgs signal from the $t\bar{t}$ background. Once again, $\Delta\phi(ll)$ and $\Delta R(ll)$ provide potent discrimination due to the Higgs spin correlation. The kinematic plots of the NN inputs appear in Figure 8.11. The outputs of the NN for a Higgs mass of 165 GeV/c^2 appear in Figure 8.12. The outputs for the other Higgs masses appear in Figures 8.13-8.15.

8.2.3 Systematic uncertainties

With the systematic uncertainties described in the previous chapter. The size of the systematics in percentages appear in Table 8.7.

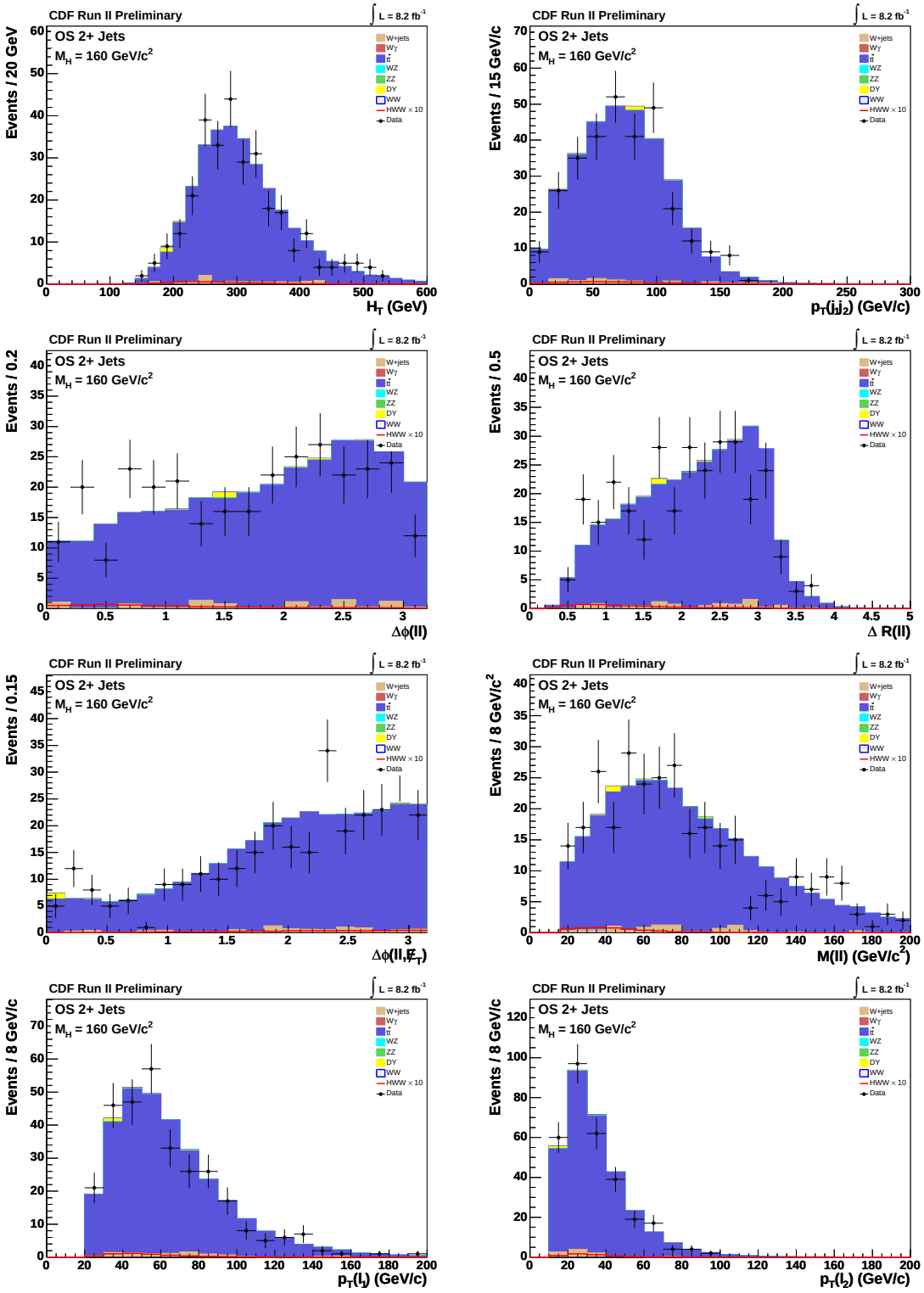

Figure 8.10: Kinematic distributions in the $t\bar{t}$ control region for a Higgs mass of 160 GeV/c^2.

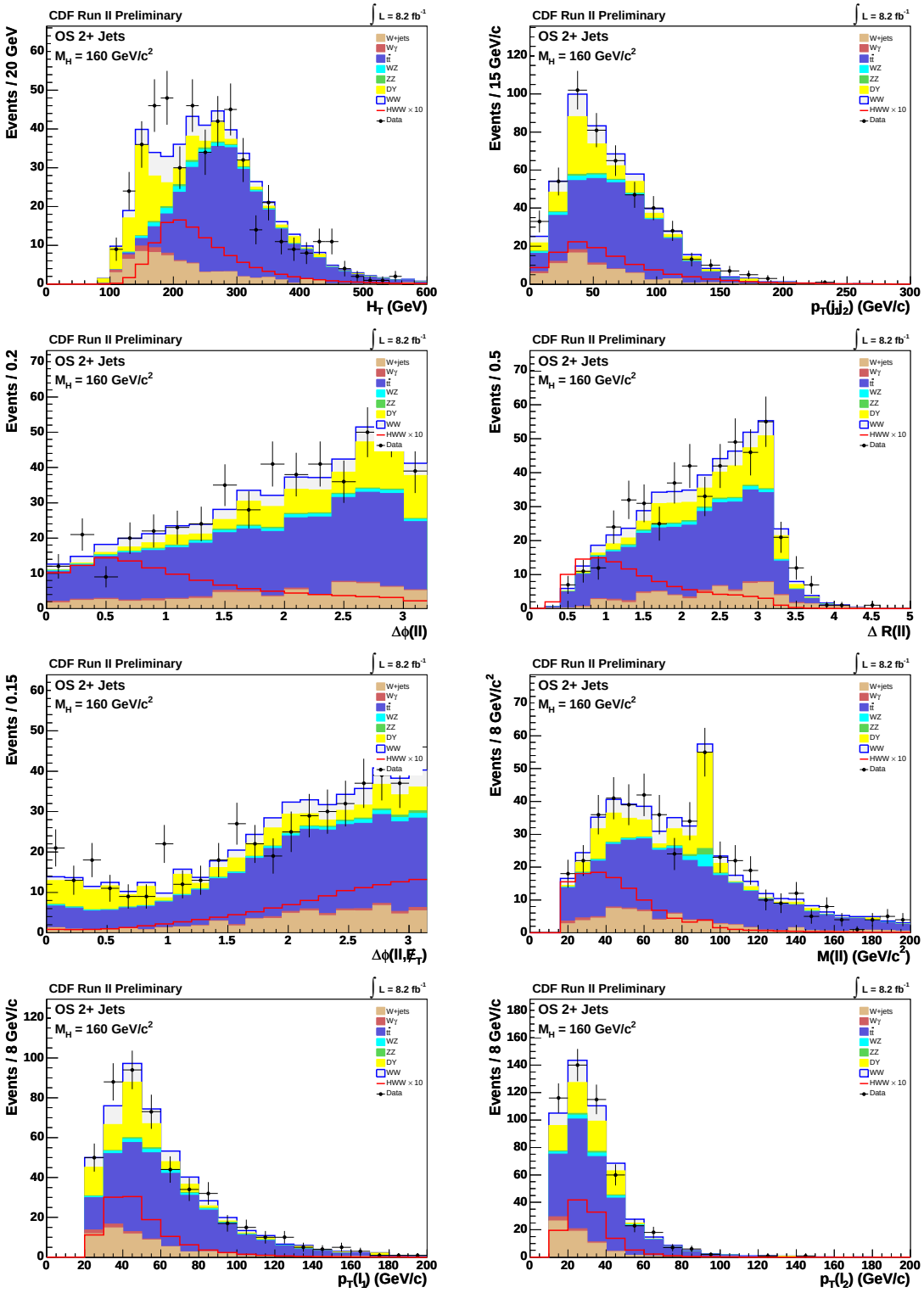

Figure 8.11: Inputs to the NN in the two or more jets category, for a Higgs mass of 160 GeV/c^2.

Uncertainty Source	WW	WZ	ZZ	$t\bar{t}$	DY	$W\gamma$	W+jet	$gg \to H$	WH	ZH	VBF
Cross Section											
ScaleInclusive								0%			
Scale1+Jets								0%			
Scale2+Jets								33%			
PDF Model								29.7%			
Total	*6.0%*	*6.0%*	*6.0%*	7.0%					**5.0%**	**5.0%**	10.0%
Acceptance											
Scale (jets)	*-8.2%*										
PDF Model (leptons)								*4.8%*			
PDF Model (jets)	*4.2%*							-12.3%			
Higher-order Diagrams		*10.0%*	*10.0%*	10.0%		10.0%			**10.0%**	**10.0%**	**10.0%**
$\not{E}_T$ Modeling					25.5%						
Conversion Modeling						10.0%					
Jet Fake Rates							28.0%				
Jet Energy Scale	*-14.8%*	*-12.9%*	*-12.1%*	*-1.7%*	*-29.2%*	*-22.0%*		*-17.0%*	*-4.0%*	*-2.3%*	*-4.0%*
b-tag Veto				3.2%							
Lepton ID Efficiencies	*3.8%*	*3.8%*	*3.8%*	*3.8%*	*3.8%*			*3.8%*	*3.8%*	*3.8%*	*3.8%*
Trigger Efficiencies	*2.0%*	*2.0%*	*2.0%*	*2.0%*	*2.0%*			*2.0%*	*2.0%*	*2.0%*	*2.0%*
Luminosity	*5.9%*	*5.9%*	*5.9%*	*5.9%*	*5.9%*			*5.9%*	*5.9%*	*5.9%*	*5.9%*

Table 8.7: The systematics applied for the 2 or more jet analysis.

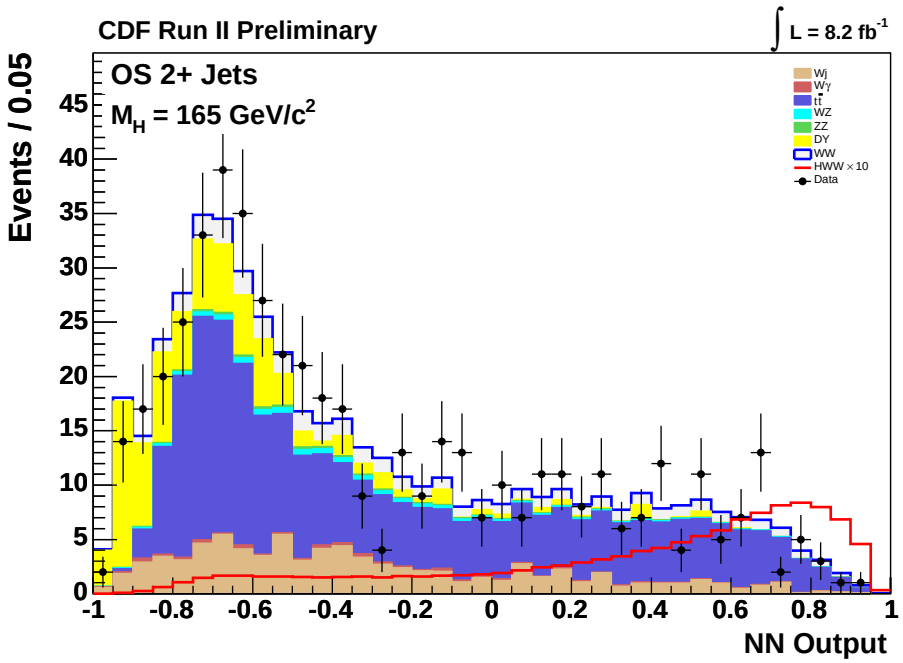

Figure 8.12: Output of the NN in the two or more jets category, for a Higgs mass of 165 GeV/c^2.

8.2.4 Results in the 2 or more jet analysis

We saw no evidence for Higgs production in events with 2 or more jets. We proceeded to set a limit using the same technique described in the previous chapter. The expected and observed limits appear in Table 8.8. A plot of the results appear in Figure 8.16.

Overall, we saw good agreement between the observed and expected limits. We end up with the most sensitivity at a mass of 165 GeV/c^2, with a ratio of limit to Standard Model expectation of 2.51.

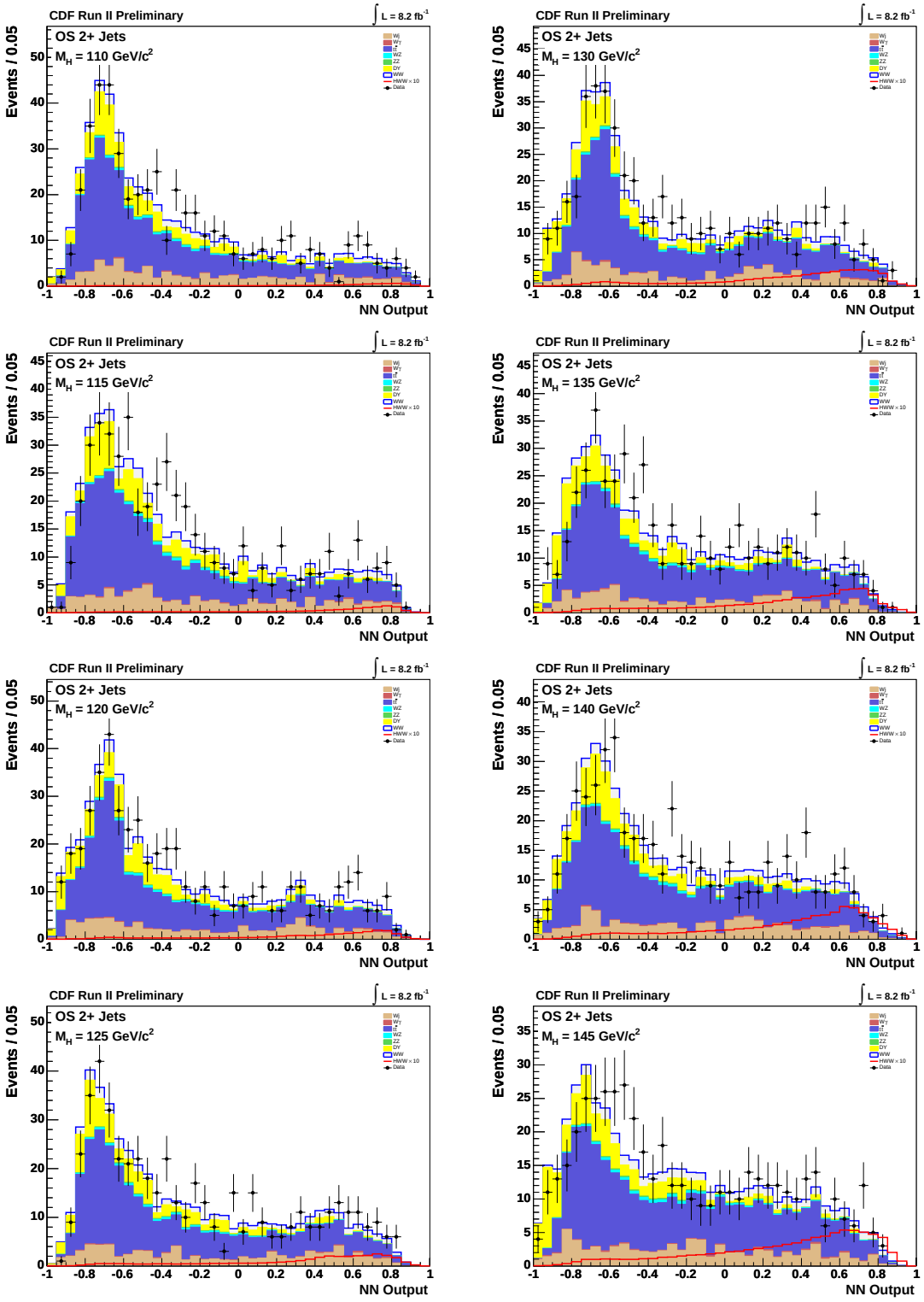

Figure 8.13: Output of the NN in the two or more jets category, for Higgs masses of 110-145 GeV/c^2.

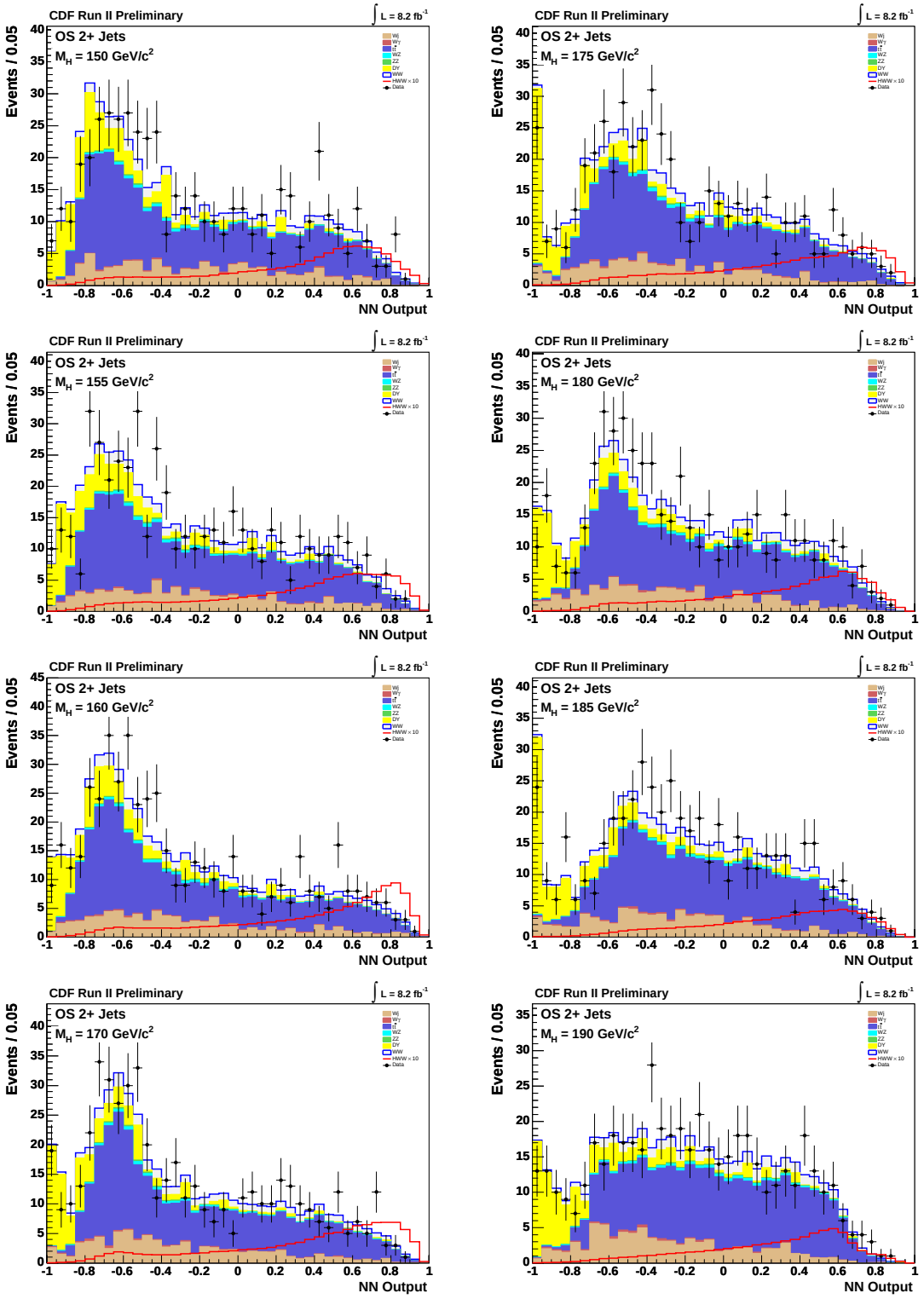

Figure 8.14: Output of the NN in the two or more jets category, for Higgs masses of 150-190 GeV/c^2.

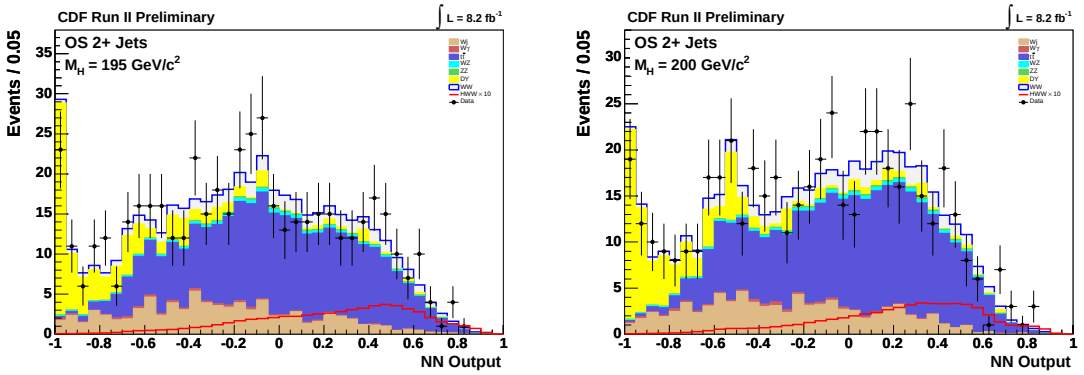

Figure 8.15: Output of the NN in the two or more jets category, for Higgs masses of 195 and 200 GeV/c^2.

OS 2+ Jets	110	115	120	125	130	135	140	145	150	155
$-2\sigma/\sigma_{SM}$	21.26	11.81	7.60	5.29	3.87	2.98	2.52	2.14	1.85	1.63
$-1\sigma/\sigma_{SM}$	28.55	16.31	10.46	7.22	5.30	4.11	3.47	2.96	2.58	2.23
Median/σ_{SM}	**40.18**	**23.15**	**14.74**	**10.26**	**7.51**	**5.85**	**4.96**	**4.27**	**3.70**	**3.22**
$+1\sigma/\sigma_{SM}$	57.89	33.28	21.05	14.59	10.83	8.42	7.09	6.23	5.36	4.67
$+2\sigma/\sigma_{SM}$	81.64	46.22	29.61	20.55	15.14	12.03	10.02	8.88	7.70	6.60
Observed/σ_{SM}	**80.83**	**39.72**	**24.69**	**21.49**	**12.53**	**10.34**	**8.99**	**7.89**	**6.02**	**5.18**

OS 2+ Jets	160	165	170	175	180	185	190	195	200
$-2\sigma/\sigma_{SM}$	1.34	1.28	1.45	1.69	2.06	2.76	3.48	3.97	4.76
$-1\sigma/\sigma_{SM}$	1.80	1.75	2.00	2.34	2.92	3.86	4.92	5.69	6.87
Median/σ_{SM}	**2.60**	**2.51**	**2.85**	**3.33**	**4.19**	**5.60**	**7.12**	**8.32**	**9.98**
$+1\sigma/\sigma_{SM}$	3.77	3.61	4.11	4.91	6.11	8.17	10.44	12.27	14.84
$+2\sigma/\sigma_{SM}$	5.42	5.24	5.90	6.93	8.77	11.87	14.99	17.72	21.31
Observed/σ_{SM}	**3.70**	**2.88**	**3.09**	**3.76**	**4.69**	**6.35**	**9.13**	**12.04**	**14.43**

Table 8.8: The expected and observed limits in the two or more jets category, over the mass range of 110-200 GeV/c^2.

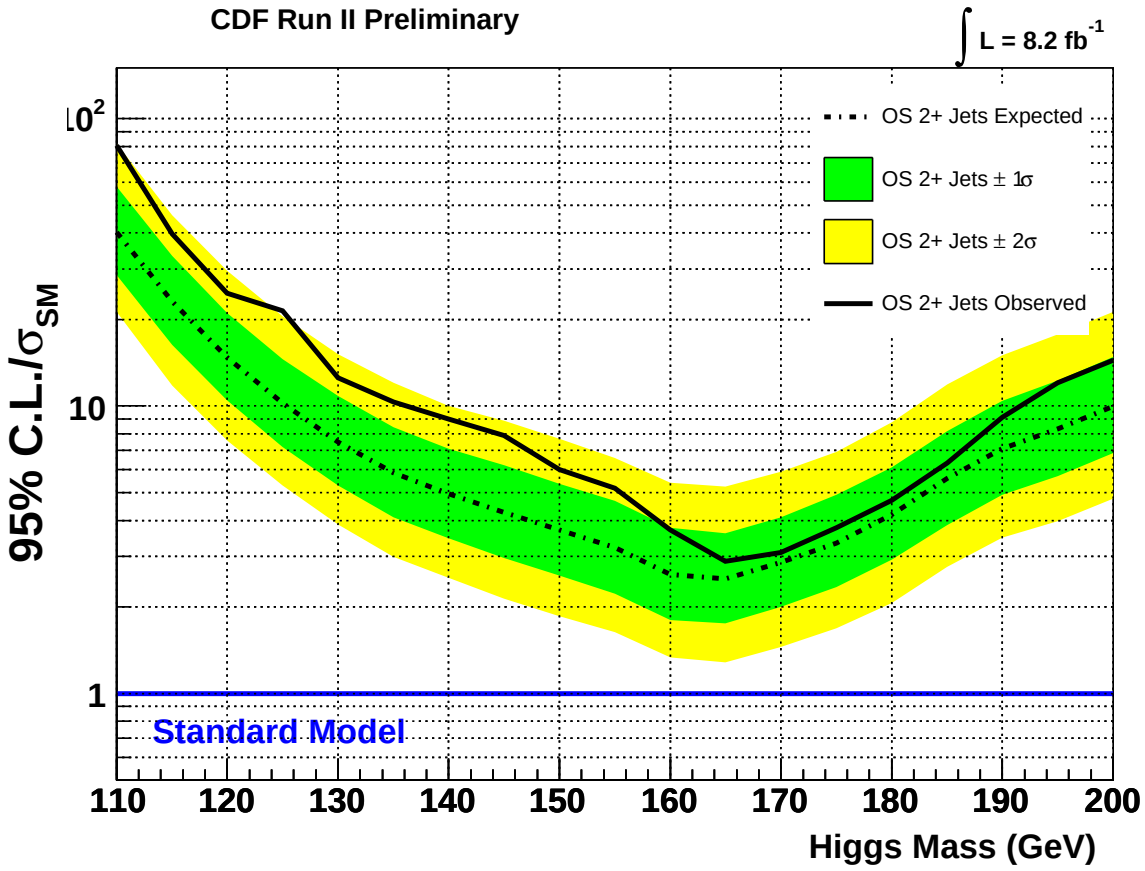

Figure 8.16: A plot of the expected and observed limits in the two or more jets category, over the mass range of 110-200 GeV/c^2.

Chapter 9

Additional channels and final combination

As alluded to earlier in the thesis, we incorporated several additional channels to increase Higgs sensitivity beyond those discussed already. The additional channels we included are the low dilepton mass channel (low M_{ll} channel), same-sign channel, and trilepton channels. With data from all channels, we proceeded to set a limit on Higgs production using the combination of all channels discussed.

This chapter will briefly describe the additional channels used as well as the final combined limit across all channels.

9.1 Additional channels

9.1.1 Low M_{ll} analysis

In the dilepton analysis discussed previously, we applied a cut on the dilepton mass, requiring $M_{ll} > 16$ GeV/c^2. For the low M_{ll} channel, we reversed the cut to examine events specifically with $M_{ll} < 16$ GeV/c^2. Additionally, we vetoed events having leptons with energies larger than 400 GeV. We included events with only zero and one jets.

The largest background in this channel is $W + \gamma$. The requirement placed on $\not\!\!E_{T\,spec}$ effectively removes a potential contribution from heavy flavour decays such as those originating from J/ψ and Υ particles. The $\not\!\!E_{T\,spec}$ variable is defined in Equation 6.1. The expected contributions for signal and background appear in Table 9.1.

As with the previously described channels, we employed NNs over 19 Higgs masses to better separate signal from background. The NN output distribution for a Higgs mass of 165 GeV/c^2 appears in Figure 9.1. We saw no excesses consistent with a Higgs signal in the NN distributions and proceeded to set limits on Higgs production.

The systematic uncertainties table used for limit setting appears in the appendix. A table containing the limits produced for this channel also appears in the appendix. A plot of the limits appear in Figure 9.2.

CDF Run II Preliminary	$\int \mathcal{L} = 8.2$ fb^{-1}		
$M_H = 165$ GeV/c^2			
$t\bar{t}$	1.47	$\pm$	0.28
DY	10.5	$\pm$	1.6
WW	29.9	$\pm$	2.9
WZ	0.79	$\pm$	0.11
ZZ	0.244	$\pm$	0.034
W+jets	48.5	$\pm$	6.5
$W\gamma$	132	$\pm$	13
$BosRad$	39	$\pm$	9.5
Total Background	262	$\pm$	21
$gg \rightarrow H$	3.12	$\pm$	0.51
WH	0.105	$\pm$	0.017
ZH	0.079	$\pm$	0.012
VBF	0.113	$\pm$	0.020
Total Signal	3.42	$\pm$	0.52
Data	260		

AllSB-lowMll

Table 9.1: The expected signal and background contributions compared with data for the low M_{ll} channel.

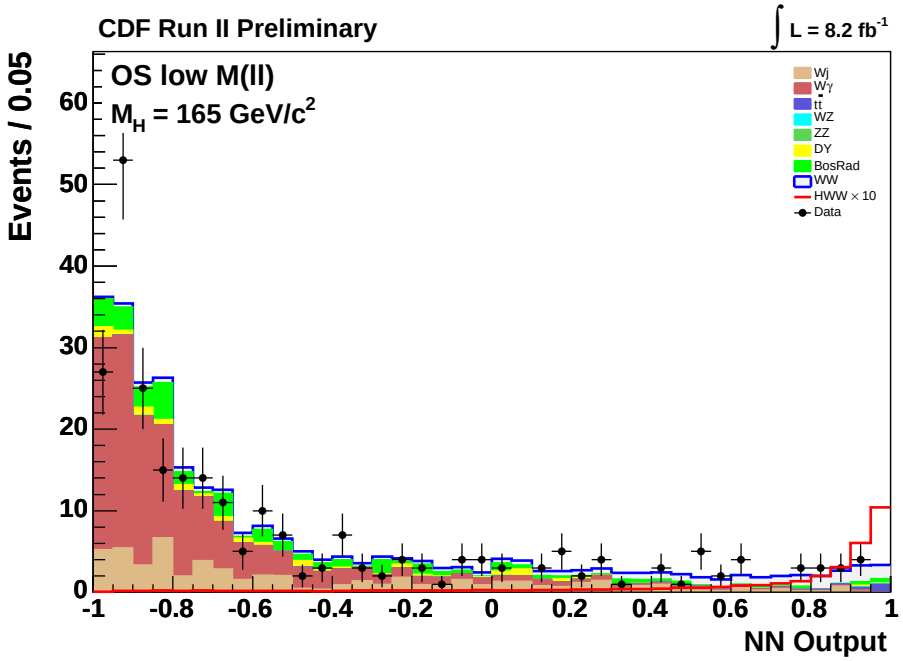

Figure 9.1: Output of the NN in the low M_{ll} channel for a Higgs mass of 165 GeV/c^2.

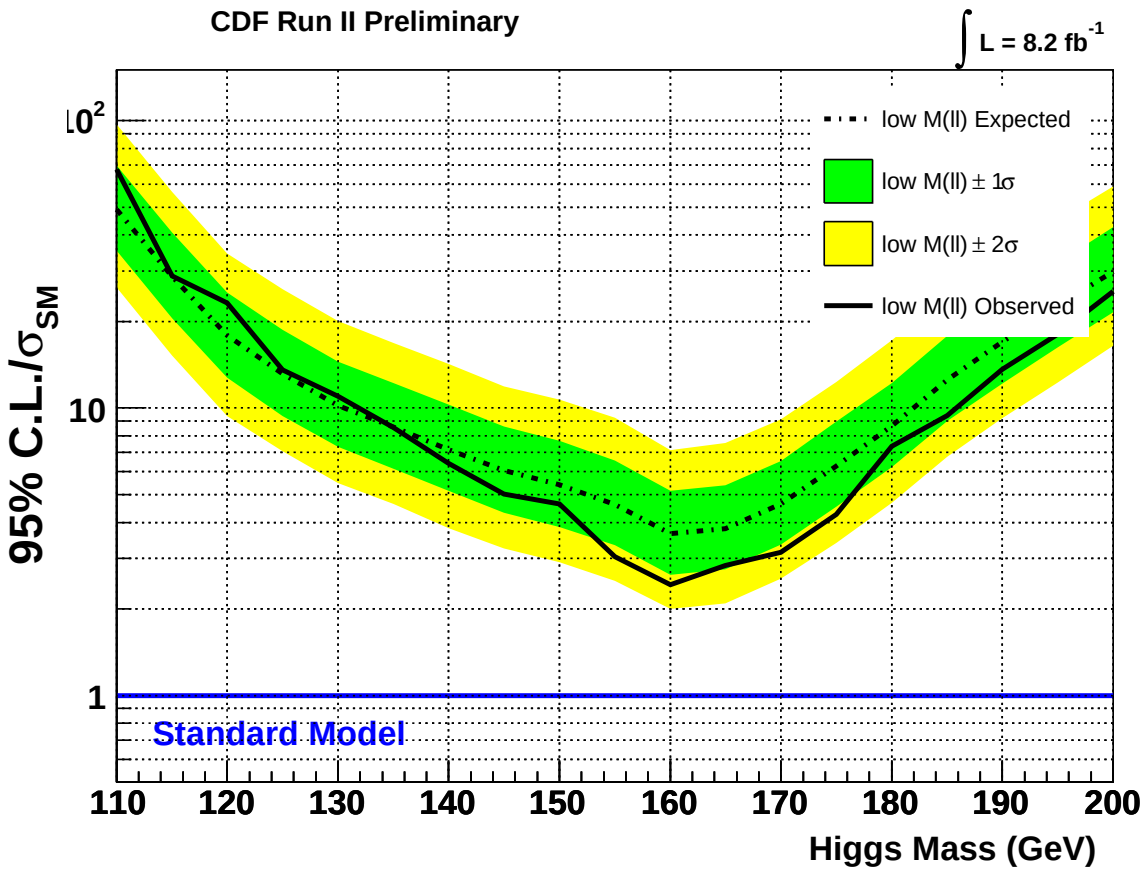

Figure 9.2: A plot of the expected and observed limits in the low M_{ll} channel, over the mass range of 110-200 GeV/c^2.

CDF Run II Preliminary	$\int \mathcal{L} = 8.2$ fb^{-1}		
$M_H = 165$ GeV/c^2			
$t\bar{t}$	2.08	$\pm$	0.30
DY	79	$\pm$	34
WW	0.169	$\pm$	0.075
WZ	14.8	$\pm$	2.0
ZZ	2.80	$\pm$	0.39
W+jets	92	$\pm$	35
$W\gamma$	6.7	$\pm$	1.1
Total Background	198	$\pm$	49
WH	2.73	$\pm$	0.36
ZH	0.404	$\pm$	0.054
Total Signal	3.13	$\pm$	0.42
Data	224		

AllSB-SS

Table 9.2: The expected signal and background contributions compared with data for the same-sign channel.

9.1.2 Same-sign analysis

To increase the breadth of potential Higgs signals, we also included events having same-sign dileptons with the intention of picking up Higgs bosons produced through associated production ($WH \rightarrow WWW$ and $ZH \rightarrow ZWW$). Same-sign dileptons occur quite naturally when the vector boson created in association with the Higgs and one of the W bosons from the Higgs decay both decay leptonically.

The primary backgrounds result from charge mismeasurements. To mitigate this, we veto events containing forward electrons which posses a high rate of charge mismeasurement. Furthermore, we only allow in TCEni electrons in the central region, vetoing LBEni electrons. We also increase the p_T requirement on the second electron from 10 GeV/c^2 to 20 GeV/c^2 to reduce the rate of photons or jets being misidentified as leptons. We also require one or more jets in the event, allowing the W boson that does not decay leptonically to instead decay hadronically. The expected signal and background contributions appear in Table 9.2.

We again use NNs to separate signal from background. The NN output distribution for a Higgs mass of 165 GeV/c^2 appears in Figure 9.3. With no excess seen, we again set an upper limit on Higgs production with this channel.

The systematic uncertainties used for limit setting appears in the appendix. A table containing the limits produced for this channel appear also appears in the appendix. A plot of the limits appears in Figure 9.4.

9.1.3 Trilepton analyses

Trilepton events appear very naturally with the production mechanisms of $WH \rightarrow WWW$ (when all W bosons decay leptoncially) and $ZH \rightarrow ZWW$ (when the Z boson and one of the W bosons decays leptonically). We incorporated trilepton events to further increase Higgs sensitivity.

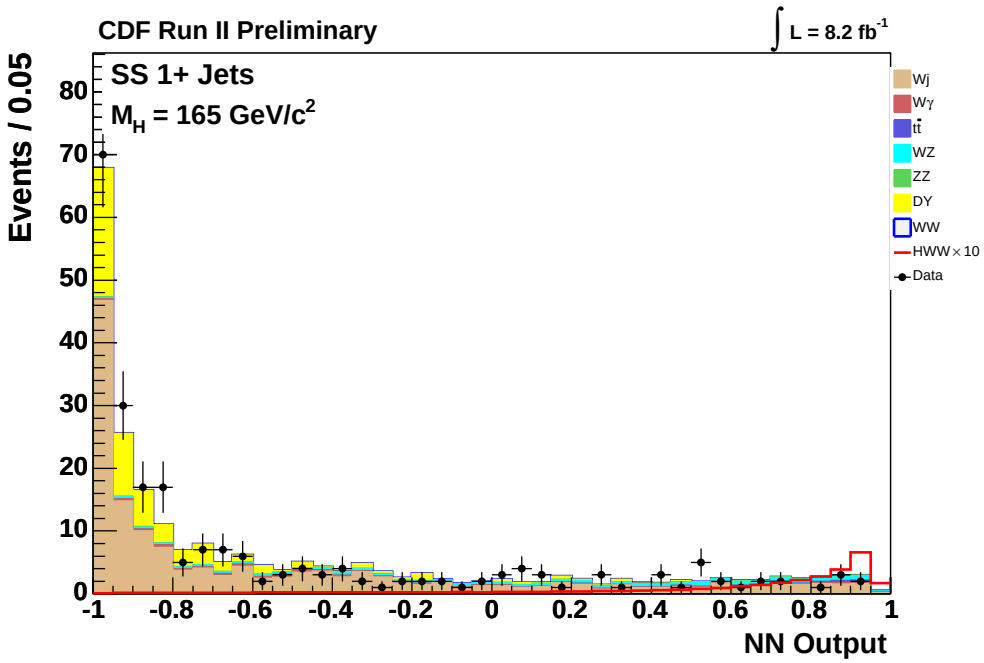

Figure 9.3: Output of the NN in the same-sign channel for a Higgs mass of 165 GeV/c^2.

To be considered for the trilepton channels, an event needed to have a trigger confirmed electron (muon) with $E_T > 20$ GeV ($p_T > 20$ GeV/c). We loosened this requirement for the second and third leptons in the event to $E_T > 10$ GeV and $p_T > 10$ GeV/c for electrons and muons respectively.

We made use of three trilepton channels, sorted by the number of jets in the event and if there are two same-flavor opposite-sign leptons (e.g. e^+e^- and $\mu^+\mu^-$) that have an invariant mass in the range of the Z boson mass. We defined the Z mass range as ± 10 GeV/c^2 around the Z mass of 91 GeV/c^2.

Events having two same-flavor opposite-sign leptons falling in the Z boson mass window should result from primarily associated production via ZH. With one of the W bosons from the Higgs decaying leptoncially, we expected $\not\!\!E_T$ from the presence of the neutrino. We therefore required the event to have $\not\!\!E_T > 10$ GeV. With the expectation that the other W boson decays hadronically, we require one jet in the event. The expected and background contributions compared to data appears in Table 9.3.

We also incorporated a trilepton channel with two or more jets, maintaining the requirement of two same-flavor opposite-sign leptons falling in the Z mass window. The expected signal and background contributions compared to data appear in Table 9.4.

For trilepton events that do not have same-flavor opposite-sign dileptons having an invariant mass falling in the Z mass window, we included these as an additional channel to pick up primarily associated production through WH. These events have all three W bosons decaying leptoncially and therefore have large values

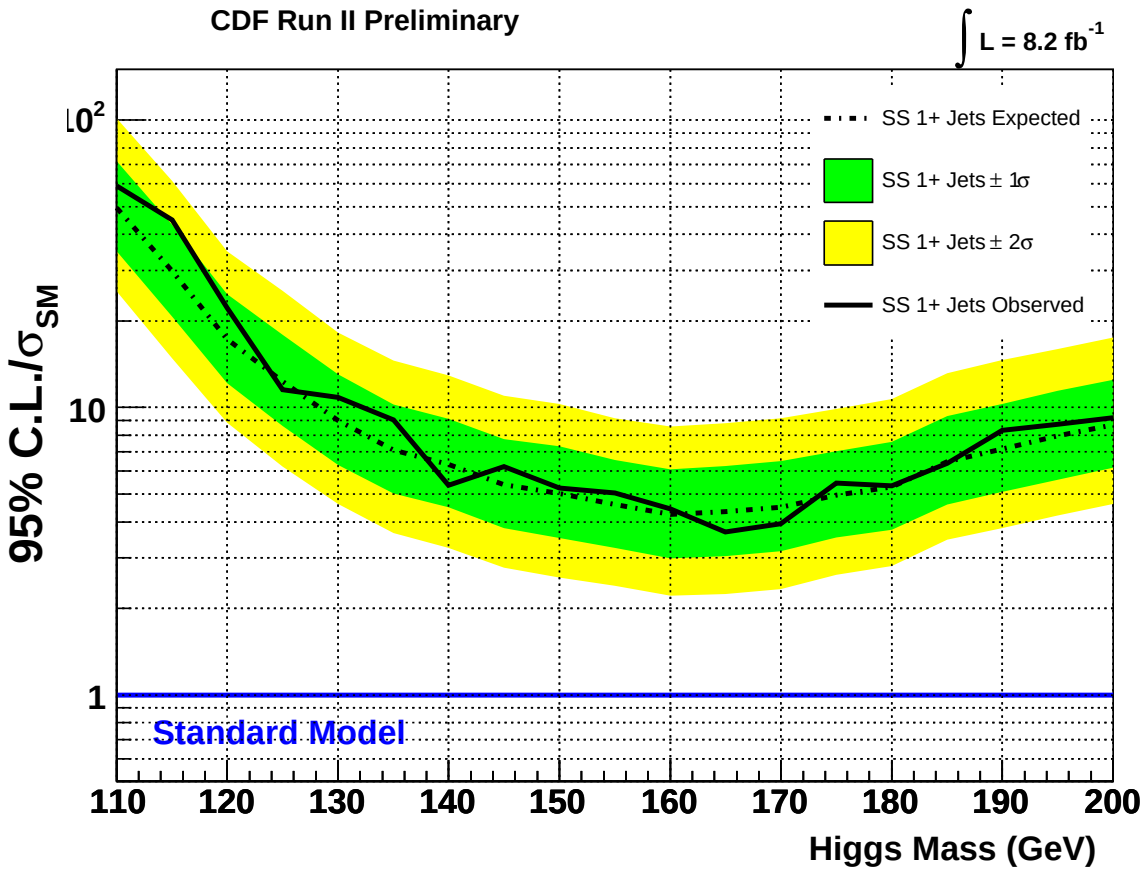

Figure 9.4: A plot of the expected and observed limits in the same-sign channel, over the mass range of 110-200 GeV/c^2.

CDF Run II Preliminary			$\int \mathcal{L} = 8.2$ fb^{-1}
$M_H = 165$ GeV/c^2			
$t\bar{t}$	0.105	±	0.047
WZ	12.1	±	2.0
ZZ	4.98	±	0.71
Z+jets	7.9	±	1.9
$Z\gamma$	6.5	±	1.4
Total Background	31.6	±	3.8
WH	0.0380	±	0.0058
ZH	0.270	±	0.042
Total Signal	0.308	±	0.046
Data		35	

AllSB-trilepZ1j

Table 9.3: The expected signal and background contributions compared with data for the trilepton channel having same-flavor opposite-sign dileptons falling in the Z mass window and one reconstructed jet.

CDF Run II Preliminary	$\int \mathcal{L} = 8.2$ fb^{-1}		
$M_H = 165$ GeV/c^2			
$t\bar{t}$	0.141	$\pm$	0.038
WZ	3.65	$\pm$	0.84
ZZ	1.91	$\pm$	0.38
Z+jets	6.4	$\pm$	1.6
$Z\gamma$	2.55	$\pm$	0.66
Total Background	14.6	$\pm$	2.4
WH	0.0133	$\pm$	0.0034
ZH	0.72	$\pm$	0.11
Total Signal	0.74	$\pm$	0.11
Data	21		

AllSB-trilepZ2j

Table 9.4: The expected signal and background contributions compared with data for the trilepton channel having same-flavor opposite-sign dileptons falling in the Z mass window and two or more reconstructed jets.

CDF Run II Preliminary	$\int \mathcal{L} = 8.2$ fb^{-1}		
$M_H = 165$ GeV/c^2			
$t\bar{t}$	0.64	$\pm$	0.20
WZ	7.1	$\pm$	1.0
ZZ	1.61	$\pm$	0.23
Z+jets	3.84	$\pm$	0.89
$Z\gamma$	4.21	$\pm$	0.84
Total Background	17.4	$\pm$	1.9
WH	0.89	$\pm$	0.12
ZH	0.203	$\pm$	0.028
Total Signal	1.09	$\pm$	0.15
Data	15		

AllSB-trilepNoZ

Table 9.5: The expected signal and background contributions compared with data for the trilepton channel not having same-flavor opposite-sign dileptons falling in the Z mass window.

of $\not\!\!E_T$. We therein required the events in this channel to have $\not\!\!E_T > 20$ GeV. Since these events have no jets at leading order, we place no requirements for the number of events appearing in the channel. The expected signal and background contributions compared to data appear in Table 9.5

The trilepton channels demonstrated no excesses consistent with a SM Higgs boson. We proceeded to set limits in each of the trilepton channels. The systematics associated with the channels and the limits produced appear in the appendix.

9.2 Combination of Higgs limits

9.2.1 CDF $H \rightarrow WW$

With the results from the aforementioned channels, we sought to combine them into a final limit for the $H \rightarrow WW$. As a review, the $H \rightarrow WW$ channels used in the combination are:

- Opposite-sign dileptons, 0 jets, high S/B
- Opposite-sign dileptons, 0 jets, low S/B
- Opposite-sign dileptons, 1 jet, high S/B
- Opposite-sign dileptons, 1 jet, low S/B
- Opposite-sign dileptons, 2 or more jets
- Opposite-sign dileptons, $M_{ll} < 16$ GeV/c^2, 0 or 1 jets
- Same-sign dileptons, 1 or more jets
- Trileptons, two same-flavor opposite-sign leptons in the Z mass region, 1 jet
- Trileptons, two same-flavor opposite-sign leptons in the Z mass region, 2 or more jets
- Trileptons, no same-flavor opposite-sign lepton pairs in the Z mass region, any number of jets

To create the combined limit, we used the procedure described in Section 7.4. We combined the NN templates generated from the above channels into the likelihood constructed out of the Poisson probabilities for each bin in each channel's template for a given Higgs mass. We again evaluated the limit at 19 Higgs masses between 110-200 GeV/c^2, in increments of 5 GeV/c^2. The result of the combination for the CDF $H \rightarrow WW$ analysis appears in Table 9.6. A plot of the expected and observed limits for the combination appears in Figure 9.5.

We exclude at the 95% confidence level, a SM Higgs boson in the mass range of 156 to 175 GeV/c^2 based on the CDF $H \rightarrow WW$ analysis alone.

9.2.2 CDF and D0 combination

The best result produced from the Higgs search at the Tevatron comes from the combination of all search channels at both CDF and D0. The additional production and decay mechanisms used in this two experiment

High Mass	110	115	120	125	130	135	140	145	150	155
$-2\sigma/\sigma_{SM}$	6.15	3.39	2.12	1.41	1.05	0.84	0.71	0.61	0.54	0.46
$-1\sigma/\sigma_{SM}$	8.96	5.03	3.13	2.14	1.61	1.27	1.07	0.93	0.81	0.69
Median/σ_{SM}	**14.03**	**7.86**	**4.86**	**3.38**	**2.57**	**2.01**	**1.69**	**1.48**	**1.27**	**1.07**
$+1\sigma/\sigma_{SM}$	21.81	12.11	7.63	5.31	4.02	3.12	2.68	2.33	2.02	1.66
$+2\sigma/\sigma_{SM}$	32.42	17.85	11.08	7.68	6.00	4.64	3.97	3.40	3.02	2.48
Observed/σ_{SM}	**15.07**	**8.82**	**5.12**	**3.28**	**3.29**	**2.28**	**1.85**	**1.59**	**1.45**	**1.09**

High Mass	160	165	170	175	180	185	190	195	200
$-2\sigma/\sigma_{SM}$	0.36	0.35	0.40	0.47	0.56	0.71	0.86	0.99	1.14
$-1\sigma/\sigma_{SM}$	0.52	0.51	0.58	0.71	0.85	1.07	1.31	1.54	1.75
Median/σ_{SM}	**0.80**	**0.78**	**0.89**	**1.09**	**1.33**	**1.70**	**2.09**	**2.49**	**2.81**
$+1\sigma/\sigma_{SM}$	1.24	1.19	1.38	1.70	2.08	2.71	3.34	4.01	4.59
$+2\sigma/\sigma_{SM}$	1.82	1.77	2.04	2.56	3.11	4.08	5.04	5.99	7.09
Observed/σ_{SM}	**0.75**	**0.77**	**0.84**	**1.04**	**1.57**	**1.75**	**3.08**	**4.34**	**5.26**

Table 9.6: The expected and observed limits for all $H \rightarrow WW$ channels, over the mass range of 110-200 GeV/c^2.

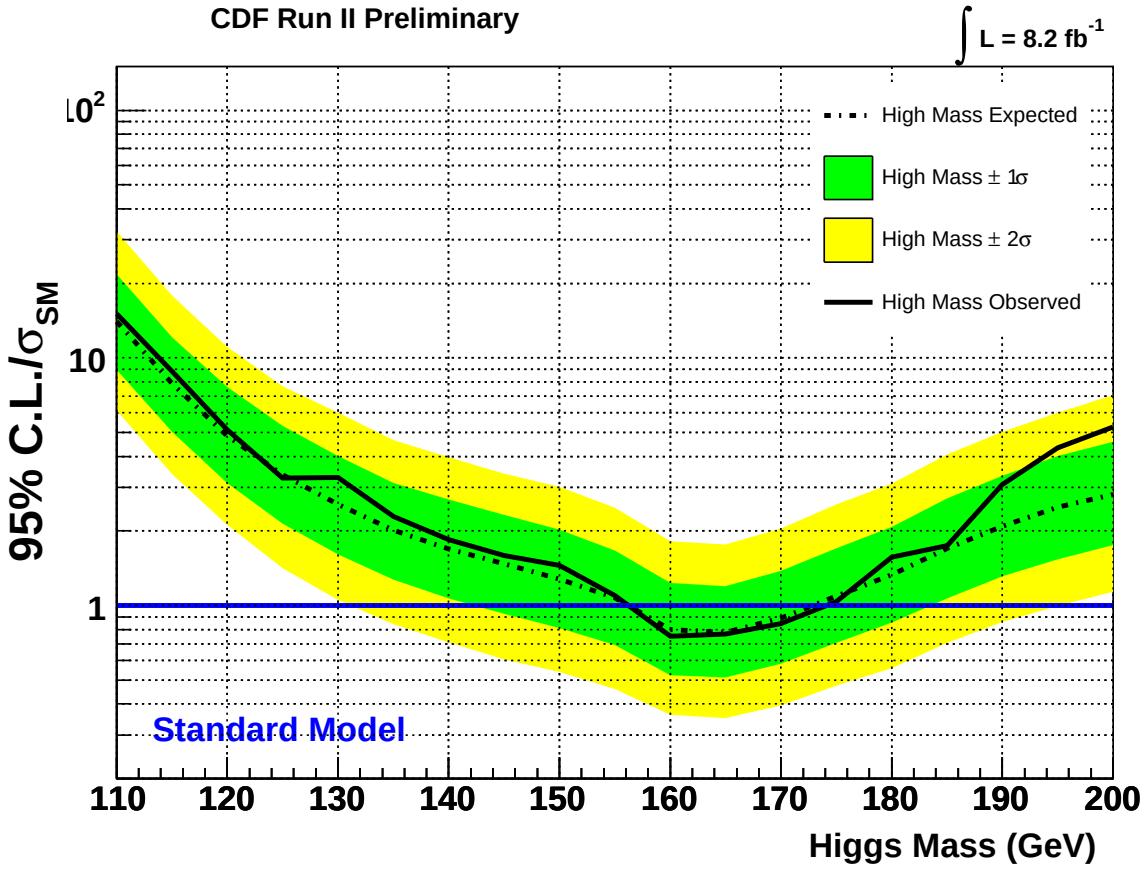

Figure 9.5: A plot of the expected and observed limits for all $H \rightarrow WW$ channels, over the mass range of 110-200 GeV/c^2.

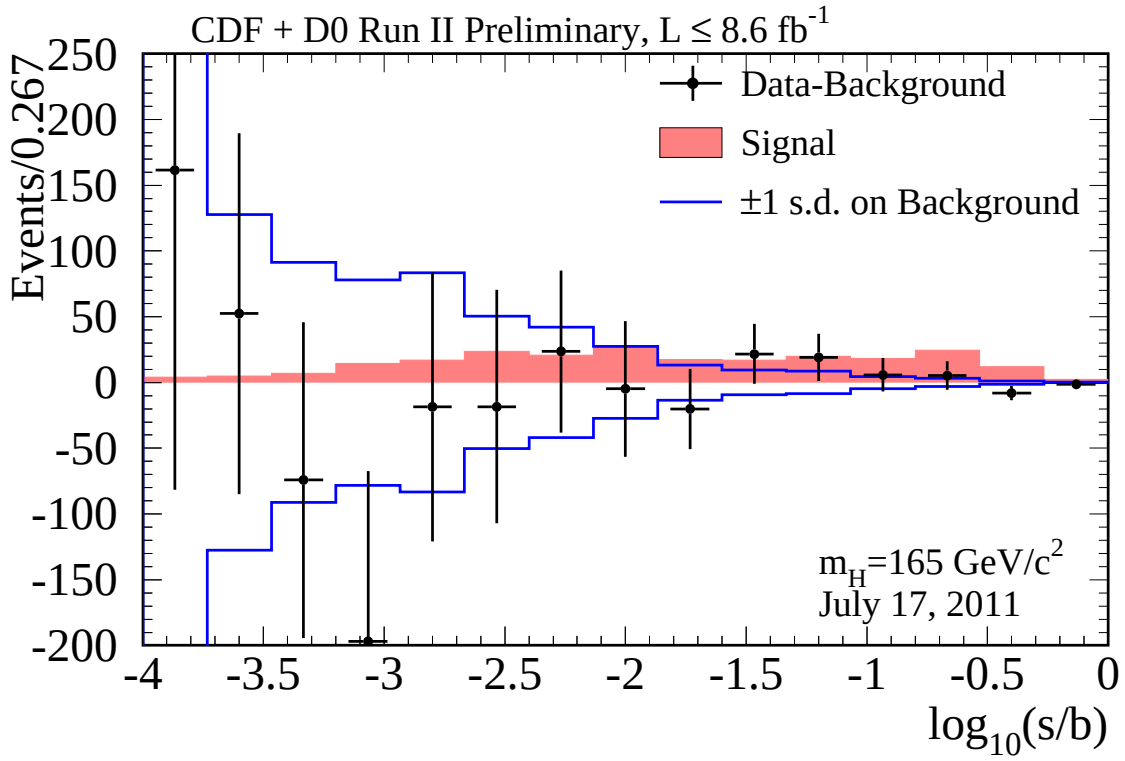

Figure 9.6: The result of combining and sorting the bins in all templates based on S/B and performing subtraction of expected background from data. The appearance of an expected Higgs signal also appears.

combination includes low mass sensitive search channels such as $WH \rightarrow l\nu b\bar{b}$. The procedure for the combination follows the aforementioned technique described above for the CDF $H \rightarrow WW$ combination.

To get a better understanding of whether or not any signal like excesses exist in the data, we sorted the bins across all the input templates according to expected ratios of S/B. We then subtracted the expected number of background events from the data. We can then visually check how consistent the data is with being background only. The result of the procedure appears as Figure 9.6, with what a possible Higgs signal would look like. The data appears consistent with the background expectation.

The combined Tevatron limits appear in Figure 9.7. We exclude at the 95% confidence level, a SM Higgs in the ranges of 100 to 108 GeV/c^2 and 156 to 177 GeV/c^2.

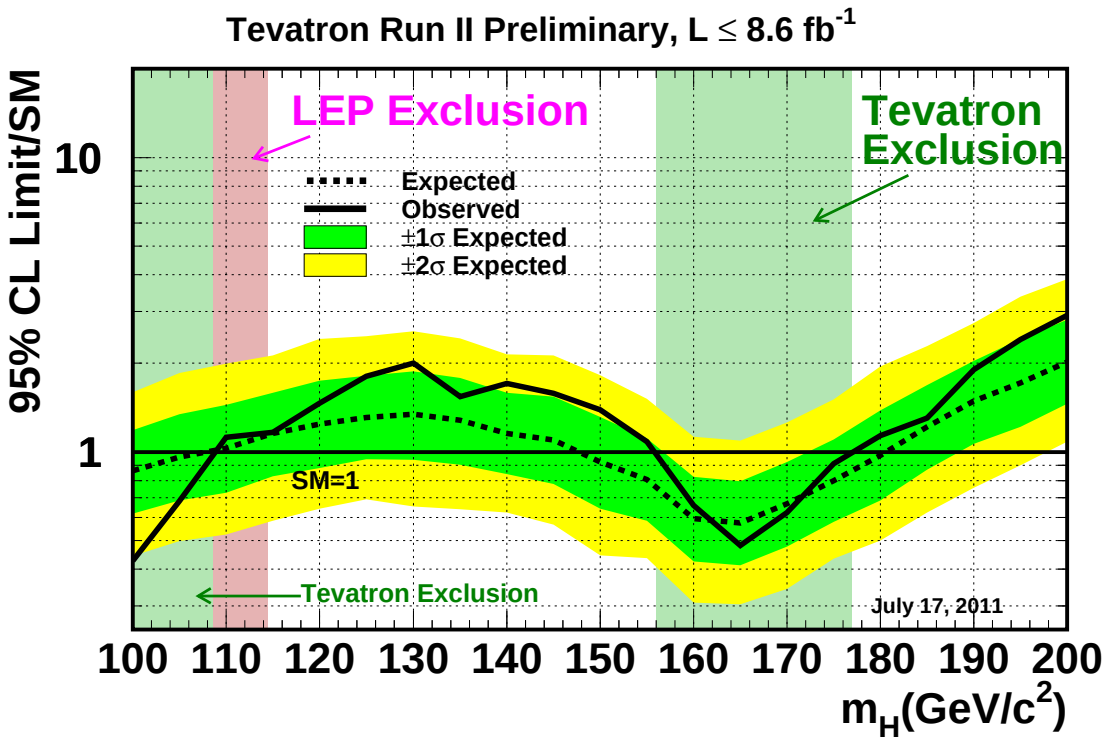

Figure 9.7: The CDF and D0 SM Higgs combined limits.

9.2.3 Conclusions and future prospects

Through the efforts of a great many, CDF and D0 have reached sensitivity in the search for the SM Higgs boson. The CDF $H \to WW$ search finds a 95% confidence level exclusion of 156 to 175 GeV/c^2. When we combined all channels from both CDF and D0, we find a 95% confidence level exclusion of 100 to 108 GeV/c^2 and 156 to 177 GeV/c^2.

As mentioned in a prior chapter, a lot of the sensitivity increases at CDF and D0 resulted not from additions of luminosity alone, but from improvements of the analyses themselves. To reiterate this, the plot demonstrating analysis sensitivity as a function of luminosity reappears in Figure 9.8. As the plot shows, the improvements put into the iteration of the analysis for Summer 2011 allowed CDF to exclude a Higgs boson at a mass of 160 GeV/c^2.

Over the past year, the LHC experiments of ATLAS and CMS both achieved significant sensitivity to the Higgs boson. The search at CDF and D0 is focused on adding the last amount of data accumulated before the Tevatron shut down and implementing improvements that will push the sensitivity curve from Figure 9.8 even lower.

We should hopefully be able to demonstrate or exclude the existence of the Higgs boson within the year.

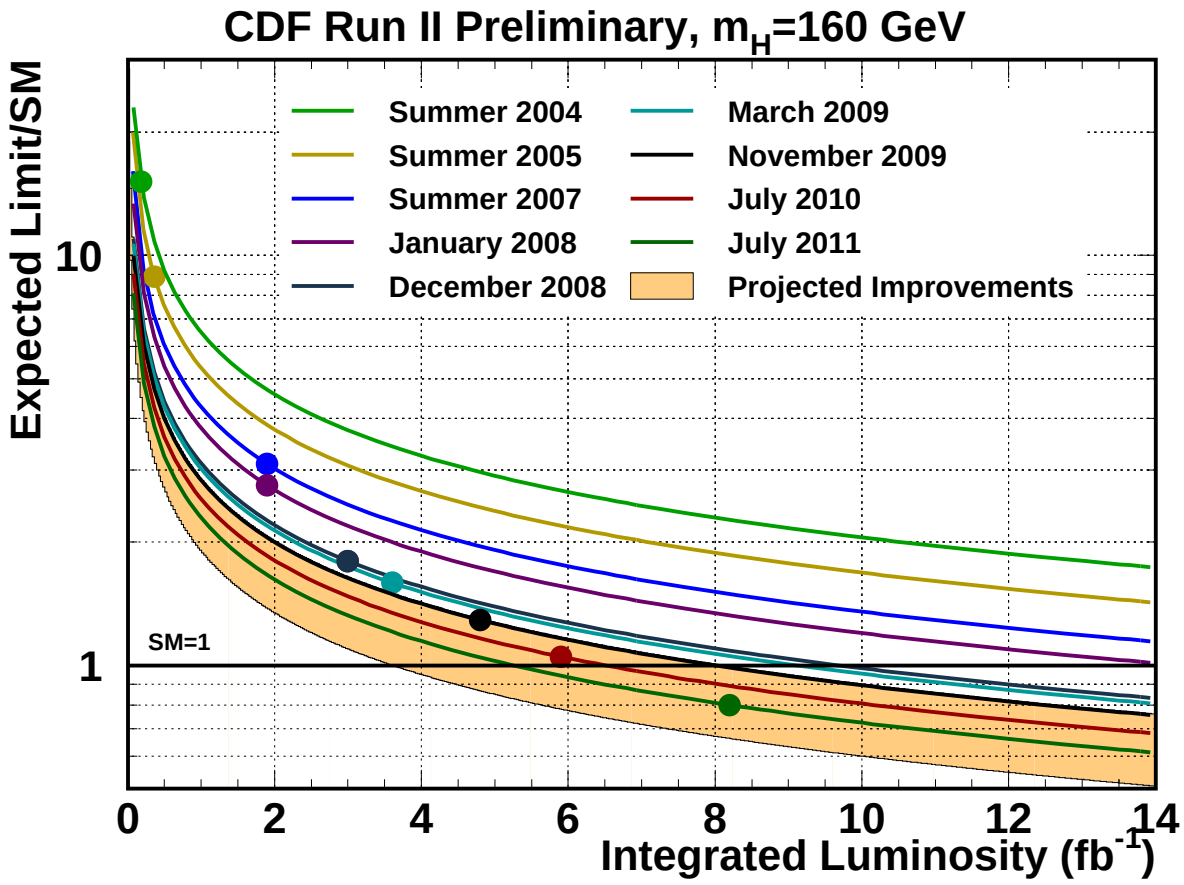

Figure 9.8: The expected sensitivity to the Higgs boson as a function of luminosity for a Higgs mass of 160 GeV/c^2. We plot several curves for different iteration of the analysis. Improving the CDF Higgs analyses significantly increases sensitivity.

Appendix A

Systematic uncertainties and limit tables for the additional channels

Uncertainty Source	WW	WZ	ZZ	$t\bar{t}$	DY	$W\gamma$	W+jet(s)	BosRad	$gg \to H$	WH	ZH	VBF
Cross Section												
ScaleInclusive								8.1%				
Scale1+Jets								0%				
Scale2+Jets								−5.1%				
PDF Model									10.5%			
Total	*6.0%*	*6.0%*	*6.0%*	7.0%	5.0%					5.0%	5.0%	10.0%
Acceptance												
Scale (jets)	*-0.4%*											
PDF Model (leptons)									*1.0%*	*1.0%*	*1.0%*	*1.0%*
PDF Model (jets)	*1.6%*								2.1%	2.1%	2.1%	2.1%
Higher-order Diagrams		10.0%	10.0%	10.0%	10.0%							
Jet Energy Scale	*1.1%*	*2.2%*	*2.0%*	*13.5%*	*6.4%*	*1.3%*			*2.4%*	*9.2%*	*6.5%*	*7.8%*
Conversion Modeling						10.0%						
Jet Fake Rates							13.5%					
Lepton ID Efficiencies	*3.8%*	*3.8%*	*3.8%*	*3.8%*	*3.8%*				*3.8%*	*3.8%*	*3.8%*	*3.8%*
Trigger Efficiencies	*2.0%*	*2.0%*	*2.0%*	*2.0%*	*2.0%*				*2.0%*	*2.0%*	*2.0%*	*2.0%*
Luminosity	*5.9%*	*5.9%*	*5.9%*	*5.9%*	*5.9%*				*5.9%*	*5.9%*	*5.9%*	*5.9%*
BosRad Modeling								25%				

Table A.1: The systematics applied for the low M_{ll} analysis.

low M(ll)	110	115	120	125	130	135	140	145	150	155
$-2\sigma/\sigma_{SM}$	26.24	15.24	9.39	7.07	5.47	4.63	3.82	3.25	2.90	2.50
$-1\sigma/\sigma_{SM}$	35.31	20.50	12.76	9.39	7.33	6.15	5.16	4.33	3.86	3.33
Median/$\sigma_{\mathbf{SM}}$	**48.99**	**28.72**	**17.89**	**13.15**	**10.21**	**8.60**	**7.18**	**6.06**	**5.40**	**4.61**
$+1\sigma/\sigma_{SM}$	69.68	40.78	25.20	18.68	14.53	12.23	10.28	8.65	7.69	6.57
$+2\sigma/\sigma_{SM}$	97.26	56.43	34.58	25.97	20.10	16.85	14.24	11.90	10.70	9.24
Observed/$\sigma_{\mathbf{SM}}$	**67.65**	**28.78**	**23.26**	**13.56**	**10.97**	**8.56**	**6.43**	**5.01**	**4.63**	**3.04**

low M(ll)	160	165	170	175	180	185	190	195	200
$-2\sigma/\sigma_{SM}$	2.00	2.09	2.55	3.39	4.68	6.76	9.20	12.28	16.45
$-1\sigma/\sigma_{SM}$	2.63	2.75	3.35	4.55	6.24	9.02	12.17	16.28	21.59
Median/$\sigma_{\mathbf{SM}}$	**3.65**	**3.81**	**4.64**	**6.30**	**8.65**	**12.55**	**16.99**	**22.70**	**29.90**
$+1\sigma/\sigma_{SM}$	5.16	5.38	6.53	8.96	12.20	17.85	23.92	32.00	42.58
$+2\sigma/\sigma_{SM}$	7.13	7.55	9.13	12.35	17.19	24.78	32.86	45.06	59.17
Observed/$\sigma_{\mathbf{SM}}$	**2.43**	**2.84**	**3.15**	**4.27**	**7.37**	**9.40**	**13.66**	**18.11**	**25.51**

Table A.2: The expected and observed limits in the low M_{ll} channel, over the mass range of 110-200 GeV/c^2.

Uncertainty Source	WW	WZ	ZZ	$t\bar{t}$	DY	$W\gamma$	W+jet	WH	ZH
Cross Section									
Total	*6.0%*	*6.0%*	*6.0%*	7.0%	5.0%			**5.0%**	**5.0%**
Acceptance									
Scale (jets)	-6.1%								
PDF Model (jets)	5.7%								
Higher-order Diagrams		*10.0%*	*10.0%*	10.0%	10.0%	10.0%		**10.0%**	**10.0%**
Jet Energy Scale	*-14.0%*	*-3.9%*	*-2.8%*	*-0.6%*	*-7.7%*	*-7.6%*		*-1.0%*	*-0.7%*
Conversion Modeling						10.0%			
Jet Fake Rates							38.5%		
Charge Mismeasurement Rate	*40.0%*			*40.0%*	*40.0%*				
Lepton ID Efficiencies	*3.8%*	*3.8%*	*3.8%*	*3.8%*	*3.8%*			*3.8%*	*3.8%*
Trigger Efficiencies	*2.0%*	*2.0%*	*2.0%*	*2.0%*	*2.0%*			*2.0%*	*2.0%*
Luminosity	*5.9%*	*5.9%*	*5.9%*	*5.9%*	*5.9%*			*5.9%*	*5.9%*

Table A.3: The systematics applied for the same-sign analysis.

SS 1+ Jets	110	115	120	125	130	135	140	145	150	155
$-2\sigma/\sigma_{SM}$	25.41	14.83	8.86	6.22	4.62	3.65	3.25	2.77	2.56	2.39
$-1\sigma/\sigma_{SM}$	34.93	20.72	12.14	8.61	6.31	5.01	4.49	3.80	3.52	3.24
Median/$\sigma_{\mathbf{SM}}$	**49.60**	**29.82**	**17.30**	**12.31**	**9.01**	**7.11**	**6.34**	**5.39**	**5.02**	**4.60**
$+1\sigma/\sigma_{SM}$	71.97	43.22	24.82	17.91	13.05	10.26	9.15	7.75	7.34	6.56
$+2\sigma/\sigma_{SM}$	101.39	61.36	34.99	25.44	18.26	14.55	12.91	11.01	10.31	9.18
Observed/$\sigma_{\mathbf{SM}}$	**59.04**	**45.02**	**22.26**	**11.53**	**10.85**	**9.05**	**5.37**	**6.22**	**5.24**	**5.05**

SS 1+ Jets	160	165	170	175	180	185	190	195	200
$-2\sigma/\sigma_{SM}$	2.21	2.24	2.34	2.61	2.80	3.47	3.80	4.22	4.63
$-1\sigma/\sigma_{SM}$	2.99	3.04	3.16	3.52	3.75	4.60	5.09	5.61	6.17
Median/$\sigma_{\mathbf{SM}}$	**4.24**	**4.34**	**4.50**	**4.95**	**5.29**	**6.47**	**7.18**	**7.96**	**8.71**
$+1\sigma/\sigma_{SM}$	6.10	6.25	6.50	7.04	7.59	9.33	10.30	11.43	12.48
$+2\sigma/\sigma_{SM}$	8.58	8.82	9.19	9.91	10.70	13.15	14.65	15.99	17.56
Observed/$\sigma_{\mathbf{SM}}$	**4.44**	**3.69**	**3.93**	**5.45**	**5.35**	**6.39**	**8.32**	**8.73**	**9.21**

Table A.4: The expected and observed limits in the same-sign channel, over the mass range of 110-200 GeV/c^2.

Uncertainty Source	WZ	ZZ	$Z\gamma$	$t\bar{t}$	Fakes	WH	ZH
Cross Section							
Total	*6.0%*	*6.0%*	10.0%	7.0%		**5.0%**	**5.0%**
Acceptance							
Higher-order Diagrams	*10.0%*	*10.0%*	15.0%	10.0%		**10.0%**	**10.0%**
Jet Energy Scale	*-7.6%*	*-2.3%*	*-5.3%*	*9.4%*		*-9.0%*	*8.1%*
Jet Fake Rates					24.8%		
b-Jet Fake Rates				42.0%			
MC Run Dependence			5.0%				
Lepton ID Efficiencies	*5.0%*	*5.0%*		*5.0%*		*5.0%*	*5.0%*
Trigger Efficiencies	*2.0%*	*2.0%*		*2.0%*		*2.0%*	*2.0%*
Luminosity	*5.9%*	*5.9%*		*5.9%*		*5.9%*	*5.9%*

Table A.5: The systematics applied for the trilepton channel having same-flavor opposite-sign dileptons falling in the Z mass window and one reconstructed jet.

Trilepton in Z 1 Jet	110	115	120	125	130	135	140	145	150	155
$-2\sigma/\sigma_{SM}$	79.50	50.61	33.69	25.13	19.96	17.16	15.51	14.30	14.02	14.11
$-1\sigma/\sigma_{SM}$	105.36	67.08	44.87	33.50	26.36	22.63	20.30	19.04	18.36	18.60
Median/$\sigma_{\mathbf{SM}}$	**148.57**	**94.09**	**63.08**	**46.81**	**36.78**	**31.76**	**28.13**	**26.74**	**25.75**	**25.71**
$+1\sigma/\sigma_{SM}$	210.56	136.45	89.92	67.77	53.12	45.07	40.45	38.42	36.87	36.81
$+2\sigma/\sigma_{SM}$	296.93	192.76	128.04	95.07	74.61	63.37	56.58	54.03	51.70	52.03
Observed/$\sigma_{\mathbf{SM}}$	**151.55**	**100.00**	**75.18**	**55.83**	**42.76**	**37.66**	**33.45**	**33.11**	**28.07**	**29.83**

Trilepton in Z 1 Jet	160	165	170	175	180	185	190	195	200
$-2\sigma/\sigma_{SM}$	14.29	15.20	16.66	17.95	20.50	24.64	27.83	31.63	34.27
$-1\sigma/\sigma_{SM}$	18.60	19.50	21.60	23.19	26.14	31.70	35.62	40.67	44.13
Median/$\sigma_{\mathbf{SM}}$	**25.79**	**27.02**	**29.79**	**31.81**	**35.85**	**43.95**	**49.39**	**55.57**	**60.69**
$+1\sigma/\sigma_{SM}$	36.94	38.44	42.82	45.70	50.97	62.60	71.10	79.71	86.63
$+2\sigma/\sigma_{SM}$	50.81	54.73	59.75	63.96	72.59	89.93	99.37	112.68	123.80
Observed/$\sigma_{\mathbf{SM}}$	**28.05**	**30.29**	**32.16**	**33.44**	**36.66**	**45.56**	**51.43**	**54.86**	**69.75**

Table A.6: The expected and observed limits in the trilepton channel having same-flavor opposite-sign dileptons falling in the Z mass window and one reconstructed jet, over the mass range of 110-200 GeV/c^2.

Uncertainty Source	WZ	ZZ	$Z\gamma$	$t\bar{t}$	Fakes	WH	ZH
Cross Section							
Total	*6.0%*	*6.0%*	10.0%	7.0%		**5.0%**	**5.0%**
Acceptance							
Higher-order Diagrams	*10.0%*	*10.0%*	15.0%	10.0%		**10.0%**	**10.0%**
Jet Energy Scale	*-17.8%*	*-13.1%*	*-18.2%*	*-3.6%*		*-15.4%*	*-4.9%*
Jet Fake Rates					25.6%		
b-Jet Fake Rates				22.2%			
MC Run Dependence			5.0%				
Lepton ID Efficiencies	*5.0%*	*5.0%*		*5.0%*		*5.0%*	*5.0%*
Trigger Efficiencies	*2.0%*	*2.0%*		*2.0%*		*2.0%*	*2.0%*
Luminosity	*5.9%*	*5.9%*		*5.9%*		*5.9%*	*5.9%*

Table A.7: The systematics applied for the trilepton channel having same-flavor opposite-sign dileptons falling in the Z mass window and two or more reconstructed jets.

Trilepton in Z 2+ Jets	110	115	120	125	130	135	140	145	150	155
$-2\sigma/\sigma_{SM}$	73.74	40.49	24.58	16.73	11.80	9.02	7.52	6.43	5.89	5.41
$-1\sigma/\sigma_{SM}$	95.12	51.89	31.50	20.74	14.89	11.49	9.36	7.99	7.26	6.58
Median/$\sigma_{\mathbf{SM}}$	**129.96**	**70.12**	**42.29**	**28.13**	**20.28**	**15.62**	**12.53**	**10.67**	**9.61**	**8.78**
$+1\sigma/\sigma_{SM}$	182.71	98.82	59.55	39.53	28.48	21.80	17.28	14.86	13.35	12.32
$+2\sigma/\sigma_{SM}$	251.82	137.96	83.61	54.61	39.44	30.13	24.47	20.56	18.67	16.90
Observed/$\sigma_{\mathbf{SM}}$	**144.85**	**72.22**	**45.28**	**29.58**	**21.53**	**15.71**	**12.53**	**10.06**	**9.78**	**8.46**

Trilepton in Z 2+ Jets	160	165	170	175	180	185	190	195	200
$-2\sigma/\sigma_{SM}$	4.98	4.90	5.33	5.87	6.64	7.88	9.08	10.19	11.25
$-1\sigma/\sigma_{SM}$	5.91	5.76	6.37	7.04	7.93	9.43	11.06	12.43	13.58
Median/$\sigma_{\mathbf{SM}}$	**7.65**	**7.53**	**8.37**	**9.26**	**10.48**	**12.48**	**14.63**	**16.48**	**17.92**
$+1\sigma/\sigma_{SM}$	10.56	10.31	11.67	12.84	14.56	17.26	20.58	22.80	24.92
$+2\sigma/\sigma_{SM}$	14.82	14.14	16.06	17.92	20.16	24.11	28.41	31.31	34.40
Observed/$\sigma_{\mathbf{SM}}$	**7.03**	**6.44**	**7.77**	**8.57**	**9.70**	**12.57**	**14.08**	**15.87**	**18.19**

Table A.8: The expected and observed limits in the trilepton channel having same-flavor opposite-sign dileptons falling in the Z mass window and two or more reconstructed jets, over the mass range of 110-200 GeV/c^2.

Uncertainty Source	WZ	ZZ	$Z\gamma$	$t\bar{t}$	Fakes	WH	ZH
Cross Section							
Total	*6.0%*	*6.0%*	10.0%	7.0%		**5.0%**	**5.0%**
Acceptance							
Higher-order Diagrams	*10.0%*	*10.0%*	15.0%	10.0%		**10.0%**	**10.0%**
Jet Energy Scale			*-2.7%*				
Jet Fake Rates					25.6%		
b-Jet Fake Rates				27.3%			
MC Run Dependence			5.0%				
Lepton ID Efficiencies	*5.0%*	*5.0%*		*5.0%*		*5.0%*	*5.0%*
Trigger Efficiencies	*2.0%*	*2.0%*		*2.0%*		*2.0%*	*2.0%*
Luminosity	*5.9%*	*5.9%*		*5.9%*		*5.9%*	*5.9%*

Table A.9: The systematics applied for the trilepton channel not having same-flavor opposite-sign dileptons falling in the Z mass window.

Trilepton NoZ	110	115	120	125	130	135	140	145	150	155
$-2\sigma/\sigma_{SM}$	30.38	18.10	11.73	8.31	6.43	5.23	4.62	4.10	3.92	3.71
$-1\sigma/\sigma_{SM}$	37.76	22.81	14.64	10.38	8.07	6.60	5.84	5.18	4.83	4.54
Median/$\sigma_{\mathbf{SM}}$	**51.32**	**31.15**	**19.82**	**14.09**	**10.93**	**8.93**	**7.89**	**7.03**	**6.54**	**6.03**
$+1\sigma/\sigma_{SM}$	72.24	43.56	28.08	19.80	15.50	12.58	11.17	9.94	9.28	8.51
$+2\sigma/\sigma_{SM}$	100.24	60.45	38.99	28.00	21.39	17.78	15.62	13.80	12.77	11.96
Observed/$\sigma_{\mathbf{SM}}$	**48.41**	**33.70**	**19.35**	**14.71**	**11.55**	**8.74**	**7.51**	**7.78**	**7.81**	**6.29**

Trilepton NoZ	160	165	170	175	180	185	190	195	200
$-2\sigma/\sigma_{SM}$	3.40	3.49	3.91	4.48	5.24	6.41	7.84	9.11	10.35
$-1\sigma/\sigma_{SM}$	4.13	4.20	4.71	5.42	6.44	7.84	9.61	11.07	12.91
Median/$\sigma_{\mathbf{SM}}$	**5.49**	**5.46**	**6.22**	**7.18**	**8.59**	**10.44**	**12.85**	**14.84**	**17.34**
$+1\sigma/\sigma_{SM}$	7.60	7.63	8.72	9.99	11.99	14.51	18.05	20.80	24.30
$+2\sigma/\sigma_{SM}$	10.48	10.74	11.92	13.98	16.77	20.32	25.33	29.35	34.41
Observed/$\sigma_{\mathbf{SM}}$	**5.83**	**6.31**	**6.95**	**7.92**	**10.34**	**13.48**	**15.57**	**20.77**	**23.73**

Table A.10: The expected and observed limits in the trilepton channel not having same-flavor opposite-sign dileptons falling in the Z mass window, over the mass range of 110-200 GeV/c^2.

References

[1] The LEP Electroweak Working Group, *Precision Electroweak Measurements and Constraints on the Standard Model* (2011), lepewwg.web.cern.ch/LEPEWWG.

[2] ALEPH Collaboration, DELPHI Collaboration, L3 Collaboration, OPAL Collaboration, and LEP Working Group for Higgs Boson Searches, Phys. Lett. B **565**, 61 (2003).

[3] *See the* TEV4LHC *working group webpage*, maltoni.home.cern.ch/maltoni/TeV4LHC/SM.html.

[4] C. Quigg (2002), `hep-ph/0204104v1`.

[5] K. Nakamura *et al.*, JPG **37**, 075021 (2010), (pdf.lbl.gov).

[6] J. Rosner (2002), `hep-ph/0108195v6`.

[7] Fermilab, *Accelerator concepts*, www-bdnew.fnal.gov/operations/rookie_books/concepts_v3.6.pdf.

[8] Fermilab, *Run II handbook*, www-bd.fnal.gov/doereview02/RunII_handbook.pdf.

[9] T. A. *et al.*, Nucl. Instr. and Meth. A **526**, 526 (2004).

[10] A. S. *et al.*, Nucl. Instr. and Meth. A **447**, 1 (2000).

[11] R. Blair, *et al.* (CDF Collaboration) (1996), `FERMILAB-PUB-96/390-E`.

[12] A. A. *et al.*, Nucl. Instr. and Meth. A **538**, 358 (2004).

[13] D. A. *et al.*, Nucl. Instr. and Meth. A **461**, 540 (2001).

[14] *CERN FILAR webpage*, hsi.web.cern.ch/hsi/s-link/devices/filar.

[15] A. B. et al., Nucl. Phys. **A566**, 375 (2006), `hep-ex/0510047`.

[16] T. Sjostrand, S. Mrenna, and P. Skands, JHEP **0605**, 026 (2006).

[17] U. Baur and E. L. Berger, Phys. Rev. **D47**, 4889 (1993).

[18] S. Frixione and B. Webber, JHEP **0206**, 029 (2002), `[hep-ph/0204244]`.

[19] G. C. et al., JHEP **0101**, 010 (2001).

[20] D. de Florian and M. Grazzini, Phys. Lett. B **674**, 291 (2009), `0901.2427 [hep-ph]`.

[21] C. Anastasiou, G. Dissertori, M. Grazzini, F. Stoeckli, and B. R. Webber (2009), `0905.3529 [hep-ph]`.

[22] S. Actis, G. Passarino, C. Sturm, and S. Uccirati, Phys. Lett. B **670**, 12 (2008).

[23] U. Aglietti, R. Bonciani, G. Degrassi, and A. Vicini (2006), `hep-ph/0610033v1`.

[24] J. Baglio and A. Djouadi (2010), `arXiv:1003.4266v2 [hep-ph]`.

[25] O. Brein, A. Djouadi, and R. Harlander, Phys. Lett. B **579**, 149 (2004).

[26] M. L. Ciccolini, S. Dittmaier, and M. Kramer, Phys. Rev. D **68**, 073003 (2003).

[27] P. Bolzoni, F. Maltoni, S.-O. Moch, and M. Zaro, Phys. Rev. Lett. **105**, 011801 (2010), 0901.2427 [hep-ph].

[28] M. L. Ciccolini, A. Denner, and S. Dittmaier, Phys. Rev. D **77**, 013002 (2008).

[29] A. Djouadi, J. Kalinowski, and M. Spira, Comput. Phys. Commun. **108**, 56 (1998).

[30] R. Brun, R. Hagelberg, M. Hansroul, and J. C. Lassalle, CERN-DD-78-2-REV and CERN-DD-78-2.

[31] J. Campbell and K. Ellis, MCFM - *monte carlo for femtobarn processes* (2005), http://mcfm.fnal.gov/.

[32] H. Kolanoski, Nucl. Instrum. Methods **A 367**, 14 (1995).

[33] M. Feindt, Technical Report IEKP-KA/01-1 (2001).

[34] U. Langenfeld, S. Moch, and P. Uwer, Phys. Rev. D **80**, 054009 (2009).

[35] N. Kidonakis and R. Vogt, Phys. Rev. D **78**, 074005 (2008).

[36] M. Cacciari, S. Frixione, M. L. Mangano, P. Nason, and G. Ridolfi, JHEP **0809**, 127 (2008).

[37] J. M. Campbell and R. K. Ellis, Phys. Rev. **D60**, 113006 (1999), hep-ph/9905386.

[38] M. Grazzini, HNNLO, http://theory.fi.infn.it/grazzini/codes.html.

[39] S. Catani and M. Grazzini, Phys. Rev. Lett. **98**, 222002 (2007).

[40] M. Grazzini, JHEP **0802**, 043 (2008).

[41] A. D. Martin, W. J. Stirling, R. S. Thorne, and G. Watt (2009), 0901.0002 [hep-ph].

[42] G. Bozzi, S. Catani, D. deFlorian, and M. Grazzini, Phys. Lett. B **564**, 65 (2003).

[43] G. Bozzi, S. Catani, D. deFlorian, and M. Grazzini, Nucl. Phys. B **737**, 73 (2006).

[44] C. Balazs, J. Huston, and I. Puljak, Phys. Rev. D **63**, 014021 (2001).

[45] C. Balazs and C.-P. Yuan, Phys. Lett. B **478**, 192 (2000).

[46] Q.-H. Cao and C.-R. Chen, Phys. Rev. D **76**, 073006 (2007).

[47] D. Acosta *et al.* (CDF Collaboration), Phys. Lett. D **71**, 052003 (2005).